Dynamics and Quantum Fluctuations of Many-body States of Interacting Ultracold Gases

by

Zehan Li

Bachelor of Science, University of Science and Technology of China, 2015

Submitted to the Graduate Faculty of

the Dietrich School of Arts and Sciences in partial fulfillment

of the requirements for the degree of

Doctor of Philosophy

University of Pittsburgh

2021

UNIVERSITY OF PITTSBURGH

DIETRICH SCHOOL OF ARTS AND SCIENCES

This dissertation was presented

by

Zehan Li

It was defended on

January 29th 2021

and approved by

W. Vincent Liu, Professor, Department of Physics and Astronomy

Brian Batell, Assistant Professor, Department of Physics and Astronomy

Daniel Boyanovsky, Professor, Department of Physics and Astronomy

Ira Rothstein, Professor, Department of Physics, Carnegie Mellon University

David Snoke, Professor, Department of Physics and Astronomy

Dynamics and Quantum Fluctuations of Many-body States of Interacting Ultracold Gases

Zehan Li, PhD

University of Pittsburgh, 2021

We explored interaction cold atoms in new quantum regimes that have no prior analogue in condensed matter materials in three related main topics. First, motivated by recent advance in orbitally tuned Feshbach resonance experiments, we analyze the ground-state phase diagram and related low-energy excitation spectra of a high partial wave interacting Bose gas. Remarkably different from what was previously known in the p-wave case, the atomic superfluid is found to be momentum-independent in the present d-wave case. What is more, we study the quantum fluctuations in the condensates of a mixture of bosonic atoms and molecules with interspecies p-wave interaction. Our analysis shows that the quantum phase of coexisting atomic and molecular condensates is unstable at the mean-field level. The quantum Lee-Huang-Yang correction to the mean-field energy provides a remarkable mechanism to self-stabilize the phase. The correlated order spontaneously breaks a rich set of global $U(1)$ gauge, atomic spin, spatial rotation and translation, and time-reversal symmetries.

Second, we study the dynamics of a non-integrable spin chain model composed of two ingredients - a nearest neighbor Ising coupling, and an infinite range XX interaction. Unlike other fast scrambling many-body systems, this model is not known to be dual to a black hole. We demonstrate that our model exhibits fast scrambling for a wide parameter regime, accompanied by a fast growth of the entanglement entropy, as well as a swift change in the magnetization.

Third, to extend the study of the highly chaotic many-body model, we analyze the ground state phases of the model with a nearest neighbor XXZ interaction and an infinite range XX interaction. By employing spin-wave theory, we find that there is a large parameter regime where the continuous $U(1)$ symmetry of this model is spontaneously broken, which is not possible in the absence of the infinite range interaction by the Mermin-Wagner theorem.

Furthermore, we demonstrate that in the $U(1)$ symmetry broken phase, the half chain entanglement entropy violates the area law logarithmically. Our work demonstrates that the interplay of short and long range interactions can lead to novel quantum phases of matter.

Table of Contents

List of Tables

List of Figures

Preface

I would like to thank my supervisor Prof. W. Vincent Liu for his guidance and support during my PhD study. With his guidance, these five years working with Prof. Liu are delightful for me. He built up the connection between me and the top-level physics researchers in the MURI group. I have also got the opportunity to study in the summer school of the Stockholm University, due to his effort. I feel grateful and honored to be his student.

I enjoy collaborations with Dr. Jian-song Pan and Dr. Sayan Choudhury. They have instructed me a lot during my research and study. I am also grateful to Dr. Ahmet Keles Dr. Haiping Hu, and Dr. Biao Huang for the discussions.

Also, I would like to thank my committee members Prof. Brian Batell, Prof. Daniel Boyanovsky, Prof. Ira Rothstein, and Prof. David Snoke. Their questions and discussions during the committee meetings benefit me a lot. In particular, Prof. Daniel Boyanovsky expert knowledge on dynamical stabilities are very helpful.

Finally, I thank my parents Jun Li and Xia Shi, and my wife Yu Liu for their constant support and love in my career.

1.0 Introduction

In the past three decades the outlook of condensed matter physics has been deeply and unexpectedly revolutionized by a few experimental breakthroughs in atomic physics, quantum optics and nanoscience. Equilibrium systems can often be understood using a combination of a mean field theory, renormalization group, and universality. This allows us to understand low temperature experimental data obtained in complex systems, such as interacting bosons, in terms of simple effective models containing a few relevant parameters [3].

As the milestone of the history of Bose-Einstein condensate, the repulsive interacting bosonic gases has been observed in a macroscopic regime experimentally [4] in a Rubidium system, where the atoms were confined in magnetic traps and cooled down to extremely low temperature, of the order of fractions of microkelvins. Countless of experiments were applied to BEC with s-wave interaction [5, 6, 7, 8]. However, as the development of the narrow Feshbach Resonance techniques, more and more attentions are addressed to bosonic systems with high-partial wave interactions, due to their unique properties, such as the finite momentum superfluidity and time reversal symmetry breaking [9, 2, 10]. We predict a possible realization of self-confinement BEC with p-wave interaction, which breaks the spherical symmetry naturally [11].

Away from equilibrium the situation is much less clear. The dynamics of thermalization in closed quantum systems has received immense attention in recent years [12, 3, 13, 14, 15]. A central focus of these studies has been the "scrambling" of quantum information [16, 17, 18, 19]. Scrambling is the process by which locally encoded information gets spread over non-local many- body degrees of freedom during the time evolution of a complex quantum system. This paradigm has been used to address a diverse array of questions in areas ranging from quantum chaos to quantum gravity [20, 21, 22, 23]. Several recent experiments in a variety of analog quantum simulator platforms have successfully probed quantum scrambling [24, 25, 26, 27], thereby paving the path to answer fundamental questions about non-equilibrium quantum dynamics.

2.0 Scattering and Feshbach Resonance

Due to the rich internal energy-level structure, an atom can interact with external electric and magnetic fields to induce effective trapping potentials. In this chapter, we will introduce the scattering between two atoms with the existence of an external magnetic field, i.e., the Feshbach resonance, which is a key ingredient of ultracold atomic physics.

2.1 Scattering

In this section, we will study the scattering of two atoms [28]. If one neglects small relativistic spin interactions, the solution of the Schrödinger equation for the relative motion can describe the collision process. For example, For positive energy ϵ, the s-wave wavefunction in the asymptotic region $r \gg R_0$ can be written as

$$\psi_0(r) \propto \sin[kr + \delta_0(k)]/r, \tag{2.1}$$

where $r = |\mathbf{r}_1 - \mathbf{r}_2|$ is the relative coordinate of the two atoms, R_0 is the spatial range of the interatomic potential, $\delta_0(k)$ is the s-wave phase shift and $k = \sqrt{2m_r\epsilon}/\hbar$ is the wavevector of the scattering wave with m_r the reduced mass of the pair of atoms ($m_r = m/2$ for identical atoms). The s-wave scattering amplitude does not depend on the scattering angle and is given as

$$f_0(k) = \frac{1}{-k\cot\delta_0(k) + ik}. \tag{2.2}$$

The quantity a is the s-wave scattering length, which plays a crucial role in the scattering processes at low energy. It is defined as $a = -f_0(k \to 0)$. By including terms to order k^2 in the expansion of the phase shift $\delta_0(k)$ at low momenta one obtains the result

$$f_0(k) = -\frac{1}{a^{-1} - k^2R^*/2 + ik}\ , \tag{2.3}$$

defining the effective range R^* of interactions. This length scale is usually of the same order of the range R_0, however in some cases, *e.g.* close to a narrow Feshbach resonance, it can

become much larger than R_0 providing a new relevant scale. In the limit $a \to \infty$, referred to as "unitary limit", the scattering amplitude (2.3) at wavevectors $k \ll 1/|R^*|$ obeys to the universal law $f_0(k) = i/k$, independent of the interaction.

In the many-body treatment of interactions it is convenient to use an effective potential V_{eff} instead of the microscopic potential V. In many applications one introduces the regularized zero-range pseudo-potential defined as (Huang and Yang, 1957)

$$V_{eff}(\mathbf{r}) = g\delta(\mathbf{r})\frac{\partial}{\partial r}r \ , \tag{2.4}$$

where the coupling constant g is related to the scattering length by the relationship $g = 2\pi\hbar^2 a/m_r$. This potential has a range $R_0 = 0$ and results in the scattering amplitude $f(k) = -1/(a^{-1} + ik)$.

2.2 Feshbach Resonance

By changing an external magnetic field, it is possible to tune the scattering length a to the values much larger than the interatomic distance. This situation exists near the so called Fano-Feshbach resonances [29, 30]. These resonances take place when the energy associated with the scattering process between two particles (referred to as open channel) becomes close to the energy of a bound state of the pair in a different spin state (closed channel). For example, for spin-triplet and spin-singlet states, their magnetic moments are totally different. Thus the energy gap between spin-triplet open channel (free scattering) and spin-singlet closed channel (weakly bound state) can be tuned by using the external magnetic field. When the energy of the closed channel is close to the energy of the open channel, the free scattering process will have resonance with this weakly bound state, and the scattering length diverges. The transition between the two situations takes place at some value (denoted by B_0) of the magnetic field. In the absence of coupling, the existence of the bound state in the closed channel has no effect on the scattering in the open channel. However, in the presence of small coupling induced for example by exchange interactions, the scattering length will be large and positive if the state is below threshold and large and

negative in the opposite case. As a function of the magnetic field B the scattering length can be parametrized in the following form

$$a = a_{bg}\left(1 - \frac{\Delta_B}{B - B_0}\right) , \tag{2.5}$$

where Δ_B is the width of the resonance and a_{bg} is the background scattering length away from the resonance. We can see that a changes from positive to negative infinity as an increasing B across B_0, or vice versa. An example of Feshbach resonance of ^{6}Li is shown in Fig. 1.

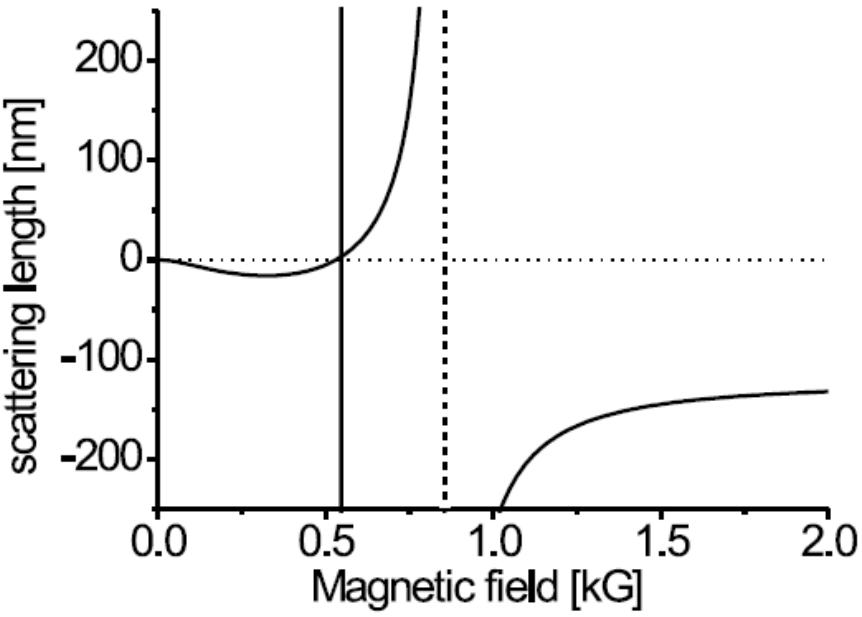

Figure 1: Magnetic field dependence of the scattering length in ^{6}Li, showing a broad Feshbach resonance at $B_0 \simeq 834$ G and a narrow Feshbach resonance at $B_0 \simeq 543$ G [1].

3.0 Finite-momentum Superfluidity and Phase Transitions in a p-wave Resonant Bose Gas

In this chapter, we will talk about the the superfluidity and phase transitions of resonant Bose gases with high order interactions [2]. Feshbach resonance (FR) has brought us the possibility to manipulate degenerate atomic gases in studies of highly coherent, interacting quantum many-body systems. We are able to finely control the two-body interactions by tuning with an external magnetic field through the atomic continuum[30, 31]. It has led to a realization of a long-sought-after s-wave paired superfluidity in bosonic[32, 33] and fermionic atomic gases[34, 35, 36]. Specifically, the successful realization of FR in fermioic atoms has proven the transition from Bardeen-Copper-Shrieffer regime (BCS) [37] to the Bose-Einstein condensate (BEC) regime.

The phenomenology of resonantly interacting degenerate bosonic atoms contrasts strongly and qualitatively with fermionic atoms. For a large positive detuning, molecules are strongly energetically suppressed and unpaired atoms (as in any bosonic system at zero temperature) form an atomic superfluid (ASF), exhibiting atomic off-diagonal long-range order (ODLRO), and the relative molecular modes are gapped. On the other side, for a large negative detuning, free atoms are strongly disfavored (gapped), pairing up into stable bosonic molecules. At $T = 0$, the atoms form a diatomic molecular superfluid (MSF) characterized by a molecular ODLRO. The MSF does not exhibit atomic ODLRO, nor the associated atomic superfluidity. Together with a gapped atomic excitation spectrum and correlation functions (characteristics that extend to finite temperature), these features qualitatively distinguish it from the ASF. And in an intermediate detuning, the atomic and molecular superfluids are possible to coexist, giving rise to gapless atomic and molecular spectrums [9, 11].

In a trapped, dilute atomic gas the existence of these qualitatively distinct superfluid phases should be most directly detectable through independent images of atomic and molecular density profiles. As illustrated in Fig. 2(a), the *atomic* component should exhibit a BEC peak in the ASF phase, that is absent in the MSF phase, shown in Fig. 2(b). Both superfluid phases are distinguished from the normal state by the BEC peak in the *molecular* density

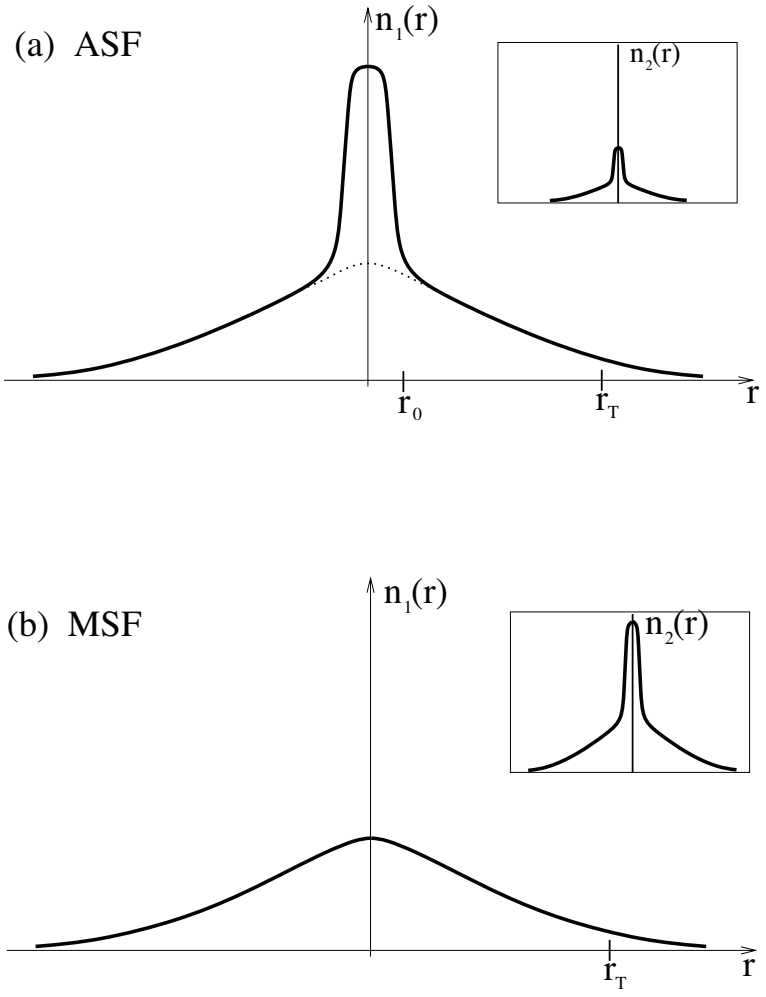

Figure 2: Atomic density profiles, $n_1(r)$ in (a) the ASF and (b) the MSF phases. These are distinguished by the presence and absence of atomic BEC peak, respectively. Each of these superfluid phases is distinguished from the "normal" (thermal) state by the BEC peak in the molecular density profile, $n_2(r)$, illustrated in insets. In the dilute limit, the quantum oscillator length r_0 of the BEC peak (set by the single-particle Gaussian ground state wavefunction), and the thermal oscillator length r_T of the thermal part of the atomic cloud [2].

profile, as illustrated in the insets to these figures. Consequently, as illustrated in Fig. 3, a thermodynamically sharp quantum phase transition, at an intermediate critical Feshbach resonance detuning ν_c, must separate the MSF and ASF phases. Each in turn is also separated by a finite-temperature transition from the "normal" (N) state lacking any order (i.e., breaking no symmetries). At zero temperature, two critical detunings separate the phases into MSF, AMSF and ASF phases.

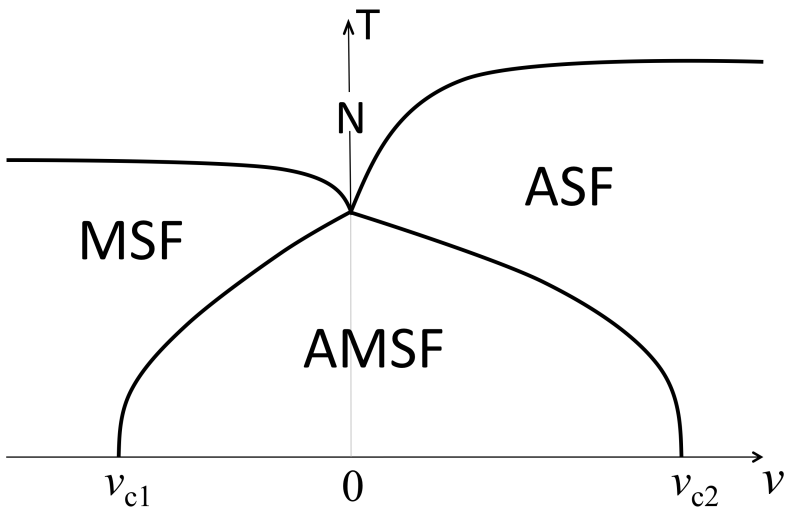

Figure 3: Schematic temperature-detuning phase diagram for a balanced two-species p-wave resonant Bose gas. As illustrated, it exhibits atomic (ASF), molecular (MSF), and atomic-molecular (AMSF) superfluid phases. The AMSF state is characterized by a p-wave, molecular, and finite-momentum Q atomic superfluidity.

3.1 Model

We study a gas mixture of two distinguishable bosonic atoms (e.g., ^{85}Rb, ^{87}Rb) [9], created by field operators $\psi_\sigma^\dagger(\mathbf{r}) = \left(\psi_1^\dagger(\mathbf{r}), \psi_2^\dagger(\mathbf{r})\right)$ and interacting through a p-wave FR associated with a tunable "closed"-channel bound state. The corresponding p-wave ($\ell = 1$) closed-channel hetero-molecule (e.g., ^{85}Rb-^{87}Rb) is created by a Cartesian vector field

operator $\boldsymbol{\phi}^\dagger(\mathbf{r}) = (\phi_x^\dagger, \phi_y^\dagger, \phi_z^\dagger)$, related to $\phi_\pm^\dagger = (\phi_x^\dagger \pm i\phi_y^\dagger)/\sqrt{2}, \phi_z^\dagger = \phi_z^\dagger$ operators, which create closed-channel molecules in the $\ell_z = \pm 1, 0$ eigenstates, respectively. This system is governed by a grand-canonical Hamiltonian density (with $\hbar = 1$ throughout),

$$\begin{aligned}\mathcal{H} &= \sum_{\sigma=1,2} \hat{\psi}_\sigma^\dagger(-\frac{1}{2m}\boldsymbol{\nabla}^2 - \mu_\sigma)\hat{\psi}_\sigma + \hat{\boldsymbol{\phi}}^\dagger \cdot (-\frac{1}{4m}\boldsymbol{\nabla}^2 - \mu_m)\cdot\hat{\boldsymbol{\phi}} + \mathcal{H}_{bg} \\ &+\frac{\alpha}{2}\left(\hat{\boldsymbol{\phi}}^\dagger \cdot \left[\hat{\psi}_1(-i\boldsymbol{\nabla})\hat{\psi}_2 - \hat{\psi}_2(-i\boldsymbol{\nabla})\hat{\psi}_1\right] + h.c.\right),\end{aligned} \tag{3.1}$$

with the effective molecular chemical potential,

$$\mu_m = \mu_1 + \mu_2 - \nu, \tag{3.2}$$

adjustable by a magnetic-field-dependent detuning ν, the latter being the rest energy of the closed-channel molecule relative to a pair of open-channel atoms. For simplicity we have taken atomic masses to be identical (a good approximation for the ^{85}Rb-^{87}Rb mixture that we have in mind) and will focus on the balanced case of $\mu_1 = \mu_2 = \mu$, with μ fixing the total number of ^{85}Rb and ^{87}Rb atoms.

The background (nonresonant) interaction density

$$\mathcal{H}_{bg} = \mathcal{H}_a + \mathcal{H}_m + \mathcal{H}_{am} \tag{3.3}$$

is given by

$$\mathcal{H}_a = \sum_{\sigma=1,2} \frac{\lambda_\sigma}{2}\hat{\psi}_\sigma^{\dagger 2}\hat{\psi}_\sigma^2 + \lambda_{12}\hat{\psi}_1^\dagger\hat{\psi}_2^\dagger\hat{\psi}_2\hat{\psi}_1, \tag{3.4a}$$

$$\mathcal{H}_m = \frac{g_1}{2}(\hat{\boldsymbol{\phi}}^\dagger\cdot\hat{\boldsymbol{\phi}})^2 + \frac{g_2}{2}|\hat{\boldsymbol{\phi}}\cdot\hat{\boldsymbol{\phi}}|^2, \tag{3.4b}$$

$$\mathcal{H}_{am} = \sum_{\sigma=1,2} g_{am}\hat{\psi}_\sigma^\dagger\hat{\boldsymbol{\phi}}^\dagger\cdot\hat{\boldsymbol{\phi}}\hat{\psi}_\sigma, \tag{3.4c}$$

where coupling constants λ_σ, λ_{12}, $g_{1,2}$, g_{am} are related to the corresponding background s-wave scattering lengths (a_1, a_2, etc.) in a standard way and thus are fixed experimentally through measurements on the gas in a dilute limit. Correspondingly, we take these background s-wave couplings to be independent of the p-wave detuning, an approximation that we expect to be quantitatively valid in the narrow resonance and/or dilute limits considered here.

The above two-channel model, Eq. (3.1), faithfully captures the low-energy p-wave resonant and s-wave nonresonant scattering phenomenology of the ^{85}Rb-^{87}Rb p-wave Feshbach-resonant mixture. Its analysis at nonzero balanced atomic densities, which is our focus here, leads to the predictions summarized in the previous section.

3.2 Mean-field Theory

The order parameters for the system are characterized here. The atomic condensates $\Psi_1(\mathbf{r})$ and $\Psi_2(\mathbf{r})$ need to be complex periodic functions characterized by momenta $\boldsymbol{Q}_n$, with the simplest single $\boldsymbol{Q}_1 = \boldsymbol{Q}$ form given by

$$\psi_1(\mathbf{r}) \rightarrow \Psi_1(\mathbf{r}) = \Psi_{1,\boldsymbol{Q}} e^{i\boldsymbol{Q}\cdot\mathbf{r}}, \tag{3.5a}$$

$$\psi_2(\mathbf{r}) \rightarrow \Psi_2(\mathbf{r}) = \Psi_{2,-\boldsymbol{Q}} e^{-i\boldsymbol{Q}\cdot\mathbf{r}}, \tag{3.5b}$$

$$\boldsymbol{\phi}(\mathbf{r}) \rightarrow \boldsymbol{\Phi}, \tag{3.5c}$$

where $\boldsymbol{\Phi}$ is a complex 3-vector order parameter characteristic of the $\ell = 1$ molecular condensate and the choice of $\pm\boldsymbol{Q}$ momentum relation for the two atomic condensate fields is dictated by momentum conservation. In general, we decompose the molecular order parameters in terms of orthonormal real 3-vectors $\mathbf{u}$ and $\mathbf{v}$

$$\boldsymbol{\Phi} = \mathbf{u} + i\mathbf{v}. \tag{3.6}$$

We next consider the Landau free energy as a function of these atomic and molecular order parameters and, by minimizing it for a range of experimentally tunable parameters, compute the mean-field phase diagram for this p-wave resonant two-component Bose gas.

Atomic superfluid phase : For large positive detuning, ν, the molecular chemical potential $\mu_m < 0$ is negative, with molecules gapped and therefore the ground state is a molecular vacuum. We can thus safely integrate out the small Gaussian molecular excitations, leading to an effective atomic free energy, $F[\Psi_\sigma, \boldsymbol{\Phi}]$ by setting $\boldsymbol{\Phi} = 0$. This functional is a special $U(1) \otimes U(1)$ form of a $O(N) \otimes O(M)$ model. This free energy is clearly minimized by a spatially uniform atomic order parameter, Ψ_σ, giving

$$f_{\rm asf} = F[\Psi_\sigma, 0]/V = \sum_{\sigma=1,2} \big[-\mu_\sigma |\Psi_\sigma|^2 + \frac{\lambda_\sigma}{2}|\Psi_\sigma|^4\big] + \lambda_{12}|\Psi_1|^2|\Psi_2|^2 \tag{3.7}$$

as the ASF free-energy density.

A minimization of $f_{\rm asf}$, leads to four states corresponding to condensed and normal (nonsuperfluid) combinations of the two-component Bose gas. For both negative chemical potentials, $\mu_1 < 0$, $\mu_2 < 0$, both atoms are in the noncondensed, normal (N) phase, $|\Psi_1| = |\Psi_2| = 0$. As physical parameters are varied (e.g., a weaker periodic potential, lower temperature, and higher density for one of the atomic species) for asymmetric mixture (different densities and/or masses), one of the two atomic chemical potentials, μ_1, μ_2 can turn positive, leading to a conventional normal-superfluid transition to $\rm ASF_1$ or $\rm ASF_2$ states, respectively. The order parameters and mean-field phase boundaries in each of these conventional single-component atomic BECs are given by

$$\text{ASF}_1\text{:} \quad \Psi_1 = \sqrt{\frac{\mu_1}{\lambda_1}}, \Psi_2 = 0, \text{for } \mu_1 > 0,\ \mu_2 < \frac{\lambda_{12}}{\lambda_1}\mu_1, \tag{3.8a}$$

$$\text{ASF}_2\text{:} \quad \Psi_1 = 0, \Psi_2 = \sqrt{\frac{\mu_2}{\lambda_2}}, \text{for } \mu_2 > 0,\ \mu_1 < \frac{\lambda_{12}}{\lambda_2}\mu_2. \tag{3.8b}$$

We note that generically for a symmetric two-component Bose mixture, these phases will be avoided by symmetry. Further changes in the system's parameters, so as to drive both chemical potentials positive, for $\lambda_1\lambda_2 > \lambda_{12}^2$ leads to $\rm ASF_1$ - $\rm ASF_{12}$ or $\rm ASF_2$ - $\rm ASF_{12}$ transitions. The resulting two-component condensate, $\rm ASF_{12}$, is characterized by two nonzero atomic condensates and mean-field phase boundaries given by

$$\begin{aligned} &\text{ASF}_{12}\text{:} \\ &\Psi_1 = \left[\frac{\lambda_2\mu_1 - \lambda_{12}\mu_2}{\lambda_1\lambda_2 - \lambda_{12}^2}\right]^{\frac{1}{2}}, \Psi_2 = \left[\frac{\lambda_1\mu_2 - \lambda_{12}\mu_1}{\lambda_1\lambda_2 - \lambda_{12}^2}\right]^{\frac{1}{2}}, \\ &\text{for } \mu_1 > 0, \mu_2 > 0, \frac{\lambda_2}{\lambda_{12}} > \frac{\mu_2}{\mu_1} > \frac{\lambda_{12}}{\lambda_1}. \end{aligned} \tag{3.9}$$

These classical phase transitions are generically continuous, in the XY universality class, breaking the associated $U(1)$ symmetries. The N-ASF$_{12}$ transition only takes place in a fine-tuned balanced mixture $\mu_1 = \mu_2$ (which is our primarily focus here) going directly through a tetracritical point, $\mu_1 = \mu_2 = 0$.

For $\lambda_1\lambda_2 < \lambda_{12}^2$, the ASF$_1$ and ASF$_2$ energies cross before either becomes locally unstable. Consequently, instead of continuous transitions to the ASF$_{12}$ state, the two-component ASF$_{12}$ is absent and the ASF$_1$ and ASF$_2$ phases are separated by a first-order transition, located at

$$\mu_2 = \sqrt{\frac{\lambda_2}{\lambda_1}}\mu_1 \tag{3.10}$$

which terminates at a bicritical point. On this critical line the ASF$_1$ and ASF$_2$ states coexist and spatially phase separate.

Molecular superfluid phase : In the opposite limit of large negative detuning, open-channel atoms are gapped and the ground state is an atomic vacuum. Hence, for $\mu < 0$ the free energy $F[\Psi_\sigma, \mathbf{\Phi}]$ is minimized by $\Psi_\sigma = 0$ and a uniform molecular condensate $\mathbf{\Phi}$. The free-energy density then reduces to

$$f_{\rm msf}[\mathbf{\Phi}] = F[0, \mathbf{\Phi}] = -\mu_m|\mathbf{\Phi}|^2 + \frac{g_1}{2}|\mathbf{\Phi}^*\cdot\mathbf{\Phi}|^2 + \frac{g_2}{2}|\mathbf{\Phi}\cdot\mathbf{\Phi}|^2, \tag{3.11a}$$

$$= -\mu_m(u^2+v^2) + \frac{g_1}{2}(u^2+v^2)^2 + \frac{g_2}{2}(u^2-v^2)^2. \tag{3.11b}$$

The minimization of $f_{\rm msf}[\mathbf{\Phi}]$ then leads to two superfluid phases, the MSF$_{\rm p}$ for $g_2 < 0$ and the MSF$_{\rm fm}$ for $g_2 > 0$ molecular condensates,

$$\mathbf{\Phi} = \sqrt{\frac{\mu_m}{g_1+g_2}}\hat{\boldsymbol{n}} = \Phi_{\rm p}\hat{\boldsymbol{n}}, \quad \text{for } g_2 < 0, \tag{3.12}$$

$$\mathbf{\Phi} = \sqrt{\frac{\mu_m}{2g_1}}(\hat{\boldsymbol{n}} + i\hat{\boldsymbol{m}}) = \frac{\Phi_{\rm fm}}{\sqrt{2}}(\hat{\boldsymbol{n}} + i\hat{\boldsymbol{m}}), \quad \text{for } g_2 > 0. \tag{3.13}$$

For polar MSF, it spans the $[U(1)\times S_2]/\mathbb{Z}_2$ manifold of degenerate ground states. For ferromagnetic MSF, it spans the $SO(3)$ manifold of states. In the above equation, $\hat{\boldsymbol{n}}, \hat{\boldsymbol{m}}, \hat{\boldsymbol{l}} \equiv \hat{\boldsymbol{n}}\times\hat{\boldsymbol{m}}$ is an orthonormal triad and $\Phi_{\rm p,fm}$ are complex order-parameter amplitudes, breaking the $SO(3)\times U_N(1)$ symmetry of the disordered phase.

Atomic molecular superfluid phase : For the intermediate detuning, we consider a condensation of both atoms and molecules, for generality allowing atoms to condense at a nonzero momentum. We focus on the simpler case of a single momentum, $\boldsymbol{Q}$ atomic condensate, that we also find to be the preferred form of the AMSF state. We relegate to Appendix A the conceptually straightforward, but technically slightly involved, analysis of the more general $\pm\boldsymbol{Q}$ momenta state.

Using the order parameter form from Eqs. (3.5a), (3.5b), and (3.5c) inside the mean-field free-energy density $f_{\rm amsf} = F[\Psi_\sigma, \mathbf{\Phi}]/V = f_Q + f_{\rm msf}$, we obtain

$$\begin{aligned} f_Q &= \varepsilon_Q \left(\Psi^*_{1,\boldsymbol{Q}}\Psi_{1,\boldsymbol{Q}} + \Psi^*_{2,-\boldsymbol{Q}}\Psi_{2,-\boldsymbol{Q}}\right) - \Delta_{\boldsymbol{Q}}\Psi^*_{1,\boldsymbol{Q}}\Psi^*_{2,-\boldsymbol{Q}} - \Delta^*_{\boldsymbol{Q}}\Psi_{1,\boldsymbol{Q}}\Psi_{2,-\boldsymbol{Q}} \\ &\quad + \frac{\lambda_1}{2}|\Psi_{1,\boldsymbol{Q}}|^4 + \frac{\lambda_2}{2}|\Psi_{2,-\boldsymbol{Q}}|^4 + \lambda_{12}|\Psi_{1,\boldsymbol{Q}}|^2|\Psi_{2,-\boldsymbol{Q}}|^2, \end{aligned} \tag{3.14}$$

where $\varepsilon_Q = \frac{Q^2}{2m} - \mu + g_{am}|\mathbf{\Phi}|^2$, $\Delta_{\boldsymbol{Q}} = \alpha\mathbf{\Phi}\cdot\boldsymbol{Q} \equiv |\Delta_{\boldsymbol{Q}}|e^{i\varphi_0}$, and for simplicity we specialized to a balanced mixture set by $\mu_1 = \mu_2 = \mu$. Due to the quartic formula of atomic mean field, it is generally difficult to derive the mean-field ground states. But it is possible to approach the AMSF phase from MSF phase, where the atomic condensate density is relatively small, and thus we can ignore the quartic terms effect. Without loss of generosity, we assume $u > v$, and the minimization of the free energy density leads to

$$Q_0 = \alpha m u \approx \alpha m\sqrt{n_m}. \tag{3.15}$$

In the meanwhile, the sign of g_2 strongly affects the composition of u and v. A straightforward minimization of $f_{\rm amsf}$, for $g_2 < 0$, leads to the $\mathrm{AMSF_p}$ phase, characterized by order parameters,

$$u_p = \sqrt{\frac{\lambda\mu_m - \tilde{g}_{am}\mu}{\lambda(g_1+g_2) - \tilde{g}^2_{am}}}, \quad v_p = 0, \tag{3.16a}$$

$$|\Psi_{1(2),p}| = \sqrt{\frac{(g_1+g_2)\mu - \tilde{g}_{am}\mu_m}{2\lambda(g_1+g_2) - 2\tilde{g}^2_{am}}}, \tag{3.16b}$$

where $\tilde{g}_{am} = g_{am} - m\alpha^2/2$. The phase boundaries corresponding to the $\mathrm{MSF_p}$ - $\mathrm{AMSF_p}$ and $\mathrm{AMSF_p}$ - ASF transitions are given by

$$\nu_{\mathrm{c}}^{\mathrm{MSF_p-AMSF_p}} = -\left(g_1 + g_2 - 2\tilde{g}_{am}\right) n_m, \tag{3.17a}$$

$$\nu_{\mathrm{c}}^{\mathrm{AMSF_p-ASF}} = \left(2\lambda - \tilde{g}_{am}\right) n_a, , \tag{3.17b}$$

Within the mean-field approximation, the $\mathrm{MSF_p}$-$\mathrm{AMSF_p}$ and $\mathrm{AMSF_p}$-ASF transitions are of second order. The phase transition figure is shown in Fig. 4

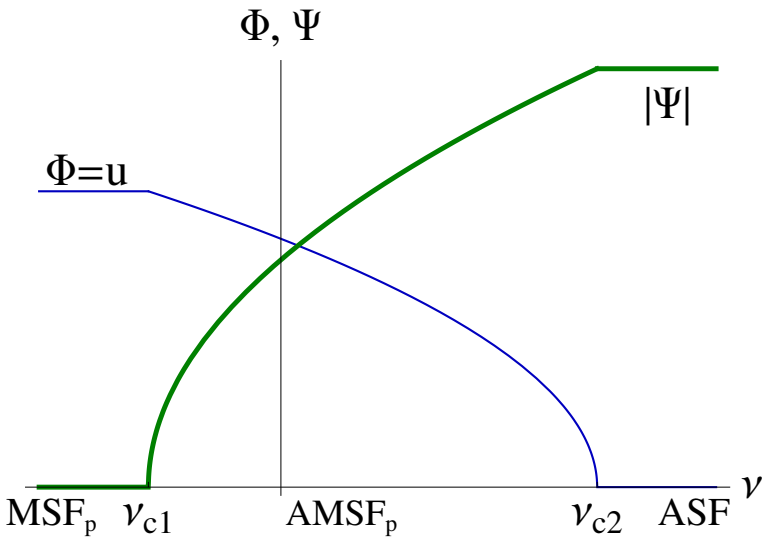

Figure 4: (Color online) Schematic atomic (thick) and molecular (thin) order parameters versus the FR detuning ν for the polar phase, with $\nu_{\mathrm{c1}} = \nu_{\mathrm{c}}^{\mathrm{MSF_p-AMSF_p}}$ and $\nu_{\mathrm{c2}} = \nu_{\mathrm{c}}^{\mathrm{AMSF_p-ASF}}$.

For $g_2 > 0$, a minimization of the free energy, f_{amsf} for a range of couplings shows that for intermediate detuning, the low-temperature state is the ferromagnetic $\mathrm{AMSF_{fm}}$,

characterized by

$$u_{fm} = \sqrt{\frac{2\lambda g_2\mu_m - g_{am}^2\mu_m - (g_1+g_2)\tilde{g}_{am}\mu + (g_1-g_2)g_{am}\mu + g_{am}\tilde{g}_{am}\mu_m}{4\lambda g_1 g_2 - 4g_2 g_{am}\tilde{g}_{am} - (g_1+g_2)(m\alpha^2/2)^2}}, \tag{3.18a}$$

$$v_{fm} = \sqrt{\frac{2\lambda g_2\mu_m - \tilde{g}_{am}^2\mu_m - (g_1+g_2)g_{am}\mu + (g_1-g_2)\tilde{g}_{am}\mu + g_{am}\tilde{g}_{am}\mu_m}{4\lambda g_1 g_2 - 4g_2 g_{am}\tilde{g}_{am} - (g_1+g_2)(m\alpha^2/2)^2}}, \tag{3.18b}$$

$$|\Psi_{1(2),fm}| = \sqrt{\frac{g_2(4g_1\mu - 4g_{am}\mu_m + m\alpha^2\mu_m)}{4\lambda g_1 g_2 - 4g_2 g_{am}\tilde{g}_{am} - (g_1+g_2)(m\alpha^2/2)^2}}. \tag{3.18c}$$

The behavior of these order parameters as a function of detuning, ν, is illustrated in Fig. 5. With increasing detuning, the component v (being smaller than u) vanishes first, signaling a transition of the ferromagnetic $\mathrm{AMSF_{fm}}$ to the polar $\mathrm{AMSF_p}$ state. Depending on the value of other parameters, upon further increase of ν the system either continuously transitions at $\nu_c^{\mathrm{AMSF_p-ASF}}$ to one of the three ASF states or undergoes a first-order $\mathrm{AMSF_{fm}}$-ASF transition with u discontinuously jumping to zero when v vanishes.

The detuning phase boundaries corresponding to the $\mathrm{MSF_{fm}}$ - $\mathrm{AMSF_{fm}}$ and the $\mathrm{AMSF_{fm}}$ - $\mathrm{AMSF_p}$ transitions, determined by a vanishing of the atomic and the v (transverse to $\boldsymbol{Q}_0$) component of the molecular condensates, respectively, are given by

$$\nu_c^{\mathrm{MSF_{fm}-AMSF_{fm}}} = -\left(g_1 - 2g_{am} + m\alpha^2/2\right)n_m, \tag{3.19a}$$

$$\nu_c^{\mathrm{AMSF_{fm}-AMSF_p}} = \frac{8\lambda g_2 + g_{am}\left(2m\alpha^2 - 4g_2\right) - m\alpha^2\left(g_1 - g_2 + m\alpha^2\right)}{4g_2 + 2m\alpha^2} n_a. \tag{3.19b}$$

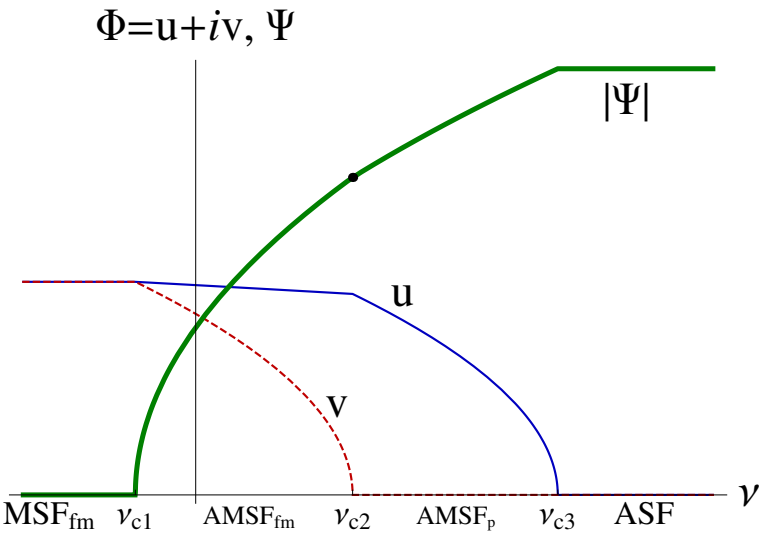

Figure 5: Schematic atomic (thick) and molecular (thin and dashed) order parameters versus the FR detuning ν for ferromagnetic phases. The AMSF$_{\rm fm}$-AMSF$_{\rm p}$ phase transition at ν_{c2} leads to kinks (change in slope) in the molecular (u) and atomic (Ψ) order parameter, later indicated by a black dot. Without loss of generality we choose the $\hat{n}$ axis (component of u) to lie along $\boldsymbol{Q}_0$. The critical detunings are denoted by $\nu_{\rm c1} = \nu_{\rm c}^{\rm MSF_{fm}-AMSF_{fm}}$, $\nu_{\rm c2} = \nu_{\rm c}^{\rm AMSF_{fm}-AMSF_{p}}$, and $\nu_{\rm c3} = \nu_{\rm c}^{\rm AMSF_{p}-ASF}$.

3.3 Elementory Excitations

We study quantum fluctuations within each of the ASF, MSF and AMSF classes of phases established above. To this end we expand the atomic and molecular bosonic operators around their mean-field condensate values $\psi_\sigma = \Psi_\sigma + \delta\psi_\sigma, \phi_i = \Phi_i + \delta\phi_i$, where $\delta\psi_\sigma$ ($\sigma = 1, 2$) are fluctuation fields for atoms of flavors 1 and 2, respectively, and $\delta\phi_i$ ($i = x, y, z$) are triplet of the $\ell = 1$ molecular fluctuation fields. It is convenient to work in momentum space,

$$\delta\psi_\sigma = \frac{1}{\sqrt{V}} \sum_{\boldsymbol{k}} a_{\sigma,\boldsymbol{k}}\, e^{i\boldsymbol{k}\cdot\boldsymbol{r}}, \tag{3.20a}$$

$$\delta\phi_i = \frac{1}{\sqrt{V}} \sum_{\boldsymbol{k}} b_{i,\boldsymbol{k}}\, e^{i\boldsymbol{k}\cdot\boldsymbol{r}}. \tag{3.20b}$$

Using the above momentum representation inside the Hamiltonian, Eq. (3.1) and expanding to second order in the fluctuations operators $a_{\sigma,\boldsymbol{k}}$, $b_{i,\boldsymbol{k}}$, we obtain $H = H_{\rm mft}[\Psi_\sigma, \boldsymbol{\Phi}] + H_f$, with

$$\begin{aligned} H_f =& \sum_{\boldsymbol{k}} \Bigg[\sum_{\sigma=1,2} \left(\frac{1}{2} \tilde{\varepsilon}_{\sigma,\boldsymbol{k}+\boldsymbol{Q}_\sigma} a^\dagger_{\sigma,\boldsymbol{k}+\boldsymbol{Q}_\sigma} a_{\sigma,\boldsymbol{k}+\boldsymbol{Q}_\sigma} + \tilde{\lambda}_\sigma a_{\sigma,-\boldsymbol{k}+\boldsymbol{Q}_\sigma} a_{\sigma,\boldsymbol{k}+\boldsymbol{Q}_\sigma} \right) + t_1 a^\dagger_{1,\boldsymbol{k}+\boldsymbol{Q}} a_{2,\boldsymbol{k}-\boldsymbol{Q}} \\ &+ t_{2,\boldsymbol{k}+\boldsymbol{Q}} a_{1,\boldsymbol{k}+\boldsymbol{Q}} a_{2,-\boldsymbol{k}-\boldsymbol{Q}} + \sum_{i=x,y,z} \left(\frac{1}{2} \tilde{\omega}_{i,\boldsymbol{k}} b^\dagger_{i,\boldsymbol{k}} b_{i,\boldsymbol{k}} + \delta_i b_{i,-\boldsymbol{k}} b_{i,\boldsymbol{k}} \right) \\ &+ \frac{1}{2} \sum_{i,j=x,y,z, i\neq j} \left(g_{ij} b^\dagger_{j,\boldsymbol{k}} b_{i,\boldsymbol{k}} + \gamma_{ij} b_{i,-\boldsymbol{k}} b_{j,\boldsymbol{k}} \right) - \sum_\sigma \boldsymbol{\alpha}_{\overline{\sigma},\boldsymbol{k}} \cdot \mathbf{b}^\dagger_{\boldsymbol{k}} a_{\sigma,\boldsymbol{k}+\boldsymbol{Q}_\sigma} + h.c. \Bigg], \qquad (3.21a) \\ \equiv& \sum_{\boldsymbol{k},\alpha,\beta} c^\dagger_{\alpha,\boldsymbol{k}} \tilde{h}^{\alpha\beta}_{\boldsymbol{k}} c_{\beta,\boldsymbol{k}} \qquad (3.21b) \end{aligned}$$

where $\tilde{h}^{\alpha\beta}_{\boldsymbol{k}}$ is a Bogoliubov Hamiltonian matrix defined by matrix elements

$$\begin{aligned} \tilde{\varepsilon}_{\sigma,\mathbf{k}} &= \epsilon_{\mathbf{k}} - \mu_\sigma + 2\lambda_\sigma |\Psi_\sigma|^2 + \lambda_{12} |\Psi_{\overline{\sigma}}|^2 + g_{am} |\boldsymbol{\Phi}|^2, \qquad (3.22a) \\ \tilde{\omega}_{i,\mathbf{k}} &= \frac{1}{2}\epsilon_{\mathbf{k}} - \mu_m + g_1 |\boldsymbol{\Phi}|^2 + (g_1 + 2g_2) |\Phi_i|^2, \\ &\quad + g_{am}(|\Psi_1|^2 + |\Psi_2|^2), \qquad (3.22b) \\ \tilde{\lambda}_\sigma &= \frac{1}{2}\lambda_\sigma \Psi^{*2}_\sigma, \qquad (3.22c) \\ t_1 &= \lambda_{12} \Psi_1 \Psi^*_2, \qquad (3.22d) \\ t_{2,\boldsymbol{k}} &= \lambda_{12} \Psi^*_1 \Psi^*_2 - \alpha \boldsymbol{\Phi}^* \cdot \boldsymbol{k}, \qquad (3.22e) \\ \delta_i &= \frac{1}{2} g_1 \Phi^*_i \Phi^*_i + \frac{1}{2} g_2 \boldsymbol{\Phi}^* \cdot \boldsymbol{\Phi}^*, \qquad (3.22f) \\ g_{ij} &= g_1 \Phi^*_i \Phi_j + 2 g_2 \Phi^*_i \Phi_j, \qquad (3.22g) \\ \gamma_{ij} &= \frac{1}{2} g_1 \Phi^*_i \Phi^*_j, \qquad (3.22h) \\ \boldsymbol{\alpha}_{\sigma=(1,2),\boldsymbol{k}} &= \pm \alpha \Psi_{\sigma,\boldsymbol{Q}_\sigma} (\boldsymbol{Q}_\sigma - \boldsymbol{k}/2), \qquad (3.22i) \end{aligned}$$

where $\epsilon_{\mathbf{k}} = \frac{k^2}{2m}$, $\overline{1} = 2, \overline{2} = 1$. A diagonalization of this ten-dimensional Bogoliubov Hamiltonian, preserving bosonic commutation relations of the $c_{\alpha,\boldsymbol{k}}$ components gives the spectrum of the five modes throughout the phase diagram.

Atomic superfluid excitation: In the ASF phase, we consider the case where both atom species condense. Standard analysis, consistent with two $U(1)$ symmetries spontaneously

broken, then leads to two gapless atomic Bogoliubov sound modes for species 1 and 2. Together with the gapped molecular excitations this leads to spectra of the five modes:

$$E_{k1}^{(a_{12})} = \sqrt{\frac{k^2}{2m}\Big(\frac{k^2}{2m}+2\lambda n\Big)}, \tag{3.23a}$$

$$E_{k2}^{(a_{12})} \simeq c^{(a_{12})}k, \tag{3.23b}$$

$$E_{k1}^{(m_{12})} = E_{k2}^{(m_{12})} = \frac{k^2}{4m}+\nu-2\lambda n+g_{am}n, \tag{3.23c}$$

$$E_{k3}^{(m_{12})} \simeq \frac{k^2}{4m^*}+\nu-2\lambda n+g_{am}n, \tag{3.23d}$$

where for $E_{k2}^{(a_{12})}$ and $E_{k3}^{(m_{12})}$ we took $k\to 0$ and $\alpha\to 0$ limit and defined the sound velocity and effective atomic mass:

$$c^{(a_{12})} = \sqrt{\frac{(\lambda-\lambda_{12})n}{m}}-\frac{3n\alpha^2\sqrt{(\lambda-\lambda_{12})mn}}{4(\nu-2\lambda n+g_{am}n)}, \tag{3.24a}$$

$$\frac{1}{m^*} = \frac{1}{m}+\frac{3(\nu-(\lambda+\lambda_{12})n+g_{am}n)n\alpha^2}{(\nu-2\lambda n+g_{am}n)^2}. \tag{3.24b}$$

$E_{k1}^{(a_{12})}$ and $E_{k2}^{(a_{12})}$ are atomlike and gapless modes respectively. $E_{k2}^{(a_{12})}$ and $E_{k3}^{(m_{12})}$ are modified by the FR interaction between atoms and molecules. The schematic plot of the excitations is shown in Fig. 6. The ASF-AMSF phase boundary is determined by the point where the molecular gap

$$E_{\rm gap}^{\rm ASF} = \nu-2\lambda n+g_{am}n \tag{3.25}$$

closes, and is consistent with the critical detuning determined by the development of the molecular order parameter that we found in the mean-field calculations.

Molecular superfluid excitation: For large negative detuning, both atomic species are gapped, and p-wave molecules are condensed into one of the two $\ell_z=0$ $\mathrm{MSF_p}$ and $\ell_z=\pm 1$ $\mathrm{MSF_{fm}}$. To see this, we note that the atomic Bogoliubov excitations are gapped and can therefore be integrated out. Neglecting these small effects, the vanishing of $\boldsymbol{\alpha}_{\sigma,\boldsymbol{k}}=\pm\alpha\Psi_{\sigma,\boldsymbol{Q}_\sigma}(\boldsymbol{Q}_\sigma-\boldsymbol{k}/2)=0$ decouples the Hamiltonian, $H_f=H_a+H_m$ into atomic and molecular parts, that then are straightforwardly diagonalized.

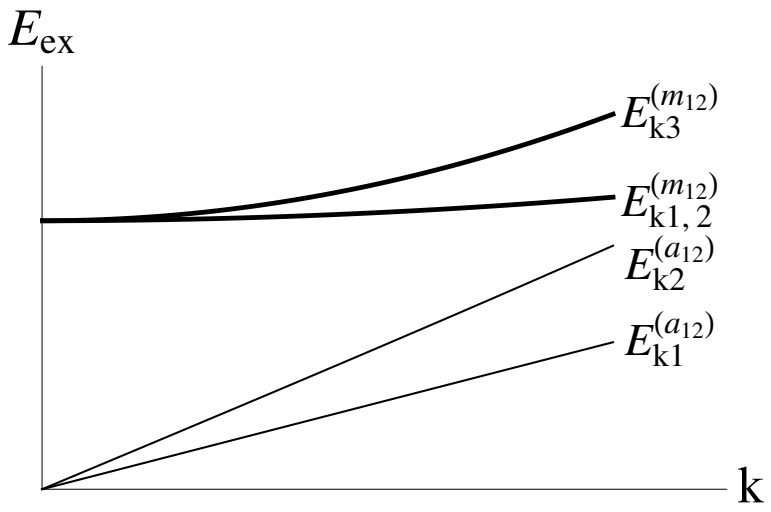

Figure 6: Schematic ASF double BEC (ASF_{12}) excitation spectrum. There are two gapless atomic Bogoliubov modes (thin) as well as three gapped molecular modes (thick).

The atomic sector, H_a is of standard Bogoliubov form, simplified to a 2×2 form by $t_1 = \tilde{\lambda}_\sigma = 0$ inside the MSF phases, leading to the atomic excitation spectrum, that for the symmetric case of $\mu_1 = \mu_2 \equiv \mu$ is given by

$$E_{a,\boldsymbol{k}}^{\rm MSF} = \sqrt{(\tilde{\varepsilon}_{\boldsymbol{k}} + |\alpha \boldsymbol{\Phi} \cdot \boldsymbol{k}|)(\tilde{\varepsilon}_{\boldsymbol{k}} - |\alpha \boldsymbol{\Phi} \cdot \boldsymbol{k}|)}, \tag{3.26}$$

where $\tilde{\varepsilon}_{\boldsymbol{k}} = k^2/2m - \mu + g_{am}|\boldsymbol{\Phi}|^2$. One key observation is that inside the MSF phases the atomic spectrum, $E_{a,\boldsymbol{k}}^{\rm MSF}$ (degenerate for $\sigma = 1, 2$ species) develops a minimum at a nonzero momentum $\boldsymbol{k}_{\rm min} = \boldsymbol{Q}_{\rm p,fm}$, with the corresponding atomic gap minimum, $E_{a,\rm gap}^{\mathrm{MSF_{p,fm}}}$, given by a value dependent on the nature of the $\mathrm{MSF_{p,fm}}$ phase.

When $g_2 < 0$, we have $\boldsymbol{\Phi} = \boldsymbol{u} = \Phi_{\rm p}\hat{\boldsymbol{n}}$, with $n_m = |\Phi_{\rm p}|^2$. For the symmetric case $\mu_1 = \mu_2 = \mu$, the atomic spectrum minimum is characterized by

$$k_{\rm min} = \alpha m \sqrt{n_m}, \tag{3.27a}$$

$$E_{\rm gap}^{(\mathrm{MSF_p,a})} = -\mu + g_{am} n_m - \frac{m\alpha^2 n_m}{2}, \tag{3.27b}$$

where in an isotropic trap the orientation of $\boldsymbol{k}_{\min}$ is spontaneously chosen. The $\mathrm{MSF_p}$-$\mathrm{AMSF_p}$ phase transition boundary is set by the closing of this atomic gap and is given by

$$\nu_c^{\mathrm{MSF_p}-\mathrm{AMSF_p}} = -\left(g_1 + g_2 - 2g_{am} + m\alpha^2\right) n_m. \tag{3.28}$$

Reassuringly, this is identical to the critical detuning for this phase boundary as we obtained in the mean-field analysis.

The diagonalization of molecular part H_m leads to three Bogoliubov-type dispersions,

$$\begin{aligned} E_{\parallel,k}^{\mathrm{MSF_p}} &= \frac{1}{2}\sqrt{\epsilon_{\boldsymbol{k}}^2 + 4(g_1+g_2)n_m\epsilon_{\boldsymbol{k}}}, && \text{(3.29a)} \\ &\simeq \sqrt{\frac{(g_1+g_2)n_m}{2m}}k, && \text{(3.29b)} \\ E_{\perp,k}^{\mathrm{MSF_p}} &= \frac{1}{2}\sqrt{\epsilon_{\boldsymbol{k}}^2 + 4|g_2|n_m\epsilon_{\boldsymbol{k}}}, && \text{(3.29c)} \\ &\simeq \sqrt{\frac{|g_2|n_m}{2m}}k, && \text{(3.29d)} \end{aligned}$$

where the longitudinal mode, $E_{\parallel,k}^{\mathrm{MSF_p}}$ describes the conventional MSF phase fluctuations and the doubly degenerate transverse mode, $E_{\perp,k}^{\mathrm{MSF_p}}$ is the dispersion for the $\ell = 1$ molecular orientational spin-waves. The schematic plot of the excitations is shown in Fig. 7.

When $g_2 > 0$, inside the $\mathrm{MSF_{fm}}$ state, the molecular condensate order parameter is given by $\boldsymbol{\Phi} = \frac{\Phi_{\mathrm{fm}}}{\sqrt{2}}(\hat{\boldsymbol{n}} + i\hat{\boldsymbol{m}})$, expressed in terms of an orthonormal triad, $\hat{\boldsymbol{n}} \times \hat{\boldsymbol{m}} = \hat{\boldsymbol{\ell}}$. To lowest order, the atomic spectrum inside $\mathrm{MSF_{fm}}$ has identical structure as that of the $\mathrm{MSF_p}$ state, Eq. (3.29), but with the replacement $g_1 + g_2 \to g_1$ and $\alpha^2 \to \alpha^2/2$,

$$\begin{aligned} k_{\min} &= \frac{1}{\sqrt{2}}\alpha m\sqrt{n_m}, && \text{(3.30a)} \\ E_{\mathrm{gap}}^{(\mathrm{MSF_{fm}},\mathrm{a})} &= -\mu + g_{am}n_m - \frac{m\alpha^2 n_m}{4}. && \text{(3.30b)} \end{aligned}$$

The $\mathrm{MSF_{fm}}$-$\mathrm{AMSF_{fm}}$ phase transition boundary is determined by the vanishing of the atomic gap, and is given by

$$\nu_c^{\mathrm{MSF_{fm}}-\mathrm{AMSF_{fm}}} = -\left(g_1 - 2g_{am} + \frac{1}{2}m\alpha^2\right) n_m, \tag{3.31}$$

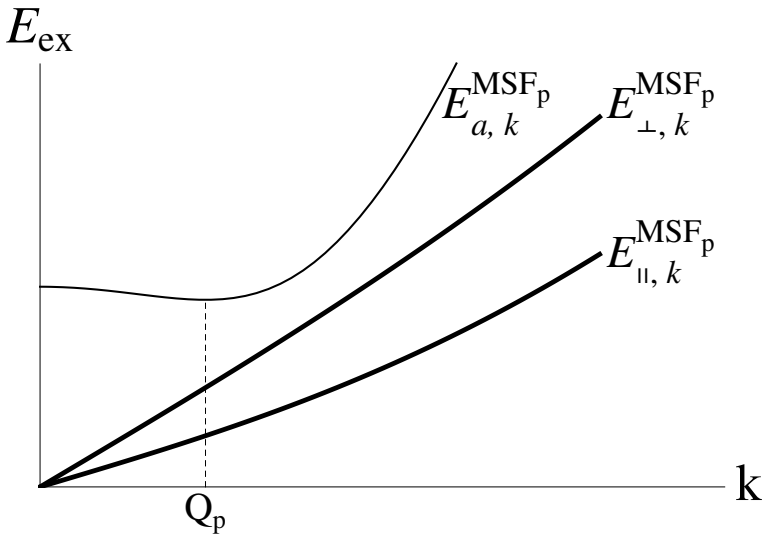

Figure 7: Schematic excitation spectrum for the $\mathrm{MSF_p}$. The doubly degenerate atomic spectrum (upper thin curve) exhibits a minimum gap at nonzero k, a precursor of finite-momentum atomic condensation inside the $\mathrm{AMSF_p}$. The molecular spectra (thick curves), one longitudinal (lowest) and two degenerate transverse (middle) modes, are of Bogoliubov type.

identical to the critical detuning obtained from mean-field theory for the order parameter in the mean-field analysis. Diagonalization of the above Hamiltonian then gives the following spectrum

$$E^{\mathrm{MSF_{fm}}}_{z,k} = \frac{1}{2}\epsilon_{\boldsymbol{k}} = \frac{k^2}{4m}, \tag{3.32a}$$

$$E^{\mathrm{MSF_{fm}}}_{+,k} = \frac{1}{2}\epsilon_{\boldsymbol{k}} + 2g_2 n_m, \tag{3.32b}$$

$$E^{\mathrm{MSF_{fm}}}_{-,k} = \frac{1}{2}\sqrt{\epsilon^2_{\boldsymbol{k}} + 4g_1 n_m \epsilon_{\boldsymbol{k}}}, \tag{3.32c}$$

$$\simeq \sqrt{\frac{g_1 n_m}{2m}}k, \tag{3.32d}$$

We note that despite a three-dimensional coset space, $SO(3)$ characterizing $\mathrm{MSF_{fm}}$, only two modes (linear and quadratic in k) exhibit a spectrum that vanishes in $k \to 0$ limit. The

spectrum $E^{\mathrm{MSF_{fm}}}_{-,k}$ is that of a conventional Bogoliubov superfluid phase, here associated with the $U(1)$ broken gauge symmetry of the molecular condensate. The quadratic in k gapless spectrum is that of the ferromagnetic spin waves, where the two components of the spinor are canonically conjugate and, as a result, combine into a single low-frequency mode. The schematic plot of the excitations is shown in Fig. 8.

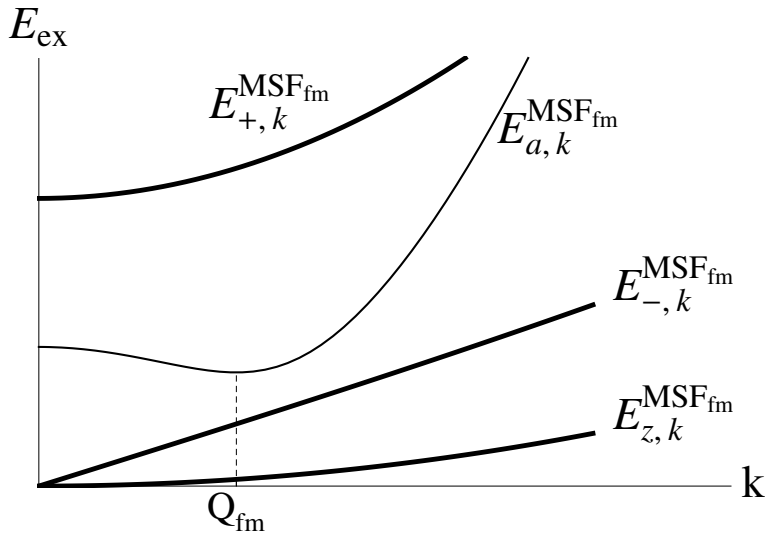

Figure 8: Schematic excitation spectrum for the $\mathrm{MSF_{fm}}$. The doubly degenerate atomic spectrum (thin curves) exhibits a minimum gap at nonzero k, a precursor of finite momentum atomic condensation. The molecular spectrum (thick curves) consists of a longitudinal gapless quadratic ferromagnetic spin-wave mode (lowest), a Bogoliubov sound mode, and a quadratic gapped mode.

Atomic molecular superfluid excitation: To obtain the spectrum inside the AMSF phases requires a solution of the fully general Hamiltonian, H_f. A complementary coherent-state path-integral approach is taken to obtain the modes and dispersions analytically. We analyze the low-energy fluctuations in the AMSF states using the coherent-state Lagrangian density, $\mathcal{L}[\psi_\sigma, \boldsymbol{\phi}] = \mathcal{L}_{\mathrm{MFT}}[\Psi_\sigma, \boldsymbol{\Phi}] + \delta\mathcal{L}$. To obtain $\delta\mathcal{L}$ we expand the atomic and molecular bosonic fields $\psi_\sigma, \boldsymbol{\phi}$ about their mean-field values (for clarity of notation in this section we choose to

use ρ instead of n of the previous sections, where $\rho_\sigma = n_a/2$, $\rho_m = n_m$, and $\rho_s = n$),

$$\psi_\sigma = \sqrt{\rho_\sigma} e^{i\theta_\sigma + i\boldsymbol{Q}_\sigma \cdot \boldsymbol{r}}, \tag{3.33a}$$

$$\boldsymbol{\phi} = \sqrt{\rho_m}\hat{\boldsymbol{\phi}} e^{i\varphi}, \tag{3.33b}$$

where $\boldsymbol{Q}_\sigma = \pm \boldsymbol{Q}$ for $\sigma = 1, 2$, respectively, $\rho_m = \rho_{m0} + \delta\rho_m$ and $\rho_\sigma = \rho_0 + \delta\rho_\sigma$ are the molecular and atomic densities, with the mean-field values $\rho_{m0} = |\boldsymbol{\Phi}|^2$ and $\rho_0 = |\Psi_\sigma|^2$. For the polar case, substituting these parametrizations of the atomic and molecular fields into the Lagrangian, we obtain $\delta\mathcal{L}$ that controls fluctuations in the AMSF phases for the polar case ($\boldsymbol{\phi} = \sqrt{\rho_m}\hat{\boldsymbol{n}} e^{i\varphi}$),

$$\begin{aligned}
\delta\mathcal{L}_{\rm p} &= i\delta\rho_+ \partial_\tau \theta_+ + \frac{\rho_0}{m}(\boldsymbol{\nabla}\theta_+)^2 + i\delta\rho_- \partial_\tau \theta_- + \frac{\rho_0}{m}(\boldsymbol{\nabla}\theta_- + \boldsymbol{Q})^2 + i\delta\rho_m \partial_\tau \varphi \\
&+ \frac{\rho_{m0}}{4m}(\boldsymbol{\nabla}\varphi)^2 + \frac{\rho_{m0}}{4m}(\boldsymbol{\nabla}\hat{\boldsymbol{n}})^2 - 2\alpha\rho_0\sqrt{\rho_{m0}}\hat{\boldsymbol{n}} \cdot (\boldsymbol{\nabla}\theta_- + \boldsymbol{Q})\cos(\varphi - 2\theta_+) \\
&+ \frac{1}{16m\rho_0}(\boldsymbol{\nabla}\rho_+)^2 + \frac{1}{16m\rho_0}(\boldsymbol{\nabla}\rho_-)^2 + \frac{1}{16m\rho_{m0}}(\boldsymbol{\nabla}\rho_m)^2 + \frac{\lambda}{4}\delta\rho_+^2 + \frac{\lambda}{4}\delta\rho_-^2 \\
&+ \frac{\lambda_{12}}{4}(\delta\rho_+^2 - \delta\rho_-^2) + g_{am}\delta\rho_+\delta\rho_m + \frac{g}{2}\delta\rho_m^2,
\end{aligned} \tag{3.34}$$

where $g \equiv g_1 + g_2$, $\lambda = \lambda_1 = \lambda_2$ for simplicity, and

$$\theta_\pm = \frac{1}{2}(\theta_1 \pm \theta_2), \tag{3.35a}$$

$$\delta\rho_\pm = \delta\rho_1 \pm \delta\rho_2, \tag{3.35b}$$

$$\mu = \frac{1}{2}(\mu_1 + \mu_2), \tag{3.35c}$$

$$h = \frac{1}{2}(\mu_1 - \mu_2), \tag{3.35d}$$

$$\boldsymbol{Q} = \alpha m\sqrt{\rho_{m0}}\hat{\boldsymbol{n}}_0. \tag{3.35e}$$

The above Lagrangian is expanded up to quadratic order in fluctuations, and neglect high order contributions. The Goldstone modes are characterized by dispersions:

$$\omega_{+p}(\boldsymbol{k}) = c_+ k, \tag{3.36a}$$

$$\omega_{-p}(\boldsymbol{k}) = \sqrt{(Bk_z^2 + Kk_\perp^4)/\chi_-}, \tag{3.36b}$$

with defined parameters

$$c_+ = \sqrt{\frac{2\rho_{s0}}{\chi_+ m}}, \tag{3.37a}$$

$$B = \frac{2\rho_0}{m}, \tag{3.37b}$$

$$K = \frac{1}{2m^3\alpha^2}. \tag{3.37c}$$

k_z refers to the direction of $\boldsymbol{Q}$. The linear $\omega_+(k)$ dispersion of the superfluid phase θ_+ is the expected Bogoliubov mode corresponding to the superfluid order. The anisotropic smecticlike dispersion of the "phonon" θ_- is a reflection of the uniaxial finite-momentum order in the $\mathrm{AMSF_p}$ state, akin to the FF superconductor.

For the ferromagnetic case, the analysis for the $\mathrm{AMSF_{fm}}$ phase is very similar, with only a single modification of the $\mathrm{MSF_{fm}}$ order parameter,

$$\begin{aligned}
\delta\mathcal{L}_{\mathrm{fm}} \approx\ & i(\delta\rho_+ + 2\delta\rho_m)\partial_\tau\theta_+ + \frac{\rho_{s0}}{m}(\boldsymbol{\nabla}\theta_+)^2 + i\delta\rho_-\partial_\tau\theta_- + \frac{\rho_0}{m}\left(\boldsymbol{\nabla}\theta_- - \frac{1}{\sqrt{2}}\alpha m\sqrt{\rho_{m0}}\delta\hat{\boldsymbol{n}}\right)^2 \\
+\ & i\rho_{m0}\delta\hat{\boldsymbol{n}}\cdot\partial_\tau\hat{\boldsymbol{m}} + \frac{\rho_{m0}}{8m}(\boldsymbol{\nabla}\hat{\boldsymbol{n}})^2 + \frac{\rho_{m0}}{8m}(\boldsymbol{\nabla}\hat{\boldsymbol{m}})^2 + \frac{1}{16m\rho_0}(\boldsymbol{\nabla}\rho_+)^2 + \frac{1}{16m\rho_0}(\boldsymbol{\nabla}\rho_-)^2 \\
+\ & \frac{1}{16m\rho_{m0}}(\boldsymbol{\nabla}\rho_m)^2 + \frac{\lambda}{4}\delta\rho_+^2 + \frac{\lambda}{4}\delta\rho_-^2 + \frac{\lambda_{12}}{4}(\delta\rho_+^2 - \delta\rho_-^2) + g_{am}\delta\rho_+\delta\rho_m + \frac{g_1}{2}\delta\rho_m^2,
\end{aligned} \tag{3.38a}$$

A straightforward diagonalization of the above Lagrangian leads to dispersions for three Goldstone modes inside the $\mathrm{AMSF_{fm}}$ state:

$$\omega^+_{fm}(\boldsymbol{k}) = c_+ k, \tag{3.39a}$$

$$\omega^-_{fm}(\boldsymbol{k}) = \sqrt{[Bk_z^2 + k^2(K_x k_x^2 + K_y k_y^2)]/\chi_-}, \tag{3.39b}$$

$$\omega^\gamma_{fm}(\boldsymbol{k}) = \sqrt{\frac{Jk^2[Bk_z^2 + k^2(K_x k_x^2 + K_y k_y^2)]}{J\chi_- k^2 + \kappa^2 k_y^2}}. \tag{3.39c}$$

with defined parameters,

$$\kappa = \frac{\sqrt{2\rho_{m0}}}{\alpha m}, \tag{3.40a}$$

$$K_x = \frac{1}{m^3\alpha^2} = K, \tag{3.40b}$$

$$K_y = \frac{1}{2m^3\alpha^2}, \tag{3.40c}$$

$$J = \frac{\rho_{m0}}{4m} = K_y Q^2. \tag{3.40d}$$

The anisotropic $\omega^{\gamma}_{fm}(\boldsymbol{k})$ dispersion corresponds to the ferromagnetic spin waves in the plane of atomic condensate phase fronts ("smectic layers") of the p-wave atomic-molecular condensate, $\mathrm{AMSF_{fm}}$, reducing to the dispersion of $\mathrm{MSF_{fm}}$ in Eq. (3.32) for a vanishing smectic order, with $B = 0$.

4.0 Superfluid Phases and Excitations in a Cold Gas of d-wave Interacting Bosonic Atoms and Molecules

Recently, d-wave scattering resonance was observed in more and more ultracold atomic gases [38, 39, 40, 41]. Particularly the observation of degenerate d-wave-interacting Bose gases with d-wave shape resonance [41] makes the hidden d-wave many-body correlation experimentally more accessible.

As we discussed in the previous section, unlike s-wave interaction, the closed channels of high-partial-wave Feshbach resonance carry finite momentum. It is predicted that finite-momentum superfluid emerges in a p-wave interacting Bose gas [42, 9, 43]. The closed channels of d-wave Feshbach resonance carry a total angular momentum of $2\hbar$, and hence the many-body form is proportional to the square of momentum k^2. Although d-wave electronic Fermi superconductor has been studied extensively in condensed matter physics, to the best of our knowledge, what possible many-body states the d-wave interacting atomic Bose gases should exhibit is a widely open question.

Inspired by recent experimental progress [40, 41], we analyze the zero-temperature mean-field ground state and Bogoliubov spectrum of a d-wave interacting Bose gas in this paper. A two-channel model is adopted for a mixture of two components interacting via d-wave interaction. Similar to the p-wave interacting Bose gas [42, 9, 43], the mean-field ground state typically shows three quantum phases: atomic superfluid (ASF), molecular superfluid (MSF) and atomic-molecular superfluid (AMSF). But unlike the p-wave case, the atomic superfluid does not carry finite momentum. The phase boundaries are analytically obtained. Furthermore, the Bogoliubov excitation spectrum is analyzed both numerically and analytically above the superfluid ground state with d-orbital aspects.

4.1 Model

Inspired by the experiments[40, 44], we will focus on a gas mixture of two distinguishable bosonic atoms (e.g., ^{85}Rb and ^{87}Rb). The two atomic fields are created by $\hat{\psi}^{\dagger}_{\sigma} = (\hat{\psi}^{\dagger}_{1}, \hat{\psi}^{\dagger}_{2})$ and interact through a d-wave FR associated with a tunable molecular bound state [9, 45]. According to the symmetry of this system, the angular momentum is a good quantum number and the related d-wave molecule (e.g., ^{85}Rb-^{87}Rb) field is created by $\hat{\phi}^{\dagger}_{m} = (\hat{\phi}^{\dagger}_{-2}, \hat{\phi}^{\dagger}_{-1}, \hat{\phi}^{\dagger}_{0}, \hat{\phi}^{\dagger}_{1}, \hat{\phi}^{\dagger}_{2})$, which corresponds to the five closed-channel molecule states (e.g., l_z=0, $\pm$1, $\pm$2). Apart from the d-wave interaction, we assume that the system is also subject to the background atom-atom, molecule-molecule and atom-molecule s-wave interactions. The Hamiltonian density for this system is written as (we take $\hbar$=1 throughout) [46],

$$\begin{aligned}\mathcal{H} = &\sum_{\sigma=1,2} \hat{\psi}^{\dagger}_{\sigma}(-\frac{\nabla^2}{2m} - \mu_{\sigma})\hat{\psi}_{\sigma} + \sum_{m=-2}^{2} [\hat{\phi}^{\dagger}_{m}(-\frac{\nabla^2}{4m} + z(-\frac{\nabla^2}{4m})^2 - \mu_M)\hat{\phi}_{m}. - \overline{g}(\hat{\phi}^{\dagger}_{m} y_m + h.c.)] \\ &+ \mathcal{H}_{bg},\end{aligned} \tag{4.1}$$

where the operator y_m and background interaction $\mathcal{H}_{bg}$ are respectively given by

$$y_m = \frac{1}{4} \sum_{a,b=x,y,z} C^{m}_{ab}[(\partial_a\hat{\psi}_1)(\partial_b\hat{\psi}_2) - (\partial_a\partial_b\hat{\psi}_1)\hat{\psi}_2 + (\partial_b\hat{\psi}_1)(\partial_a\hat{\psi}_2) - \hat{\psi}_1(\partial_a\partial_b\hat{\psi}_2)], \tag{4.2}$$

$$\mathcal{H}_{bg} = \frac{1}{2} \sum_{\sigma,\sigma'=1,2} \lambda_{\sigma\sigma'}|\hat{\psi}_{\sigma}|^2|\hat{\psi}_{\sigma'}|^2 + \sum_{m,n=-2}^{2} \frac{g_0}{2}(\hat{\phi}^{\dagger}_{m}\hat{\phi}_{m})(\hat{\phi}^{\dagger}_{n}\hat{\phi}_{n}) + \sum_{m=-2}^{2} g_{\mathrm{AM}}(|\hat{\psi}_1|^2 + |\hat{\psi}_2|^2)\hat{\phi}^{\dagger}_{m}\hat{\phi}_{m}. \tag{4.3}$$

Here μ_1 and μ_2 are the chemical potentials of the atoms and μ_M is that for the molecule. The detuning between atomic and molecular channels is given by $\nu = \mu_1 + \mu_2 - \mu_M$. $\overline{g}$ characterizes the d-wave interaction strength. C^{m}_{ab} is the Clebsch-Gordan coefficient [45], satisfying $\sum_{a,b} C^{m}_{ab}k_a k_b/k^2 = \sqrt{4\pi}Y^{m}_{2}(\hat{k})$, where $Y^{m}_{2}(\hat{k})$ is the spherical harmonics of degree 2 arising from the d-wave components of two-body wave function. For simplicity, we have taken the two atomic masses m to be identical, which is a good approximation for the mixtures

of isotopes like ^{85}Rb and ^{87}Rb. Thus, the molecules have the mass of $2m$. The z term in Eq. (4.1) is formally introduced for the normalization of the d-wave interaction [46], but it actually does not affects the mean-field dynamics. In the background interaction $\mathcal{H}_{bg}$, the $\lambda_{\sigma\sigma'}$ term characterizes the atom-atom interactions given by different species respectively, the g_{AM} term describes the atom-molecule interaction, and the g_0 term describes the molecule-molecule interaction. We restrict ourselves in the homogeneous case for simplicity and clarity by the local density approximation widely applied to the study of trapped gaeses in the experiment. It is proven to be a good approximation for a slowly varying trap potential with a large number of atoms in the experiment.

4.2 Mean-field Theory

We will obtain the Landau free energy by applying mean-field theory to our model and minimize it to establish the phase diagram and analyze the phase transition. This method is equivalent to solving Gross-Pitaevskii equation. Replacing the atomic and molecular field operators with their relative classical order parameters Ψ_σ, Φ_m, we obtain the Landau free energy function $F[\Psi_\sigma, \Phi_m] = \langle H \rangle$.

We decompose our mean-field parameters to characterize the states of the system. For the atomic condensates Ψ_1 and Ψ_2, let us use Fourier transform and make these fields complex periodic functions characterized by momenta $\mathbf{Q}_n$,

$$\Psi_\sigma = \sum_{\mathbf{Q}_n} \Psi_{\sigma,\mathbf{Q}_n} e^{i\mathbf{Q}_n\cdot\mathbf{r}}. \tag{4.4}$$

It is generally expected that the assumption of having a single component, $\mathbf{Q}_n = \mathbf{Q}$ is sufficient to capture the qualitative picture of the ground state [47]. Unlike p-wave case [9], the d-wave interaction is proportional to the square of momentum and thus can not give rise to finite-momentum molecular condensates, since the minimum of the total energy still keeps at the zero momentum of molecules. In order to make the momentum conservation, the ground state should fall into two universal classes: FF (Fulde-Ferrell)-like [48] form $\Psi_\sigma^{FF} = \Psi_{\sigma,\mathbf{Q}_\sigma} e^{i\mathbf{Q}_\sigma\cdot\mathbf{r}}$ or the LO (Larkin-Ovchinnikov)-like [49] form $\Psi_\sigma^{LO} = \Psi_{\sigma,\mathbf{Q}} e^{i\mathbf{Q}\cdot\mathbf{r}} + \Psi_{\sigma,-\mathbf{Q}} e^{-i\mathbf{Q}\cdot\mathbf{r}}$

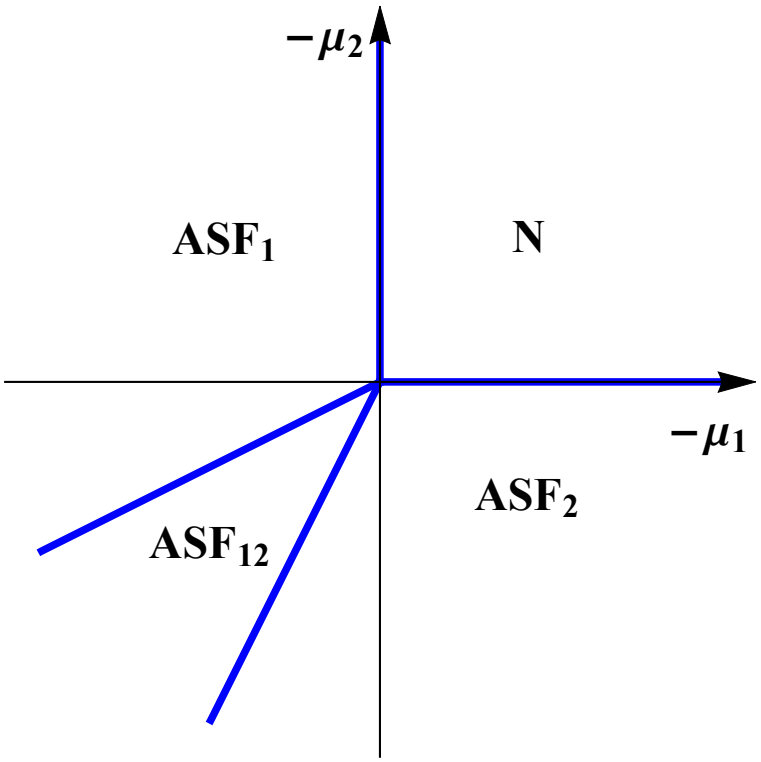

Figure 9: Mean-field phase diagram of a d-wave resonant two-component Bose gas for large positive detuning and $4\lambda_{11}\lambda_{22} - (\lambda_{12} + \lambda_{21})^2 > 0$. The atomic channels have lower energy. ASF_1 and ASF_2 refer to single atom species superfluid state, and ASF_{12} refers to double atom species superfluid state.

where $\Psi_{\sigma,\mathbf{Q}} = \Psi_{\sigma,-\mathbf{Q}}$. Based on the analysis of total energy (see Supplementary B), the order parameters favor the simplest but non-trivial FF-like form with a single ordering wavevector $\mathbf{Q}_1 = -\mathbf{Q}_2 = \mathbf{Q}$, described by

$$\begin{aligned} \Psi_1 &= \Psi_{1,\mathbf{Q}} e^{i\mathbf{Q}\cdot\mathbf{r}}, \\ \Psi_2 &= \Psi_{2,-\mathbf{Q}} e^{-i\mathbf{Q}\cdot\mathbf{r}}. \end{aligned} \tag{4.5}$$

Atomic superfluid phase: For large positive detuning $\nu > 0$, the atomic channels have lower energy and the ground state is a molecule vacuum. The free energy is minimized by

phase	chemical potentials	Ψ_1	Ψ_2
N	$\mu_1<0,\mu_2<0$	0	0
ASF_1	$\mu_1>0,\mu_2<\frac{\lambda_{12}+\lambda_{21}}{2\lambda_{11}}\mu_1$	$\sqrt{\frac{\mu_1}{\lambda_{11}}}$	0
ASF_2	$\mu_1<\frac{\lambda_{12}+\lambda_{21}}{2\lambda_{22}}\mu_2,\mu_2>0$	0	$\sqrt{\frac{\mu_2}{\lambda_{22}}}$
ASF_{12}	$\mu_1>\frac{\lambda_{12}+\lambda_{21}}{2\lambda_{22}}\mu_2,\mu_2>\frac{\lambda_{12}+\lambda_{21}}{2\lambda_{11}}\mu_1$	$\sqrt{\frac{4\lambda_{22}\mu_1-2(\lambda_{12}+\lambda_{21})\mu_2}{4\lambda_{11}\lambda_{22}-(\lambda_{12}+\lambda_{21})^2}}$	$\sqrt{\frac{4\lambda_{11}\mu_2-2(\lambda_{12}+\lambda_{21})\mu_1}{4\lambda_{11}\lambda_{22}-(\lambda_{12}+\lambda_{21})^2}}$

Table 1: Sub-phases of the ASF phase. i) When μ_1 and μ_2 are negative, both atomic species are in the normal (N) phase. ii) When $\mu_1>0,\mu_2<\frac{\lambda_{12}+\lambda_{21}}{2\lambda_{11}}\mu_1$, the atom 1 forms condensate. iii) When $\mu_1<\frac{\lambda_{12}+\lambda_{21}}{2\lambda_{22}}\mu_2,\mu_2>0$, the atom 2 forms condensate. iv) When $\mu_1>\frac{\lambda_{12}+\lambda_{21}}{2\lambda_{22}}\mu_2,\mu_2>\frac{\lambda_{12}+\lambda_{21}}{2\lambda_{11}}\mu_1$, both atom species form condensates.

spatially uniform atomic order parameters [50] and leads to the free energy density with the form

$$f_A = -\sum_{\sigma=1,2}\mu_\sigma|\Psi_\sigma|^2+\sum_{\sigma,\sigma'=1,2}\frac{\lambda_{\sigma,\sigma'}}{2}|\Psi_\sigma|^2|\Psi_{\sigma'}|^2\,. \tag{4.6}$$

For $4\lambda_{11}\lambda_{22}-(\lambda_{12}+\lambda_{21})^2>0$, the minimization of f_A leads to different superfluid phases as μ_1 and μ_2 change, which are listed in Table 1 (see Fig. 9). Otherwise, for $4\lambda_{11}\lambda_{22}-(\lambda_{12}+\lambda_{21})^2<0$, the ASF_{12} phase tends to be unstable, there will be a direct first-order phase transition from ASF_1 to ASF_2, and its phase boundary is determined to be $\mu_2=\sqrt{\frac{\lambda_{22}}{\lambda_{11}}}\mu_1$ (see Fig. 10).

Molecular superfluid phase: In the MSF phase, we have large negative detuning $\nu<0$, that is, $-\nu\gg|\mu_{1,2}|$. The molecular channels have lower energy and the ground state is an atom vacuum. The free energy density f_M is given as

$$f_M = \sum_{m=-2}^{2}-\mu_M|\Phi_m|^2+\sum_{m,n=-2}^{2}\frac{g_0}{2}(\Phi_m^*\Phi_m)(\Phi_n^*\Phi_n). \tag{4.7}$$

The molecular condensate density is obtained by minimizing the free energy,

$$\Phi=\sqrt{\frac{\mu_M}{g_0}}D(0,0,1,0,0)^T, \tag{4.8}$$

where D is an $SU(5)$ matrix satisfying $D * D^{\dagger} = 1$. The ground state implies a broken symmetry group $SU(5)$.

Atomic-molecular superfluid phase: For the intermediate detuning, both the atomic and molecular modes are gapless. To understand the phase boundaries and the behavior of order parameters, it is convenient to approach the AMSF phase from MSF phase [9]. For simplicity, we specialize in a balanced mixture by $\mu_1 = \mu_2 = \mu$. Applying mean-field assumption, we obtain the free energy density $f_{AM} = F[\Psi_\sigma, \Phi_m]/V = f_Q + f_M$, where f_Q describes the Q-dependent fragment in the free energy density f_{AM},

$$f_Q = \sum_{\sigma=1,2} \varepsilon_Q |\Psi_{\sigma,\mathbf{Q}_\sigma}|^2 - (\Delta^*_{\mathbf{Q}} \Psi_{1,\mathbf{Q}} \Psi_{2,-\mathbf{Q}} + c.c.) + \sum_{\sigma,\sigma'=1,2} \frac{\lambda_{\sigma,\sigma'}}{2} |\Psi_{\sigma,\mathbf{Q}_\sigma}|^2 |\Psi_{\sigma',\mathbf{Q}_{\sigma'}}|^2, \tag{4.9}$$

$$f_M = -\sum_{m=-2}^{2} \mu_M \Phi^*_m \Phi_m + \sum_{m,n=-2}^{2} \frac{g_0}{2} (\Phi^*_m \Phi_m)(\Phi^*_n \Phi_n). \tag{4.10}$$

In the above equations, the atomic order parameter ansatz Eqs. (4.5) is used to simplify f_Q. $\varepsilon_Q = (\frac{Q^2}{2m} - \mu + \sum_{m=-2}^{2} g_{\rm AM} |\Phi_m|^2)$, $\Delta_{\mathbf{Q}} = \sum_{m=-2}^{2} \overline{g} \sqrt{4\pi} Q^2 Y_2^m(\hat{\mathbf{Q}}) \Phi_m$, $\mathbf{Q}_1 = \mathbf{Q}$ and $\mathbf{Q}_2 = -\mathbf{Q}$. When we approach the ASMF phase from the MSF phase, the atomic condensate fractions are considered to be small and perturbative. Thus, the quadratic order terms are enough to characterize the free energy density f_Q. Besides, when the atom condensate is emergent in the AMSF phase, they prefer to stay at a lower energy level. The condensate mean-field ground states are obtained by minimizing the free energy f_{AM},

$$Q = 0, \tag{4.11}$$

$$\Phi \ = \sqrt{\tfrac{g_{\rm AM}\mu - \lambda\mu_M}{g_{\rm AM}^2 - g_0\lambda}} D(0,0,1,0,0)^T, \tag{4.12}$$

$$|\Psi_{1,2}| = \sqrt{\frac{g_0\mu - g_{\rm AM}\mu_M}{2\lambda g_0 - 2g_{\rm AM}^2}}, \tag{4.13}$$

where D is an $SU(5)$ rotation matrix. Similar to the analysis in the MSF context, the broken symmetry group is $SU(5)$. Worth noting, a zero momentum solution is needed to minimize

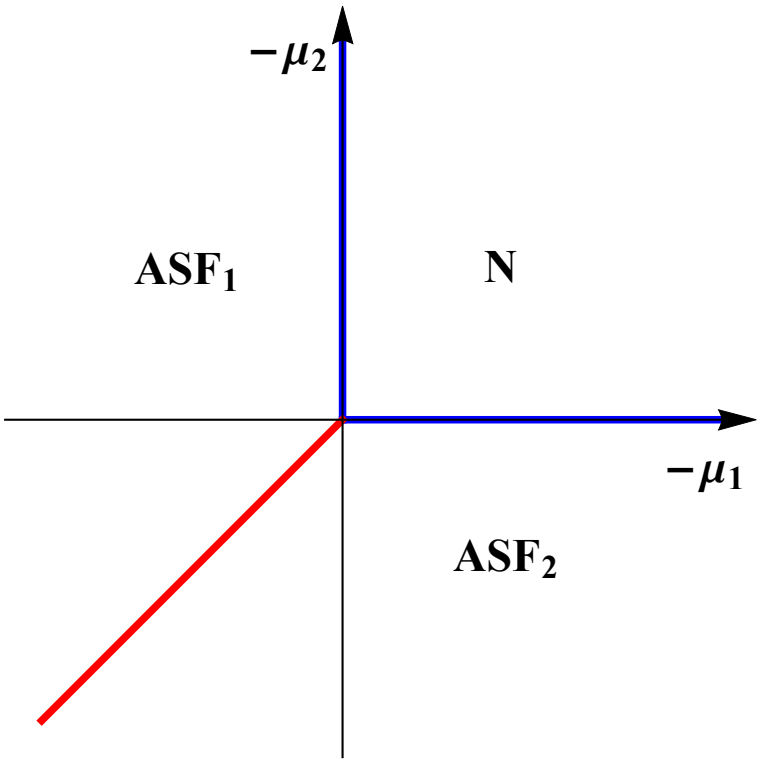

Figure 10: Mean-field phase diagram of a d-wave resonant two-component Bose gas for large positive detuning and $4\lambda_{11}\lambda_{22} - (\lambda_{12} + \lambda_{21})^2 < 0$. A valid phase of significant condensate fraction in both atom fields is not found in mean-field calculation. The phases ASF_1 and ASF_2 are separated by a first-order transition boundary.

the free energy, which is different from the finite momentum case in p-wave interaction gases [9]. The condensate densities are

$$n_M = \frac{(2\lambda - g_{\rm AM})\mu - \lambda\nu}{\lambda g_0 - g_{\rm AM}^2}, \tag{4.14}$$

$$n_A = \frac{(g_0 - 2g_{\rm AM})\mu + g_{\rm AM}\nu}{\lambda g_0 - g_{\rm AM}^2}. \tag{4.15}$$

By setting $n_A = 0$ and $n_M = 0$ respectively, we obtain the two phase boundaries to separate the three phases, molecular superfluid (MSF), atomic-molecular superfluid (AMSF) and

atomic superfluid (ASF). The relation between condensate densities and detuning is depicted in Fig. 11,

$$\nu_1^d = (2 - \frac{g_0}{g_{\rm AM}})\mu, \tag{4.16}$$

$$\nu_2^d = (2 - \frac{g_{\rm AM}}{\lambda})\mu. \tag{4.17}$$

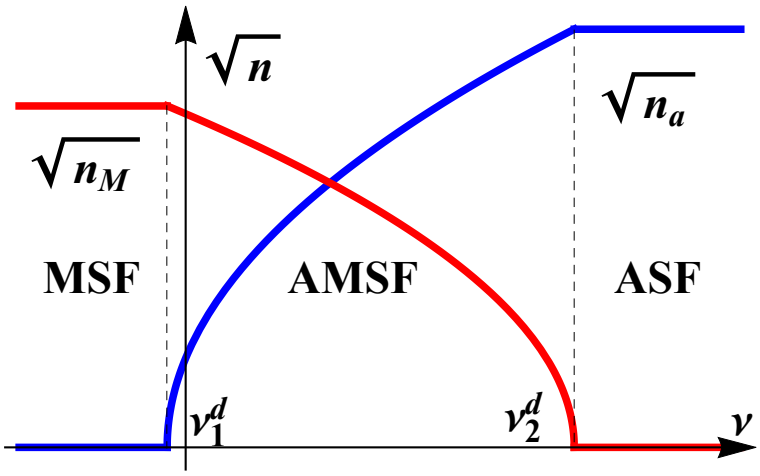

Figure 11: Atomic and molecular condensate density versus the FR detuning ν. Red curves are for molecule condensate density, blue curves are for atom condensate density, i) MSF for $\nu < \nu_1^d$ ii) AMSF for $\nu_1^d < \nu < \nu_2^d$ iii) ASF for $\nu > \nu_2^d$.

4.3 Low Energy Excitations

In this section, we will focus on the low energy excitations for d-wave FR to cross-examine the consistency of mean-field results. To begin with, we expand the field operators in the ASF, MSF and AMSF phases around their mean-field condensate values [43, 9], $\hat{\psi}_\sigma = \Psi_\sigma + \delta\hat{\psi}_\sigma$ and $\hat{\phi}_m = \Phi_m + \delta\hat{\phi}_m$. With these perturbation field representations, the

Hamiltonian (4.1) is expanded up to the second order in the momentum space with creation and annihilation operators $\hat{a}_{\sigma,\mathbf{k}}$ and $\hat{b}_{m,\mathbf{k}}$,

$$\begin{aligned} H_f = \quad & \sum_{\mathbf{k}}\{\sum_{\sigma=1,2}(\frac{1}{2}\varepsilon_{\sigma,\mathbf{k}+\mathbf{Q}_\sigma}\hat{a}^\dagger_{\sigma,\mathbf{k}+\mathbf{Q}_\sigma}\hat{a}_{\sigma,\mathbf{k}+\mathbf{Q}_\sigma} + \tilde{\lambda}_\sigma\hat{a}_{\sigma,-\mathbf{k}+\mathbf{Q}_\sigma}\hat{a}_{\sigma,\mathbf{k}+\mathbf{Q}_\sigma}) + t_1\hat{a}^\dagger_{1,\mathbf{k}+\mathbf{Q}}\hat{a}_{2,\mathbf{k}-\mathbf{Q}} \\ + \quad & t_{2,\mathbf{k}+\mathbf{Q}}\hat{a}_{1,\mathbf{k}+\mathbf{Q}}\hat{a}_{2,-\mathbf{k}-\mathbf{Q}} + \sum_m(\frac{1}{2}\omega_{m,k}\hat{b}^\dagger_{m,k}\hat{b}_{m,k} + \delta_m\hat{b}_{m,-k}\hat{b}_{m,k}) \\ + \quad & \frac{1}{2}\sum_{m\neq n}(g_{m,n}\hat{b}^\dagger_{n,k}\hat{b}_{m,k} + \gamma_{m,n}\hat{b}_{m,-k}\hat{b}_{n,k}) + \sum_{\sigma,m}\beta_{1,m,\sigma}\hat{a}^\dagger_{\sigma,\mathbf{k}+\mathbf{Q}_\sigma}\hat{b}_{m,k} + \sum_{\sigma,m}\beta_{2,m,\sigma}\hat{a}^\dagger_{\sigma,\mathbf{k}+\mathbf{Q}_\sigma}\hat{b}^\dagger_{m,-k} \\ + \quad & \sum_{\sigma,m}\beta_{3,m,\sigma}\hat{a}_{\sigma,-\mathbf{k}+\mathbf{Q}_\sigma}\hat{b}_{m,k} + \sum_{\sigma,m}\beta_{4,m,\sigma}\hat{a}_{\sigma,-\mathbf{k}+\mathbf{Q}_\sigma}\hat{b}^\dagger_{m,-k} - \sum_{\sigma,m}\alpha_{m,\bar{\sigma},\mathbf{k}}\hat{b}^\dagger_{m,k}\hat{a}_{\sigma,\mathbf{k}+\mathbf{Q}_\sigma} + h.c.\}. \end{aligned} \tag{4.18}$$

The parameters are defined below,

$$\varepsilon_{\sigma,\mathbf{k}} = \epsilon_{\mathbf{k}} - \mu_\sigma + 2\lambda_{\sigma,\sigma}|\Psi_\sigma|^2 + \frac{1}{2}(\lambda_{12}+\lambda_{21})|\Psi_{\bar{\sigma}}|^2 + g_{\mathrm{AM}}\sum_m \Phi^*_m\Phi_m, \tag{4.19}$$

$$\omega_{m,k} = \frac{1}{2}\epsilon_{\mathbf{k}} + z(\frac{1}{2}\epsilon_{\mathbf{k}})^2 - \mu_M + g_0\sum_n \Phi^*_n\Phi_n + g_0\Phi^*_m\Phi_m + g_{\mathrm{AM}}(|\Psi_1|^2 + |\Psi_2|^2), \tag{4.20}$$

$$\tilde{\lambda}_\sigma = \frac{1}{2}\lambda_{\sigma,\sigma}\Psi^{*2}_\sigma, \tag{4.21}$$

$$t_1 = \frac{1}{2}(\lambda_{12}+\lambda_{21})\Psi_1\Psi^*_2, \tag{4.22}$$

$$t_{2,\mathbf{k}} = \frac{1}{2}(\lambda_{12}+\lambda_{21})\Psi^*_1\Psi^*_2 - \overline{g}\sqrt{4\pi}k^2\sum_m \Phi^*_m Y^m_2(\hat{\mathbf{k}}), \tag{4.23}$$

$$\delta_m = \frac{1}{2}g_0\Phi^*_m\Phi^*_m, \tag{4.24}$$

$$g_{m,n} = g_0\Phi^*_m\Phi_n, \tag{4.25}$$

$$\gamma_{m,n} = g_0\Phi^*_m\Phi^*_n, \tag{4.26}$$

$$\beta_{1,m,\sigma} = g_{\mathrm{AM}}\Psi_\sigma\Phi^*_m, \tag{4.27}$$

$$\beta_{2,m,\sigma} = g_{\mathrm{AM}}\Psi_\sigma\Phi_m, \tag{4.28}$$

$$\beta_{3,m,\sigma} = g_{\mathrm{AM}}\Psi^*_\sigma\Phi^*_m, \tag{4.29}$$

$$\beta_{4,m,\sigma} = g_{\mathrm{AM}}\Psi^*_\sigma\Phi_m, \tag{4.30}$$

$$\alpha_{m,\sigma,\mathbf{k}} = \overline{g}\sqrt{4\pi}\Psi_{\sigma,\mathbf{Q}_\sigma}(\mathbf{Q}_\sigma - \frac{\mathbf{k}}{2})^2 Y_2^m(\widehat{\mathbf{k} - 2\mathbf{Q}_\sigma}), \tag{4.31}$$

where $\epsilon_k = \frac{k^2}{2m}, \overline{1} = 2$ and $\overline{2} = 1$. The Hamiltonian is diagonalized up to the order of k^2 theoretically, and an exact diagonalization is used to testify our analysis in the meanwhile.

Atomic superfluid excitation: In the ASF phase, it has been found that the molecular modes are gapped in the previous section. The relative mean-field $\Phi_m = 0$, and the atoms are condensed at zero momentum $\mathbf{Q} = 0$. To find out the atomic modes, we need to integrate the molecular modes out (see Supplementary C.1). In the low energy regime, when $k \to 0$, we calculate the dispersion up to k^2 order. The atomic and molecular modes are given by

$$E^A_{1,k} = \sqrt{\frac{k^2}{2m}(\frac{k^2}{2m} + 2\lambda n_A)}, \tag{4.32}$$

$$E^A_{2,k} = \sqrt{\frac{(2\lambda - \lambda_{12} - \lambda_{21})n_A}{2m}}k, \tag{4.33}$$

$$E^M_{-2,-1,0,1,2,k} = \frac{k^2}{4m} + \nu - 2\lambda n_A + g_{\mathrm{AM}}n_A, \tag{4.34}$$

where n_A is the atom condensate density in the mean-field level, $n_A = |\Psi_1|^2 + |\Psi_2|^2$. Obviously, the atomic modes are gapless excitations in the superfluid states. The molecular modes have energy gap $\nu - 2\lambda n_A + g_{\mathrm{AM}}n_A$. When it vanishes, we have the transition from ASF phase to AMSF phase at the detuning value

$$\nu = 2\lambda n_A - g_{\mathrm{AM}}n_A, \tag{4.35}$$

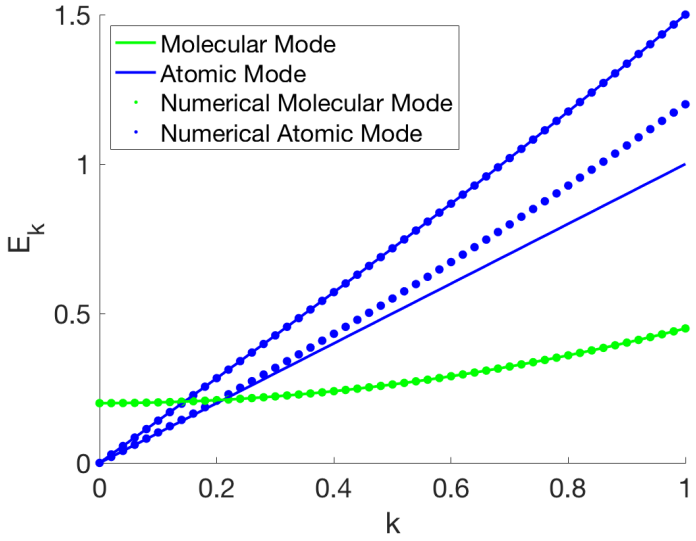

Figure 12: ASF phase excitation spectrum. Here we use parameters $\{m = 1, \mu = 1, \nu = 3.2, \lambda_{11} = \lambda_{22} = 3, \lambda_{12} = \lambda_{21} = 1\}$. The unit is arbitrary. All the molecular modes are gapped, but the atomic modes are gapless. The five molecule modes are degenerate. The numerical results and theoretical results fit well in small k regime.

which is consistent with Eq. (4.17)($n_A = \mu/\lambda$). Fig. 12 shows the theoretical results and numerical results. They fit well in the small k region.

Molecular superfluid excitation: In the MSF phase, the atomic modes are gapped and their mean-fields $\Psi_1 = \Psi_2 = 0$. The vanishing of atomic mean-fields results in $\alpha_{m,\sigma,\mathbf{k}} = 0$, which means the atomic Hamiltonian and molecular Hamiltonian are separable (see Supplementary C.2). Referring to the mean-field ground state (4.8), we choose the simplest case $D = 1$ to explore its low energy excitation, and it leads to $\Phi_{-2,-1,1,2} = 0$, $\Phi_0 = \sqrt{n_M}$. The respective atomic dispersions are degenerate,

$$E_k^A = \sqrt{\varepsilon_{\mathbf{k}}^2 - 4\pi\overline{g}^2\mathbf{k}^4 \sum_{m,n} \Phi_m Y_2^m(\widehat{\mathbf{k}})\Phi_n^* Y_2^n(\widehat{\mathbf{k}})}, \tag{4.36}$$

$$E_{0,k}^M = \sqrt{\frac{g_0 n_M}{2m}}k, \tag{4.37}$$

$$E^M_{n=\pm1,\pm2,k} = \frac{k^2}{4m}, \tag{4.38}$$

The five molecular modes are all gapless, which proves that they are in superfluid state. For the MSF phase, $\mu = \frac{1}{2}(\mu_M + \nu) < \frac{1}{2}(\mu_M + \nu_1^d)$, from which we can obtain $-\mu + g_{\rm AM} n_M > 0$. So in Eq. (4.36) $k = 0$ gives us the energy gap,

$$\Delta E^A_k = -\mu + g_{\rm AM} n_M, \tag{4.39}$$

By setting $\Delta E^A_k = 0$, the atomic modes become gapless and the atomic condensates are emergent. Applying $\nu = 2\mu - \mu_M$ and $\mu_M = g_0 n_M$(see Eq. (4.8)), we obtain the transition from the MSF to AMSF phase at the detuning value,

$$\nu = (2 - \frac{g_0}{g_{\rm AM}})\mu, \tag{4.40}$$

which is consistent with Eq. (4.16). Fig. 13 shows the consistency between the theoretical results and numerical results.

Atomic-molecular superfluid excitation: For the intermediate phase, both atomic and molecular condensates exist. Hence, they define a complicated coupled Hamiltonian (see Supplementary C.3). The molecular and atomic condensate mean-field solutions are given as

$$\Phi = \sqrt{\frac{g_{\rm AM}\mu - \lambda\mu_M}{g^2_{\rm AM} - g_0\lambda}} D(0,0,1,0,0)^T, \tag{4.41}$$

$$\Psi_{1,2} = \sqrt{\frac{g_0\mu - g_{\rm AM}\mu_M}{2\lambda g_0 - 2g^2_{\rm AM}}}. \tag{4.42}$$

Similar to what we have achieved in the MSF phase, we choose the simplest case to compute the spectrums, $D = 1$. Diagonalizing this Hamiltonian leads to the spectrums up to the order of k,

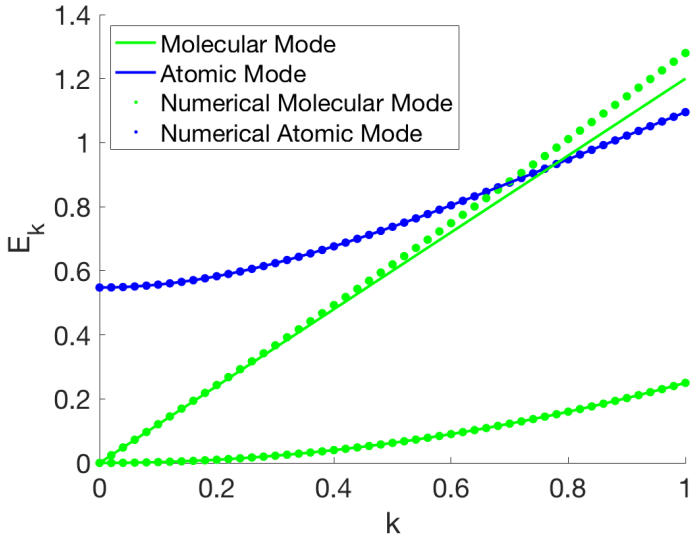

Figure 13: MSF phase excitation spectrum. The parameters used for MSF phase are $\{m = 1, \mu = 0, \nu = -1.44, g_0 = 1\}$. The atomic modes are gapped and degenerate. All the molecular modes are gapless, $m = \pm 1, \pm 2$ are degenerate on the lower green line, $m = 0$ is on the upper green line.

$$E^A_{1,k} = \sqrt{\frac{\lambda n_A}{m}} k, \tag{4.43}$$

$$E^A_{2,k} = \sqrt{(2\lambda - \lambda_{12} - \lambda_{21}) n_A (\frac{1}{2m} - \sqrt{5 n_M} \bar{g})} k, \tag{4.44}$$

$$E^M_{0,k} = \sqrt{\frac{(g_0 + \frac{g^2_{\mathrm{AM}}}{\lambda}) n_M}{2m}} k, \tag{4.45}$$

$$E^M_{n=\pm 1,\pm 2,k} = \frac{k^2}{4m}, \tag{4.46}$$

Fig. 14 shows the consistency between the theoretical results and numerical results.

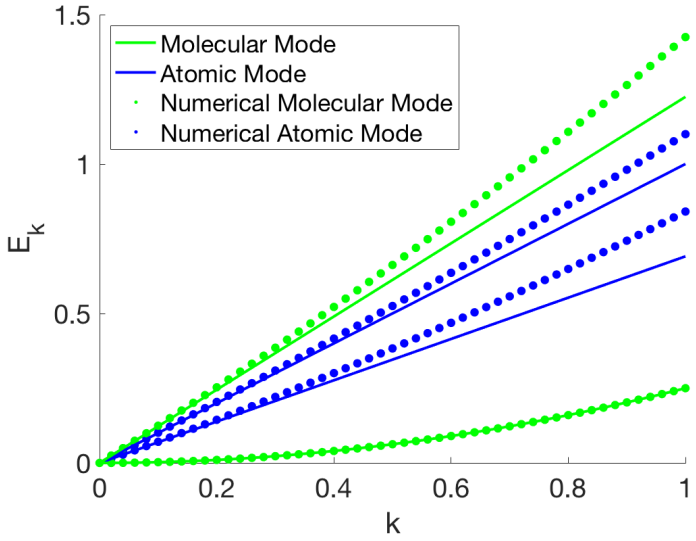

Figure 14: AMSF phase excitation spectrum. The parameters here are $\{m = 1, \mu = 0, \nu = -1, \lambda_{11} = \lambda_{22} = 1.5, \lambda_{12} = \lambda_{21} = 0.5, g_0 = 2, g_{AM} = -1, \overline{g} = 0.01\}$. The atomic modes are gapless on the two blue lines. The molecular modes are also gapless: $m = \pm 1, \pm 2$ are degenerate on the lower green line; $m = 0$ is on the upper green line.

4.4 Atom Loss Effect

In general, atom loss is inevitable near a Feshbach resonance. In this case, the free energy becomes complex and the ground states are no longer stable. For simplicity, let us qualitatively estimate the effect of atom loss by introducing imaginary parts into the chemical potentials $\mu_{1,2,M}$. Nevertheless, as a criteria, different quantum phases may be straightforwardly obtained from Tab. 1 by replacing the chemical potentials with their real parts, if we determine the ground states according to the real parts of the free energies in Eqs. (4.6,4.8,4.9,4.10). The imaginary part of the free energies determines the damping rate of the corresponding ground states. When the relaxation times (to the equilibrium states) are far shorter than the life time of the atomic gas due to the atom loss, the ground states predicted here are still observable. The qualitative properties of low-energy excitation spectra

(such as the numbers of gapless modes) are also expected to be unchanged by introducing the atom loss when the continuous symmetries are not broken. It is hard to quantitatively estimate the effect of atom loss at this stage since the experiment lacks necessary data.

5.0 Spontaneous Formation of Polar Superfluid Droplets in a p-wave Interacting Bose Gas

Quantum fluctuation is one of the most intrinsic properties of quantum mechanics, which is responsible for many fascinating physical phenomena, such as Casimir effect and abundant quantum phase transitions. Recently, Petrov showed that quantum fluctuation reflected by Lee-Huang-Yang (LHY) correction can prevent a mean-field-unstable Bose gas from collapsing [51]. The competition between the mean-field attraction and LHY repulsion stabilizes the Bose gas into a self-bound liquidlike droplet state. Subsequently, several experimental groups reported this novel quantum state with the prediction of Petrov [52, 53, 54]. In order to protrude the action of LHY correction, which is typically small in the dilute limit, Petrov suggested to subtly balance the inter- and intra-species interactions at the mean-field level. Owing to its unique formation mechanism, the self-bound state shows many interesting features, such as the quantum droplet is self-trapped and evaporated without external potential [51, 55].

The properties of quantum droplet are linked to the properties of interaction between particles. It is natural to ask if quantum droplet can be stabilized with other types of interaction and what their properties might be. It was also found that quantum droplets can be stabilized in a dipolar Bose gas benefiting from the competition between the dipolar interaction and s-wave contact interaction [56, 57, 58, 59]. The quantum droplets in a dipolar Bose gas are anisotropic and form a regular array, as a consequence of the dipolar interaction is anisotropic and long-ranged. Moreover, it is also predicted quantum droplets can be stabilized with the assistance of three-body interaction [60, 61] and spin-orbit coupling [62].

Here we study the beyond-mean-field ground state of a p-wave interacting Bose gas, and predict the existence of finite-momentum anisotropic self-stabilized quantum droplet. At the mean-field level, this p-wave interacting Bose gas typically has three ground-state phases: atomic superfluid (ASF) phase with only the atomic condensate, atomic-molecular superfluid (AMSF) phase with both atomic and molecular condensates, and molecular superfluid (MSF) phase with only the molecular condensate. We find AMSF phase is unstable and tends to

symmetry	$\hat{\psi}_1(\mathbf{r})$	$\hat{\psi}_2(\mathbf{r})$	$\hat{\phi}_{x,y,z}(\mathbf{r})$	$\boldsymbol{\nabla}$
$U_N(1)$	$e^{i\theta}\hat{\psi}_1$	$e^{i\theta}\hat{\psi}_2$	$e^{2i\theta}\hat{\phi}_{x,y,z}$	–
$[SU(2)/U_y(1)]$	$e^{i\theta_x\sigma_x+i\theta_z\sigma_z}(\hat{\psi}_1,\hat{\psi}_2)^T$		–	–
$SO(3)$	–	–	$e^{i\sum_{i=x,y,z}\overline{\theta}_i\lambda_i}\hat{\phi}$	$e^{i\sum_{i=x,y,z}\overline{\theta}_i\lambda_i}\boldsymbol{\nabla}$
Tr	$\hat{\psi}_1(\mathbf{r}+\mathbf{r}')$	$\hat{\psi}_2(\mathbf{r}+\mathbf{r}')$	$\hat{\phi}_{x,y,z}(\mathbf{r}+\mathbf{r}')$	–
$\mathcal{T}$	$\sum_{p_1} e^{-i\mathbf{p}_1\cdot\mathbf{r}}\hat{a}_{1,-\mathbf{p}_1}$	$\sum_{p_2} e^{-i\mathbf{p}_2\cdot\mathbf{r}}\hat{a}_{2,-\mathbf{p}_2}$	$e^{-i(\mathbf{p}_1+\mathbf{p}_2)\cdot\mathbf{r}}\hat{b}_{i,-\mathbf{p}_1-\mathbf{p}_2}$	–

Table 2: Symmetry transformation. $U_N(1)$: $\theta \in [0, 2\pi)$ is an arbitrary angle. This symmetry corresponds to the total number conservation. $[SU(2)/U_y(1)]$ with spin rotation symmetry $U_y(1)$ generated by σ_y: θ_x and θ_z are arbitrary angles. Here $\sigma_{x,y,z}$ are the Pauli matrices. $SO(3)$: $\lambda_{x,y,z}$ are defined in Eq. (5.2) and $\overline{\theta}_{x,y,z}$ are arbitrary rotation angles. Tr: $\mathbf{r}'$ is an arbitrary displacement vector in a 3D spatial coordinate. $\mathcal{T}$ time-reversal: We use momentum representation to expand $\hat{\psi}_1$ and $\hat{\psi}_2$ fields. Due to momentum conservation, the momentum of the molecule fields is restricted to $\mathbf{p}_1 + \mathbf{p}_2$.

collapse. Unlike pure s-wave interaction [63], we find the sign of the LHY correction of p-wave interaction may be different from that of the mean-field term when varying particle densities. A balance between the mean-field part and LHY correction exists for certain particle density, which gives rise to a self-stabilized (-bound) state without external potential. It is shown the self-stabilized state even survives in the dilute limit estimated with scattering volume. In addition to the U(1) global phase symmetry, the rotation, translation and time-reversal symmetries are found to be spontaneously broken by the presence of finite momentum of the order parameters. The result ground state is predicted to be an anisotropic quantum droplet with finite momentum for a system with finite particle number.

5.1 Model

Inspired by the experimental observations of p-wave Feshbach resonance in the mixture of ^{85}Rb and ^{87}Rb atoms [64, 65], we consider a mixture of two distinguishable species of bosonic atoms respectively created by $\hat{\psi}_1^\dagger(\boldsymbol{r})$ and $\hat{\psi}_2^\dagger(\boldsymbol{r})$ with interspecies p-wave interaction. The p-wave interaction arises from a p-wave Feshbach resonance by coupling with three closed molecular channels denoted by $l_z = -1, 0, 1$. Here $l_z\hbar$ are the magnetic angular momentum carried by the molecules on the closed channels, which are created by $\hat{\phi}^\dagger_{l_z=-1,0,1}(\boldsymbol{r})$ respectively. It will be convenient to discuss the physics with bases $\hat{\phi}^\dagger_{i=x,y,z}$, which are related with $\hat{\phi}^\dagger_{l_z=-1,0,1}$ through $\phi^\dagger_{\pm1} = (\phi^\dagger_x \pm i\phi^\dagger_y)/\sqrt{2}$, and $\phi^\dagger_0 = \phi^\dagger_z$. To focus on the physics arising from p-wave interaction, we will restrict our attention to the case where the closed channels are degenerate and background (non-resonant) interactions are negligible. The system we consider is characterized by Hamiltonian density

$$\begin{aligned}\mathcal{H} = &\sum_{\sigma=1,2} \hat{\psi}^\dagger_\sigma(-\frac{\nabla^2}{2m})\hat{\psi}_\sigma + \sum_{i=x,y,z} \hat{\phi}^\dagger_i(-\frac{\nabla^2}{4m} - \epsilon_0)\hat{\phi}_i \\ &+ \sum_{i=x,y,z} [\frac{\overline{g}}{2}\hat{\phi}^\dagger_i(\hat{\psi}_1, \hat{\psi}_2)\sigma_y\partial_i(\hat{\psi}_1, \hat{\psi}_2)^T + h.c.],\end{aligned} \tag{5.1}$$

where the atomic masses have been assumed to be the same, i.e. $m_1 = m_2 = m$, ϵ_0 is the detuning of molecule channels, $\bar{g}$ represents the strength of p-wave interaction, and σ_y is the Pauli matrix. Here the reduced Plank constant $\hbar$ has been set as 1.

Our model possesses $U_N(1) \times [SU(2)/U_y(1)] \times SO(3) \times Tr \times \mathcal{T}$ symmetries, where $U_N(1)$ is the global gauge symmetry, $[SU(2)/U_y(1)]$ the spin rotation symmetry around x and z directions, $SO(3)$ the 3-dimensional spatial rotation symmetry, Tr the translation symmetry in the absence of an external field, and $\mathcal{T}$ the time reversal symmetry. The symmetry transformations are listed in Tab. 2. It is worth noting that spin-rotation symmetry $[SU(2)/U_y(1)]$ is reduced to a spin-rotation symmetry $U_z(1)$ generated by σ_z in the presence of intraspecies s-wave interaction [42, 9]. In $SO(3)$ rotation symmetry, the atom fields are scalar fields, so they remain constant under $SO(3)$ transformation. However, molecular field $\hat{\phi}$ and gradient

operator $\boldsymbol{\nabla}$ are all vector fields, and they are transformed by a 3D spatial rotation. In Tab. 2, the generators of rotation symmetry $\lambda_{x,y,z}$ are given by,

$$\lambda_x = \begin{pmatrix} 0 & 0 & 0 \\ 0 & 0 & -i \\ 0 & i & 0 \end{pmatrix}, \lambda_y = \begin{pmatrix} 0 & 0 & i \\ 0 & 0 & 0 \\ -i & 0 & 0 \end{pmatrix}, \lambda_z = \begin{pmatrix} 0 & -i & 0 \\ i & 0 & 0 \\ 0 & 0 & 0 \end{pmatrix}. \tag{5.2}$$

Time-reversal symmetry $\mathcal{T}$ is given by reversing the momentum of atomic and molecular field operators, i.e. transforming $\hat{a}_{1,\mathbf{p}_1}, \hat{a}_{2,\mathbf{p}_2}$, and $\hat{b}_{i,\mathbf{p}_1+\mathbf{p}_2}$ as $\hat{a}_{1,-\mathbf{p}_1}, \hat{a}_{2,-\mathbf{p}_2}$, and $\hat{b}_{i,-\mathbf{p}_1-\mathbf{p}_2}$, respectively.

The total particle number N and atomic number difference δN are defined as below,

$$N_1 + N_2 + 2N_M = N, \quad N_1 - N_2 = \delta N, \tag{5.3}$$

where we use $N_{1,2} = \int d^3r \langle \hat{\psi}^\dagger_{1,2} \hat{\psi}_{1,2} \rangle$ and $N_M = \sum_{i=x,y,z} \int d^3r \langle \hat{\phi}^\dagger_i \hat{\phi}_i \rangle$ to denote the numbers of atoms and molecules, respectively. Here $\langle \cdots \rangle$ represents the average over the ground state. N and δN are conserved in our model, which correspond to the $U_N(1)$ and $[SU(2)/U_y(1)]$ symmetries.

5.2 Mean-field Ground State

As the foundation of beyond-mean-field study, we need to characterize the ground state at the mean-field level at first. We use the mean fields $\Psi_1 = \langle \hat{\psi}_1 \rangle$, $\Psi_2 = \langle \hat{\psi}_2 \rangle$ and $\Phi_i = \langle \hat{\phi}_i \rangle$ to describe the atomic and molecular condensates. The mean-field ground state of a p-wave resonant Bose gas including considerable large intraspecies s-wave interaction has been systematically discussed before [42, 9]. Three mean-field phases for the ground states: atomic (ASF), atomic-molecular (AMSF) and molecular (MSF) superfluid, are found. Typically, the atomic condensates carry finite momentum due to the p-wave interaction in AMSF phase. Actually, the ground-state phase diagram of our model is similar to the case there. Due to the lack of intraspecies s-wave interaction (or due to weak intraspecies s-wave interaction) in our model, it is shown that such previously known types of ground state are unstable at the mean field level.

Phase	ϵ_0	n_M	$n_1 = n_2$	Q	μ	Z	E_0/V
ASF	$\epsilon_0 < -\frac{1}{2}\overline{g}^2 mn$	0	$\frac{1}{2}n$	0	0	0	0
AMSF	$-\frac{1}{2}\overline{g}^2 mn < \epsilon_0 < \frac{1}{2}\overline{g}^2 mn$	$\frac{1}{4}n + \frac{\epsilon_0}{2\overline{g}^2 m}$	$\frac{1}{4}n - \frac{\epsilon_0}{2\overline{g}^2 m}$	$-\overline{g}m\sqrt{\frac{1}{4}n + \frac{\epsilon_0}{2\overline{g}^2 m}}$	$-\frac{1}{8}\overline{g}^2 mn - \frac{1}{4}\epsilon_0$	0	$-\frac{1}{16\overline{g}^2 m}(\overline{g}^2 mn + 2\epsilon_0)^2$
MSF	$\epsilon_0 > \frac{1}{2}\overline{g}^2 mn$	$\frac{1}{2}n$	0	$-\frac{1}{\sqrt{2}}\overline{g}m\sqrt{n}$	$-\frac{1}{4}\overline{g}^2 mn$	0	$-\frac{1}{2}\epsilon_0 n$

Table 3: Table of ground state phases. Here we have three phases by setting different detuning. ASF, AMSF and MSF are the atomic, atomic-molecular and molecular condensate phases, respectively.

As the typical feature of p-wave interaction, the atomic condensates generally carry finite momentum due to the shift of energy minimum in momentum space by the interaction terms [42, 9]. Although a general description of atomic order parameters should be written as $\Psi_1 = \sum_{\mathbf{Q}_n} \Psi_{1,\mathbf{Q}_n} e^{-i\mathbf{Q}_n\cdot\mathbf{r}}$ and $\Psi_2 = \sum_{\mathbf{Q}_n} \Psi_{2,-\mathbf{Q}_n} e^{i\mathbf{Q}_n\cdot\mathbf{r}}$, where $\mathbf{Q}_n$ is the set of possible momentums, it is generally expected that the assumption $\mathbf{Q}_n = \mathbf{Q}$ is sufficient to capture the qualitative picture of the ground state. That is, the order parameters can be taken as

$$\Psi_1 = \Psi_{1,Q} e^{-i\mathbf{Q}\cdot\mathbf{r}}, \quad \Psi_2 = \Psi_{2,-Q} e^{i\mathbf{Q}\cdot\mathbf{r}}. \tag{5.4}$$

Correspondingly the molecular components are space-independent, since the molecular fields only feel a homogeneous potential by atoms. Considering the symmetries of our model, we have the following ground-state ansatz

$$\begin{aligned}
\Psi &= \sqrt{n_A} e^{i\theta} e^{i(\theta_x\sigma_x + \theta_z\sigma_z)} \begin{pmatrix} \cos\chi_A e^{-i\mathbf{Q}\cdot\mathbf{r}} \\ \sin\chi_A e^{i\mathbf{Q}\cdot\mathbf{r}} \end{pmatrix}, \\
\mathbf{Q} &= e^{i\sum_{i=x,y,z}\overline{\theta}_i\lambda_i}\mathbf{Q}_0, \\
\Phi &= \sqrt{n_M} e^{i(2\theta+\theta_M)} e^{i\sum_{i=x,y,z}\overline{\theta}_i\lambda_i} \begin{pmatrix} \cos\chi_M \\ i\sin\chi_M \\ 0 \end{pmatrix},
\end{aligned} \tag{5.5}$$

where $\theta, \theta_M \in [0, 2\pi)$ are $U(1)$ phases, $\theta_{x,z} \in [0, 2\pi)$ are $[SU(2)/U_y(1)]$ spin rotation angles, $\overline{\theta}_{x,y,z}$ are $SO(3)$ rotation angles, $\chi_A, \chi_M \in [0, 2\pi)$, $\mathbf{Q}_0 = (Q_{0,x}, Q_{0,y}, Q_{0,z})^T$ is an arbitrary

real three dimensional vector, $n_A = (N_1 + N_2)/V, n_M = N_M/V$ with system volume V are the total atomic density and molecular density respectively.

Furthermore, we derive the free energy density by substituting the above ansatz (5.5) to the Hamiltonian density (5.1)

$$\begin{aligned} F/V = & \sum_{\sigma=1,2} \frac{Q^2}{2m} n_\sigma - \epsilon_0 n_M - \mu(n_1 + n_2 + 2n_M - n) \\ & + \frac{\overline{g}}{2} n_A \sqrt{n_M} \sin 2\chi_A [e^{-i\theta_M} (\cos\chi_M, -i\sin\chi_M, 0) \\ & \cdot \mathbf{Q}_0 + h.c] - Z(n_1 - n_2), \end{aligned} \tag{5.6}$$

where $n_{1,2} = N_{1,2}/V$, μ and Z are the Lagrange multipliers set for the conservations of the total particle number and atom-number difference. For simplicity, we only consider a nonpolarized situation in this paper, i.e. $n_1 = n_2 = n_A/2$, and fix the total particle number. The free energy density does not depend on $\theta, \theta_{x,z}, \overline{\theta}_{x,y,z}$. To minimize the free energy, we obtain the optimal values for the parameters: $\theta_M = 0, \chi_A = \pi/4, \chi_M = 0, Q_{0,x} = |\mathbf{Q}|, Q_{0,y,z} = 0$, from which we can see that Φ is real and parallel to $\mathbf{Q}$ by setting $\theta = 0$. To be more convenient, we set $\overline{\theta}_y = \pi/2, \overline{\theta}_{x,z} = 0$ so that $\mathbf{Q}$ and Φ are aligned to z direction. Without loss of generosity, we choose $\overline{g}$ to be negative (if $\overline{g} > 0$, $\mathbf{Q}$ will be opposite to Φ, however, it gives us the same phases and LHY corrections as we obtain below). Gross-Pitaevskii (GP) equations can be derived from the free energy density formula, and we obtain the optimized solutions to minimize the free energy.

Similar to previous chapter, the ground state phase diagram of our model is also divided into three phases for different detuning ϵ_0, where the ground state phases are listed in the Tab. 3. Here ASF refers to the atomic superfluid phase, where only atomic condensates exist. Note that there is no superfluidity here due to the absence of background atom-atom interaction, where the name of phase is only taken to be consistent with previous convention [42, 9]. AMSF refers to the atomic-molecular superfluid phase, where atom and molecular condensates are present in the same phase. MSF with only molecular condensate is the molecular superfluid phase.

In ASF phase, the condensate in both atomic species stays stationary due to vanishing $\mathbf{Q}$ and the two condensates do not interact. The atomic chemical potential remains zero.

In AMSF phase, the rotation and time-reversal symmetries are all broken due to the finite-momentum condensates. The $SO(3)$ rotation symmetry is spontaneously broken into $SO(2)$ symmetry. In MSF phase, although the density of the atomic condensates is zero, we still have non-zero $\mathbf{Q}$. This results in an MSF excitation spectrum translated in momentum space by $\mathbf{Q}$ as we will see in section IV.

From Tab. 3, we can also find the total energy E_0 is proportional to particle number $N = nV$ in phases ASF and MSF, which is due to the lack of background atom-atom and molecule-molecule interactions in these phases, respectively. It means the total energy E_0 is constant, such that the ground state is stable, for a system with fixed total particle number. However, we can find it is energetically favorable to increase density n to reach lower total energy E_0 in AMSF phase. It implies that in this phase the mean-field ground state is unstable and tends to collapse into a state with smaller volume but large particle density when the total particle number is fixed. The instability of the ground state in AMSF phase also manifests itself in the fact that the excitation mode becomes complex in the long-wavelength limit $k \to 0$ [66]. It will be shown the ground state collapses into a small droplet after considering LHY correction [63]. In order to calculate this correction, we need to analyze the Bogoliubov excitation spectrum at first.

5.3 Bogoliubov Excitations

We will study the Bogoliubov excitation spectrum in this section. Following Bogoliubov's theory [67, 68], we expand the atomic and molecular fields around the ground-state mean fields,

$$\hat{\psi}_\sigma = \Psi_\sigma + \delta\hat{\psi}_\sigma, \quad \hat{\phi}_i = \Phi_i + \delta\hat{\phi}_i, \tag{5.7}$$

with the fluctuation fields $\delta\hat{\psi}_\sigma$ and $\delta\hat{\phi}_i$. For convenience, we furthermore expand $\delta\hat{\psi}_\sigma$ and $\delta\hat{\phi}_i$ with the Fourier transformation

$$\delta\hat{\psi}_\sigma = \frac{1}{\sqrt{V}}\sum_{\mathbf{k}} \delta\hat{a}_{\sigma,\mathbf{k}} e^{-i\mathbf{k}\cdot\mathbf{r}}, \quad \delta\hat{\phi}_i = \frac{1}{\sqrt{V}}\sum_{\mathbf{k}} \delta\hat{b}_{i,\mathbf{k}} e^{-i\mathbf{k}\cdot\mathbf{r}}, \tag{5.8}$$

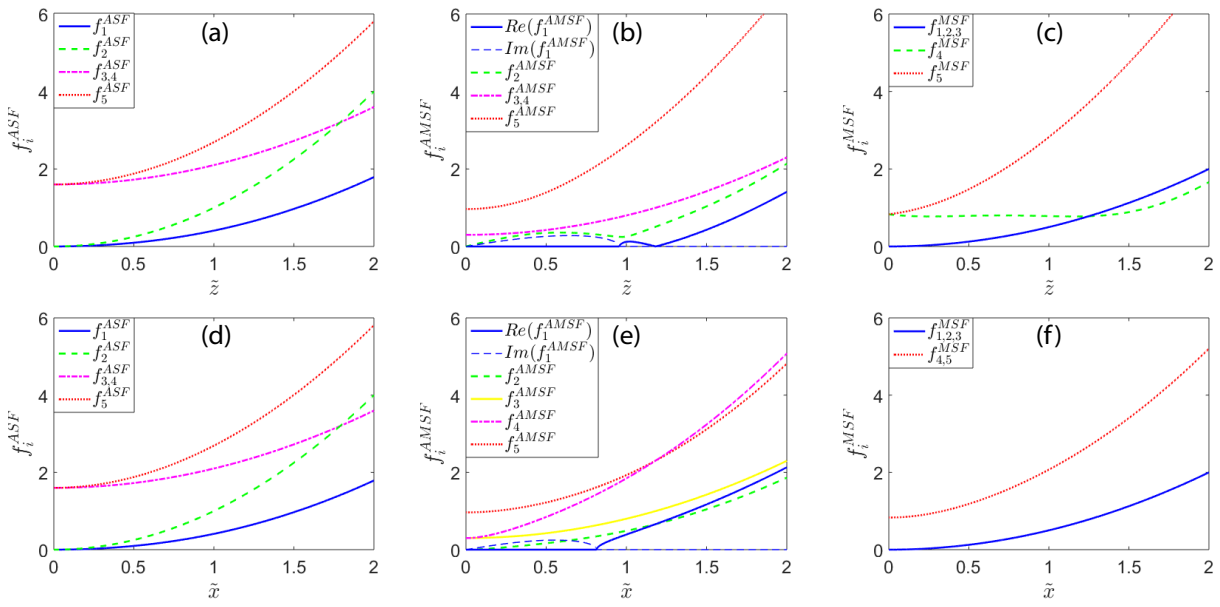

Figure 15: Schematic plot of dimensionless function f_j for subplots (a), (d): $\Delta = -0.4$; (b), (e): $\Delta = 0.1$; and (c), (f): $\Delta = 0.4$, which are inside ASF, AMSF and MSF phases, respectively. Here j means different modes. We can find the low-energy modes become imaginary in phase AMSF, which arises from the instability of the mean-field ground state. Here $\tilde{r} = \sqrt{\tilde{x}^2 + \tilde{y}^2 + \tilde{z}^2}$ represents the distance from the momentum-space origin.

where $\delta\hat{a}_{\sigma,\mathbf{k}}$ and $\delta\hat{b}_{i,\mathbf{k}}$ are the corresponding quantum fluctuation fields in momentum space. Substituting Eqs. (5.7) and (5.8) into Eq. (5.1) and keeping only the second-order terms (the first-order terms vanish due to the saddle-point solution and higher-order terms will be neglected), we can derive the Bogoliubov Hamiltonian. The Bogoliubov excitation spectrum can be extracted by diagonalizing Bogoliubov Hamiltonian.

ASF phase: This phase has only atomic condensates, i.e. $n_1 = n_2 = n/2$, $n_M = 0$ and the zero atomic condensates momentum $\mathbf{Q} = 0$. The Bogoliubov Hamiltonian can be written

as

$$\begin{aligned} H_f =& \frac{1}{2}\sum_{\mathbf{k}}\{\sum_{\sigma=1,2}\varepsilon_{\sigma,\mathbf{k}+\mathbf{Q}_\sigma}\delta\hat{a}^\dagger_{\sigma,\mathbf{k}+\mathbf{Q}_\sigma}\delta\hat{a}_{\sigma,\mathbf{k}+\mathbf{Q}_\sigma} \\ &+\sum_{i=x,y,z}\omega_{i,k}\delta\hat{b}^\dagger_{i,k}\delta\hat{b}_{i,k} - 2\sum_{\sigma,i}\alpha_{i,\overline{\sigma},\mathbf{k}}\delta\hat{b}^\dagger_{i,k}\delta\hat{a}_{\sigma,\mathbf{k}+\mathbf{Q}_\sigma} \\ &+h.c.\}, \end{aligned} \tag{5.9}$$

where $\overline{\sigma}=3-\sigma,\sigma=1,2,\quad \mathbf{Q}_1=-\mathbf{Q}_2=\mathbf{Q}$, and the parameters in the above equation are given as

$$\begin{aligned} &\varepsilon_{\sigma,\mathbf{k}}=\epsilon_k=\frac{k^2}{2m},\quad \omega_{i,\mathbf{k}}=\frac{1}{2}\epsilon_k+\frac{1}{2}\overline{g}^2mn, \\ &\alpha_{i,\sigma,\mathbf{k}}=(-1)^\sigma\frac{1}{2\sqrt{2}}\overline{g}\sqrt{n}k_i. \end{aligned} \tag{5.10}$$

The corresponding Bogoliubov excitation spectrum is given by

$$E^{ASF}_{j,\mathbf{k}}=\frac{1}{4}\overline{g}^2mnf^{ASF}_j(\tilde{x},\tilde{y},\tilde{z}), j=1,\cdots,5 \tag{5.11}$$

where f^{ASF}_j is a dimensionless function, j corresponds to different modes and the dimensionless variables $\tilde{x}=\frac{k_x}{\overline{g}m\sqrt{n}},\tilde{y}=\frac{k_y}{\overline{g}m\sqrt{n}},\tilde{z}=\frac{k_z}{\overline{g}m\sqrt{n}}$.

We show f^{ASF}_j along the radial direction in Fig. 15(a) and (d). The spectrum is symmetric in all directions and has two gapless atomic modes. The quadratic dispersions of gapless mode are due to the absence of atom-atom interaction.

AMSF phase: In AMSF phase, particles are condensed into both the atomic and molecular channels, and the atomic condensates carry opposite finite momentums. The directions of atomic momentum $\mathbf{Q}$ and molecular condensates order parameter $\Phi=(\Phi_x,\Phi_y,\Phi_z)$ are parallel in mean-field ground state, where the direction of Φ is defined by the it three spatial components. For convenience, we build the coordinate so that this direction is aligned along z axis. The Bogoliubov Hamiltonian is written as

$$\begin{aligned} H_f =& \sum_{\mathbf{k}}\{\sum_{\sigma=1,2}\frac{1}{2}\varepsilon_{\sigma,\mathbf{k}+\mathbf{Q}_\sigma}\delta\hat{a}^\dagger_{\sigma,\mathbf{k}+\mathbf{Q}_\sigma}\delta\hat{a}_{\sigma,\mathbf{k}+\mathbf{Q}_\sigma} \\ &+\sum_i\frac{1}{2}\omega_{i,k}\delta\hat{b}^\dagger_{i,k}\delta\hat{b}_{i,k}+t_{\mathbf{k}+\mathbf{Q}}\delta\hat{a}_{1,\mathbf{k}+\mathbf{Q}}\delta\hat{a}_{2,-\mathbf{k}-\mathbf{Q}} \\ &-\sum_{\sigma,i}\alpha_{i,\overline{\sigma},\mathbf{k}}\delta\hat{b}^\dagger_{i,k}\delta\hat{a}_{\sigma,\mathbf{k}+\mathbf{Q}_\sigma}+h.c.\}, \end{aligned} \tag{5.12}$$

where the parameters in the above equation are given by

$$\begin{aligned}
&\varepsilon_{\sigma,\mathbf{k}} = \epsilon_k + \frac{1}{8}\overline{g}^2 mn + \frac{1}{4}\epsilon_0, \quad \omega_{i,\mathbf{k}} = \frac{1}{2}\epsilon_k + \frac{1}{4}\overline{g}^2 mn - \frac{1}{2}\epsilon_0, \\
&t_{\mathbf{k}} = -\overline{g}\sum_i \Phi_i^* k_i, \quad \alpha_{i,\overline{\sigma},\mathbf{k}} = \pm\overline{g}\sqrt{n_\sigma}(Q_{\sigma,i} - k_i/2),
\end{aligned} \tag{5.13}$$

with $\epsilon_k = \frac{k^2}{2m}$, $\sigma = 1, 2$ (correspondingly $\bar{\sigma} = 2, 1$), $\mathbf{Q}_1 = \mathbf{Q}$ and $\mathbf{Q}_2 = -\mathbf{Q}$. The Bogoliubov excitation spectrum can be written as

$$E_{j,\mathbf{k}}^{AMSF} = \frac{1}{4}\overline{g}^2 mn f_j^{AMSF}(\tilde{x}, \tilde{y}, \tilde{z}, \Delta), j = 1, \cdots, 5 \tag{5.14}$$

where f_j^{AMSF} is a dimensionless function, j corresponds to different modes, the dimensionless variables $\tilde{x} = \frac{k_x}{\overline{g}m\sqrt{n}}, \tilde{y} = \frac{k_y}{\overline{g}m\sqrt{n}}, \tilde{z} = \frac{k_z}{\overline{g}m\sqrt{n}}$ and $\Delta = \frac{\epsilon_0}{2\overline{g}^2 mn}$ is the dimensionless detuning.

The schematic plots of f_j^{AMSF} are shown in Fig. 15(b) and (e) along z and x directions respectively. As we can see from the two figures, the blue-dashed curve shows imaginary mode consistent with the instability of the mean-field ground state [66], which is absent when the ground state is stable [42, 9]. Actually, the true ground state is lost due to the homogeneous assumption (the system with finite particle number will collapse into a droplet shape that breaks the spatial translation symmetry) and the absence of LHY correction. On the other hand, the inverse of the largest momentum carried by imaginary modes is expected to be comparable with the size of the droplet [66]. The minima on the blue-solid curve in Fig. 15(b) corresponds to the nonvanishing momentum $2\mathbf{Q}$ in AMSF phase, where the atomic condensates locate. That the spectrum softens to zero at $k_z = 2Q$ implies our ansatz correctly captures the feature of the ground state.

MSF phase: In this phase, we have $n_M = n/2$ and $n_1 = n_2 = 0$. The Bogoliubov Hamiltonian is given as

$$\begin{aligned}
H_f = &\sum_{\mathbf{k}}\{\sum_{\sigma=1,2}\frac{1}{2}\varepsilon_{\sigma,\mathbf{k}+\mathbf{Q}_\sigma}\delta\hat{a}^\dagger_{\sigma,\mathbf{k}+\mathbf{Q}_\sigma}\delta\hat{a}_{\sigma,\mathbf{k}+\mathbf{Q}_\sigma} \\
&+ t_{\mathbf{k}+\mathbf{Q}}\delta\hat{a}_{1,\mathbf{k}+\mathbf{Q}}\delta\hat{a}_{2,-\mathbf{k}-\mathbf{Q}} \\
&+ \sum_i \frac{1}{2}\omega_{i,k}\delta\hat{a}^\dagger_{i,k}\delta\hat{a}_{i,k} + h.c.\},
\end{aligned} \tag{5.15}$$

where $\varepsilon_{\sigma,\mathbf{k}} = \epsilon_k + \frac{1}{4}\overline{g}^2 mn$, $\omega_{i,\mathbf{k}} = \frac{1}{2}\epsilon_k$ and $t_{\mathbf{k}} = -\overline{g}\sum_i \Phi_i^* k_i$.

Fortunately, we can derive analytical formulas for the excitation modes in this phase, i.e.

$$
\begin{aligned}
E^{MSF}_{1,2,3,\mathbf{k}} &= \frac{1}{8}\overline{g}^2 mn\tilde{r}^2, \\
E^{MSF}_{4,\mathbf{k}} &= \frac{1}{4}\overline{g}^2 mn\sqrt{(\tilde{r}^2+2\Delta-\frac{1}{2})(\tilde{r}^2-2\sqrt{2}\tilde{r}\cos\gamma+2\Delta+\frac{3}{2})}, \\
E^{MSF}_{5,\mathbf{k}} &= \frac{1}{4}\overline{g}^2 mn\sqrt{(\tilde{r}^2+2\Delta-\frac{1}{2})(\tilde{r}^2+2\sqrt{2}\tilde{r}\cos\gamma+2\Delta+\frac{3}{2})}.
\end{aligned}
\tag{5.16}
$$

where $\tilde{r}^2 = (k_x^2+k_y^2+k_z^2)/\overline{g}^2m^2n$ and γ is the angle between z axis and unit vector $\hat{\mathbf{k}}$ as we have aligned $\hat{\mathbf{Q}}$ along z. Similar to what we defined in ASF and AMSF phases, we rewrite the excitation modes in this formula

$$
E^{MSF}_{j,\mathbf{k}} = \frac{1}{4}\overline{g}^2 mn f^{MSF}_j(\tilde{x},\tilde{y},\tilde{z},\Delta), j = 1,\cdots,5. \tag{5.17}
$$

Fig. 15(c) and (f) are the corresponding f^{MSF}_j along z and x directions. In Fig. 15(c), the red dotted and green dashed curves are the two atom modes respectively, and the minima on green dashed curve corresponds to the nonvanishing momentum $2\mathbf{Q}$. The blue curve denotes the triply-degenerated molecule modes. In Fig. 15(f), the red curve denotes the doubly-degenerated atom modes and blue curve denotes the triply-degenerated molecule modes.

5.4 LHY Correction

The LHY correction is the leading-order correction of quantum fluctuation. It is composed of Bogoliubov excitation energies, commutation energies which appear due to the commutation relations of Nambu basis, and energy correction due to the interaction renormalization. Here the interaction renormalization is employed to remove the energy divergence arising in collecting the energy of quantum fluctuation [63]. Let us review the renormalization procedure before going ahead.

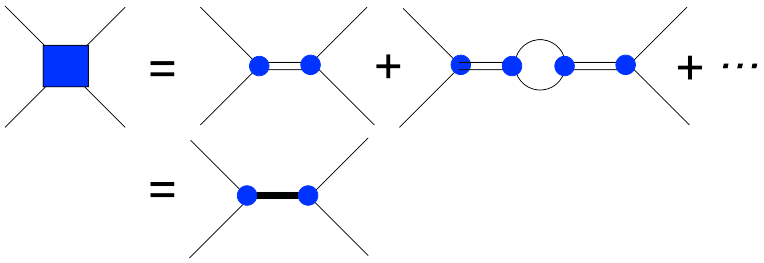

Figure 16: Diagram for calculating the T matrix for p-wave interaction. Single lines denote the bare atom propagators $G^{(0)}$, double lines denote the bare molecule propagators $D^{(0)}$, and the bold one denotes the renormalized molecule propagators D. The blue square represents the T matrix: $-iT^{(l_z)}_{\mathbf{k},\mathbf{k}'}$. The blue dot represents the interaction vertex: $-i\overline{g}kY_{1,l_z}(\hat{\mathbf{k}})$.

To remove the divergence appears in the calculation of LHY correction, we need to renormalize the interaction parameter $\overline{g}$ and detuning ϵ_0 [63, 66]. As shown in Fig. 16, the two body T matrix for p wave interaction is given by [69]

$$\begin{aligned} &-iT^{(l_z)}_{\mathbf{k},\mathbf{k}'}(k) = D^{(0)}(k)(-i\overline{g})^2k^2Y_{1,l_z}(\hat{\mathbf{k}})Y^*_{1,l_z}(\hat{\mathbf{k}}') \\ &+ D^{(0)2}(k)(-i\overline{g})^4 2\Pi_{l_z}(k)k^2Y_{1,l_z}(\hat{\mathbf{k}})Y^*_{1,l_z}(\hat{\mathbf{k}}') + ... \\ &= D(k)(-i\overline{g})^2k^2Y_{1,l_z}(\hat{\mathbf{k}})Y^*_{1,l_z}(\hat{\mathbf{k}}'). \end{aligned} \tag{5.18}$$

where the index l_z denotes different interacting channels $l_z = -1, 0, 1$. $Y_{1,l_z}(\hat{\mathbf{k}})$ is the l_z-th channel of the first order spherical harmonics. $D^{(0)}(k)$ is the p-wave scattering propagator and $\Pi_{l_z}(k)$ is the polarization bubble for channel l_z, which are given by

$$D^{(0)}(k) = \frac{i}{k^2/m + \epsilon_0 + i0+}, \tag{5.19}$$

and

$$\Pi_{l_z}(k) = \int \frac{d^3p}{(2\pi)^3} \frac{ip^2|Y_{1,l_z}(\hat{\mathbf{p}})|^2}{k^2/m - p^2/m + i0+}. \tag{5.20}$$

Using Eq. (5.18), we yield

$$D^{-1}(k) = [D^{(0)}(k)]^{-1} - (-i\overline{g})^2\Pi_{l_z}(k). \tag{5.21}$$

Comparing k^0 term and k^2 term on both sides of Eq. (5.21), we obtain the renormalization relations [70],

$$\frac{\tilde{\epsilon}_0}{\tilde{\overline{g}}^2} = \frac{\epsilon_0}{\overline{g}^2} + \int \frac{d^3p}{(2\pi)^3} m|Y_{1,l_z}(\hat{\mathbf{p}})|^2, \tag{5.22}$$

and

$$\frac{1}{\tilde{\overline{g}}^2} = \frac{1}{\overline{g}^2} - \int \frac{d^3p}{(2\pi)^3} m^2 \frac{|Y_{1,l_z}(\hat{\mathbf{p}})|^2}{p^2}, \tag{5.23}$$

where $\tilde{\epsilon}_0$ and $\tilde{\overline{g}}$ are the renormalized detuning and p-wave interacting strength respectively.

Applying these renormalization relations into the ground state energy in different phases, one obtains the renormalized mean-field ground state energies

$$E_{0,r}^{ASF}/V = 0, \tag{5.24}$$

$$E_{0,r}^{AMSF}/V = \int \frac{d^3k}{(2\pi)^3}\left(\frac{1}{12}\overline{g}^2 mn + \frac{1}{6}\epsilon_0 + \frac{\overline{g}^4 m^2 n^2 - 4\epsilon_0^2}{72k^2}\right), \tag{5.25}$$

and

$$E_{0,r}^{MSF}/V = \int \frac{d^3k}{(2\pi)^3}\left(\frac{1}{6}\overline{g}^2 mn + \frac{\overline{g}^2 mn - 2\epsilon_0}{12k^2}\right). \tag{5.26}$$

LHY correction is the zero-point energy corresponding to the Bogoliubov modes. It is necessary to remove the commutation energies which are the diagonal terms in the Bogoliubov Hamiltonian. The commutation energies for different phases are listed below,

$$E_c^{ASF}/V = \int \frac{d^3k}{(2\pi)^3} \frac{k_x^2 + k_y^2 + k_z^2}{2m} + \frac{3k^2}{8m} + \frac{3\overline{g}^2 mn}{8}, \tag{5.27}$$

$$\begin{aligned} E_c^{AMSF}/V &= \int \frac{d^3k}{(2\pi)^3}\frac{1}{2}\left(\frac{k_x^2 + k_y^2 + (k_z + \overline{g}m\sqrt{\frac{1}{4}n + \frac{\epsilon_0}{2\overline{g}^2 m}})^2}{2m} + \frac{1}{8}\overline{g}^2 mn + \frac{1}{4}\epsilon_0\right) \\ &+ \frac{1}{2}\left(\frac{k_x^2 + k_y^2 + (k_z - \overline{g}m\sqrt{\frac{1}{4}n + \frac{\epsilon_0}{2\overline{g}^2 m}})^2}{2m} + \frac{1}{8}\overline{g}^2 mn + \frac{1}{4}\epsilon_0\right) \\ &+ \frac{3}{2}\left(\frac{k^2}{4m} + \frac{1}{4}\overline{g}^2 mn - \frac{1}{2}\epsilon_0\right), \end{aligned} \tag{5.28}$$

$$\begin{aligned} E_c^{MSF}/V &= \int \frac{d^3k}{(2\pi)^3}\frac{1}{2}\left(\frac{k_x^2 + k_y^2 + (k_z + \overline{g}m\sqrt{n/2})^2}{2m} + \frac{1}{4}\overline{g}^2 mn\right) \\ &+ \frac{1}{2}\left(\frac{k_x^2 + k_y^2 + (k_z - \overline{g}m\sqrt{n/2})^2}{2m} + \frac{1}{4}\overline{g}^2 mn\right) + \frac{3k^2}{8m} \end{aligned} \tag{5.29}$$

From the analysis of Bogoliubov spectrum and interaction renormalization, we obtain the LHY correction densities in different phases, $E^{\alpha}_{LHY}/V = \sum_{j=1}^{5} \int \frac{d^3k}{(2\pi)^3} E^{\alpha}_{j,\mathbf{k}} - E^{\alpha}_{c}/V + E^{\alpha}_{0,r}/V$, where $\alpha = ASF, AMSF, MSF$.

$$\begin{aligned} E^{ASF}_{LHY}/V = &- \overline{g}^5 m^4 n^{2.5} \int \frac{d^3\tilde{r}}{(2\pi)^3} (\sum_{j=1}^{5} \frac{1}{4} f_j^{ASF} \\ &- \frac{7}{8}\tilde{r}^2 + 3\Delta), \end{aligned} \tag{5.30}$$

$$\begin{aligned} E^{AMSF}_{LHY}/V = &- \overline{g}^5 m^4 n^{2.5} \int \frac{d^3\tilde{r}}{(2\pi)^3} (\sum_{j=1}^{5} \frac{1}{4} f_j^{AMSF} \\ &- \frac{7}{8}\tilde{r}^2 - \frac{13}{24} + \frac{5}{6}\Delta + \frac{1-16\Delta^2}{72\tilde{r}^2}), \end{aligned} \tag{5.31}$$

and

$$\begin{aligned} E^{MSF}_{LHY}/V = &- \overline{g}^5 m^4 n^{2.5} \int \frac{d^3\tilde{r}}{(2\pi)^3} (\sum_{j=1}^{5} \frac{1}{4} f_j^{MSF} \\ &- \frac{7}{8}\tilde{r}^2 - \frac{1}{3} + \frac{1-4\Delta}{12\tilde{r}^2}). \end{aligned} \tag{5.32}$$

Unlike the AMSF and MSF phases, there is no particle-hole coupling as presented in Eq. (5.9) in the ASF phase, which results in the cancellation between the total excitation energies and the commutation energies in LHY calculation. As a proof to this inference, we find Eq. (5.30) shows result $E^{ASF}_{LHY} = 0$ numerically. Combining the mean-field ground state energy densities and LHY corrected energy densities yields the total ground state energy density $E_g/V = E_0/V + E_{LHY}/V$ for different phases as follows,

$$E^{ASF}_{g}/V = 0, \tag{5.33}$$

$$\begin{aligned} E^{AMSF}_{g}/V = &- \overline{g}^5 m^4 n^{2.5} F(\Delta) - \frac{1}{16}\overline{g}^2 m n^2 \\ &- \frac{1}{4}\epsilon_0 n - \frac{1}{4}\frac{\epsilon_0^2}{\overline{g}^2 m}, \end{aligned} \tag{5.34}$$

and

$$E^{MSF}_{g}/V = -\overline{g}^5 m^4 n^{2.5} F(\Delta) - \frac{1}{2} n \epsilon_0, \tag{5.35}$$

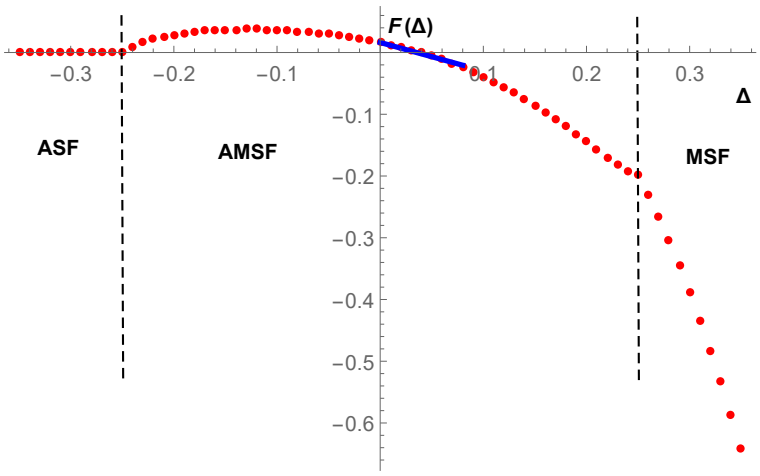

Figure 17: Schematic plot of $F(\Delta)$. The blue solid line is a linearized approximation for the regime with a stabilized particle number density.

where $F(\Delta)$ is depicted in Fig. 17 numerically.

We plot the total energy density versus particle density for different detuning in Fig. 18. As we can see, for $\epsilon_0 > 0$, the minimum energy density is well defined, and lies in the AMSF phase. It implies that there exists a self-stabilized state at around the minimum. If the particle number is finite, it forms a quantum droplet [51]. We also depict the dependence between the particle density of the self-stabilized state n_s and the detuning ϵ_0 in Fig. 19. It is shown the stabilized density is almost linearly proportional to ϵ_0. However, if $\epsilon_0 < 0$, the energy density is degenerated inside ASF phase, but it can be broken by introducing an atom-atom s-wave interaction. Typically, the atom-atom s-wave interaction is repulsive and the corresponding LHY correction is also positive [63]. Therefore, the lowest energy density lies at $n = 0$ inside ASF phase. For this reason, we do not expect a self-stabilized state when the detuning $\epsilon_0 < 0$.

The diluteness of p-wave interacting gas can be characterized by the product between the particle density and the scattering volume v_p [70, 71], i.e. $nv_p = \overline{g}^2 mn/(16\pi^2\epsilon_0)$. Therefore, we can rewrite the ground-state energy given by mean-field theory (MFT) and the LHY

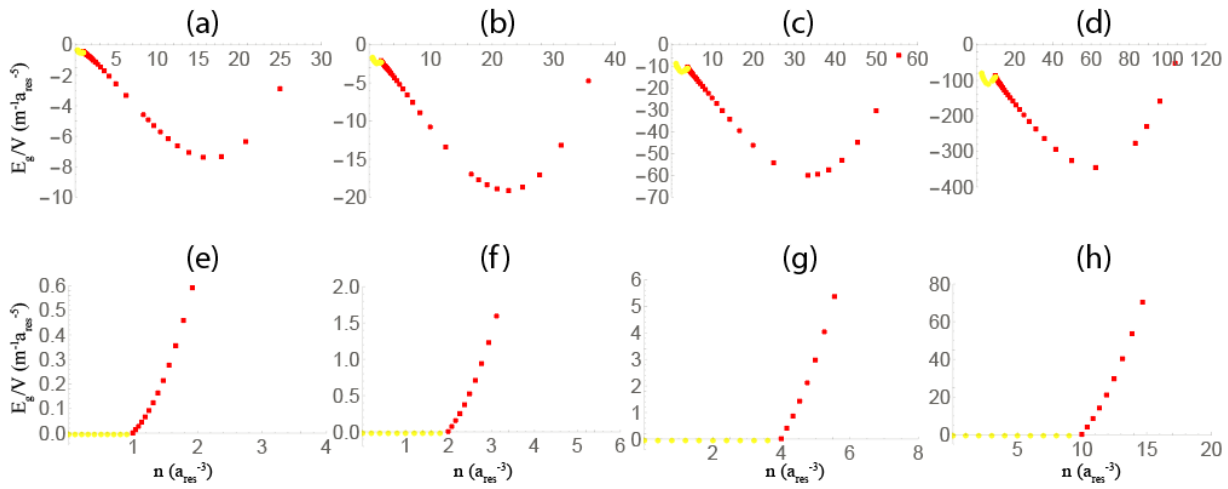

Figure 18: Total ground-state energy density versus total number density for different detuning: $\epsilon_0 m a_{res}^2 = 0.5$ (a), 1 (b), 2 (c), 5 (d), -0.5 (e), -1 (f), -2 (g), -5 (h). In subfigures with $\epsilon_0 > 0$, the yellow circle (red square) dots represent the energies in MSF (AMSF) phase. The minimum energy density is presented with a finite number density after we introduce the LHY correction and lies in the AMSF phase. In subfigures with $\epsilon_0 < 0$, the yellow circle (red square) dots represent the energies in ASF (AMSF) phase. To emphasize the dominance of p-wave interaction, we choose $a_{res} = 10^3 a_0$ with the Bohr radius a_0 as the unit of length, which is typically far larger than the background scattering length. We set the Planck constant $\hbar$ as 1 for convenience.

correction in terms of the diluteness as

$$E_{AMSF}^{MFT}/V = -\frac{\epsilon_0^2}{64\bar{g}^2 m}(32\pi^2 n v_p + 4)^2, \tag{5.36}$$

$$E_{MSF}^{MFT}/V = -\frac{\epsilon_0^2}{4\bar{g}^2 m} 32\pi^2 n v_p, \tag{5.37}$$

and

$$E^{LHY}/V = m^{1.5}(\epsilon_0/2)^{2.5}(32\pi^2 n v_p)^{2.5} F(\frac{1}{32\pi^2 n v_p}). \tag{5.38}$$

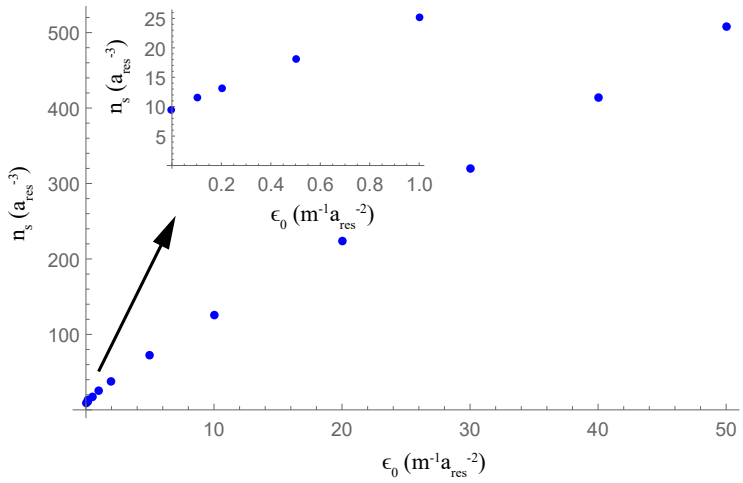

Figure 19: The stabilized density n_s versus detuning ϵ_0. The stabilized density n_s is almost proportional to detuning ϵ_0 linearly. As ϵ_0 becomes larger, $\Delta_s = \frac{\epsilon_0}{2\overline{g}^2 m n_s}$ converges to ≈ 0.08.

The diluteness of the self-stabilized state with respect to detuning is shown in Fig. 20. As detuning approaches zero, the diluteness tends to diverge, which may indicate that higher order corrections besides MFT and LHY are needed. But for a large detuning regime, the mixture is dilute, so that it is reasonable to characterize our model with only first order beyond-mean-field calculation.

5.5 Quantum Droplets

According to the above analysis, we find the mean-field collapsing state becomes self-stabilized after considering beyond-mean-field correction. This self-stabilized state forms a quantum droplet when the particle number is finite [51]. To figure out the density distribution of the quantum droplet, we will derive an effective theory to characterize the density profile. Here we employ function $\xi(\mathbf{r})$ to characterize the droplet density profile. If the system size is infinite, we have solution $\xi(\mathbf{r}) = 1$ as it should be a uniform gas. However, if the system

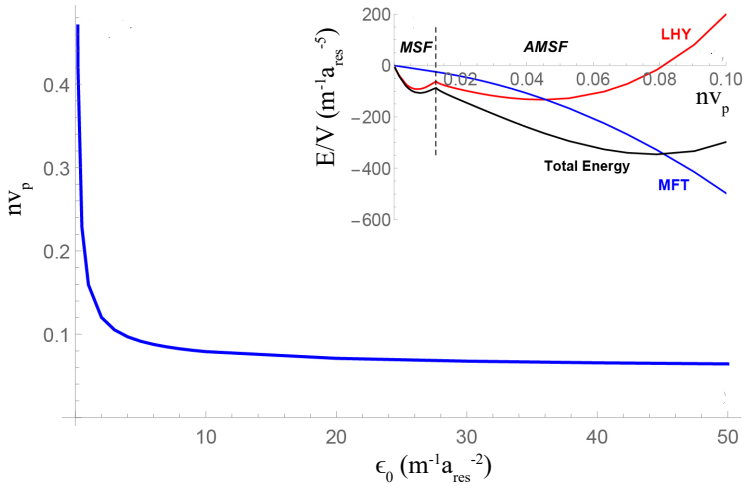

Figure 20: Relation between the diluteness and the detuning. As detuning approaches zero, the diluteness tends to diverge, which may indicate that higher order corrections besides MFT and LHY are needed. But for a large detuning regime, the mixture is dilute, so that it is reasonable to characterize our model with only first order beyond-mean-field calculation. The inset shows the energy comparison for different diluteness, as we set $\epsilon_0 m a_{res}^2 = 5$. The lowest total energy is ensured to appear in the dilute regime.

size is finite, the density profile will be inhomogeneous.

As a qualitative analysis, we will take the local density approximation (LDA). With this approximation, the order parameters can be rewritten as [66],

$$\Psi_1 = \Psi_{1,\mathbf{Q}} e^{-i\mathbf{Q}\cdot\mathbf{r}}, \quad \Psi_2 = \Psi_{2,-\mathbf{Q}} e^{i\mathbf{Q}\cdot\mathbf{r}}, \tag{5.39}$$

and $\Phi = \sqrt{n_{s,M}}\xi(\mathbf{r})\hat{\mathbf{z}}$, where

$$\Psi_{1,\mathbf{Q}} = \sqrt{n_{s,1}}\xi(\mathbf{r}), \quad \Psi_{2,-\mathbf{Q}} = \sqrt{n_{s,2}}\xi(\mathbf{r}). \tag{5.40}$$

$n_{s,\{1,2,M\}}$ are the densities that correspond to the minimum of E_g/V as shown in Fig. 18. Here we have chosen $\hat{\mathbf{z}}$ direction due to the spontaneous breaking of $SO(3)$ rotation symmetry by $\mathbf{Q} = -\overline{g}m\sqrt{n_{s,M}}\xi(\mathbf{r})\hat{\mathbf{z}}$.

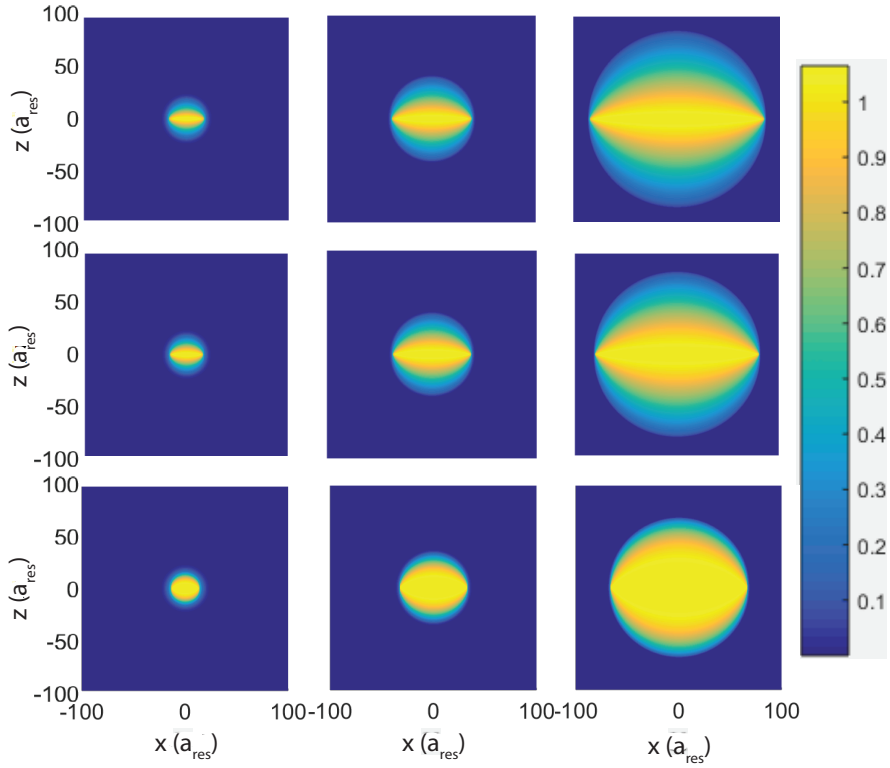

Figure 21: Density profile of the droplet. The background color represents $\xi = \sqrt{n(\mathbf{r})/n_s}$, where $n(\mathbf{r})$ is density at different locations and n_s is the stabilized density. The x axis and y axis for each subfigure label the x direction and z direction in real space. The detunings from the top row to the bottom row are $\epsilon_0 m a_{res}^2 = 0.5, 5, 50$ respectively. The normalization factor for ξ from the left column to the right column are $N/(n_s a_{res}^3) = 10^4, 10^5, 10^6$ respectively. When the particle number grows large enough with n_s fixed, it breaks $SO(3)$ symmetry clearly. As the detuning grows smaller and deep inside the AMSF phase, the droplet is more and more reduced along z axis.

To access the analytical form of effective Hamiltonian, an approximative form of $F(\Delta)$ at around the stable point is considered. For $\epsilon_0 > 0$, we find a linearized formula for $F(\Delta)$, which captures its behavior at around the minimum energy density inside the AMSF phase

$(0 < \Delta <\approx 0.08)$ [see Fig. 17]. It is written as

$$F(\Delta) \approx -0.460333\Delta + 0.01624807. \tag{5.41}$$

According to Eq. (5.34), the approximated total ground-state energy in AMSF phase is given by

$$\begin{aligned} E_g^{AMSF}/V = &-\frac{1}{16}\overline{g}^2 m n_s^2 - \frac{1}{4}\epsilon_0 n_s - \frac{1}{4}\frac{\epsilon_0^2}{\overline{g}^2 m} \\ &- 0.01625\overline{g}^5 m^4 n_s^{2.5} + 0.2302\epsilon_0 \overline{g}^3 m^3 n_s^{1.5}. \end{aligned} \tag{5.42}$$

Furthermore, by substituting Eqs. (5.39) and (5.40) to Eq. (5.42) along with the kinetic energy, we derive the effective Hamiltonian

$$\begin{aligned} \mathcal{H}_{eff} = \overline{g}^2 m n_s^2 \{ &[\frac{1}{\overline{g}^2 m^2 n_s}(\frac{3}{4}\Delta - \frac{5}{16}) + (\Delta^2 - \frac{1}{16})z^2\xi^2]\xi\nabla^2\xi \\ &-(2\Delta^2 + \frac{1}{2}\Delta)\xi^2 + 0.460333\Delta\overline{g}^3 m^3\sqrt{n_s}\xi^3 \\ &+(\Delta^2 - \frac{1}{16})\xi^4 - 0.01625\overline{g}^3 m^3\sqrt{n_s}\xi^5\} \ . \end{aligned} \tag{5.43}$$

The chemical potential $\tilde{\mu}$ is fixed by the normalization condition $\int d^3r|\xi|^2 = N/n_s$, where N is the total number of particles and n_s is the stabilized total density. The profile function $\xi(\mathbf{r})$ is determined by the GP equation

$$\begin{aligned} \tilde{\mu}\xi^2 = \overline{g}^2 m n_s^2 \{ &[\frac{1}{\overline{g}^2 m^2 n_s}(\frac{3}{4}\Delta - \frac{5}{16}) + 2(\Delta^2 - \frac{1}{16})z^2\xi^2]\xi\nabla^2\xi \\ &-(2\Delta^2 + \frac{1}{2}\Delta)\xi^2 + 0.690501\Delta\overline{g}^3 m^3\sqrt{n_s}\xi^3 \\ &+2(\Delta^2 - \frac{1}{16})\xi^4 - 0.0460202\overline{g}^3 m^3\sqrt{n_s}\xi^5\} \ , \end{aligned} \tag{5.44}$$

which is derived by minimizing the effective Hamiltonian.

The above GP equation is solved numerically by using the imaginary time evolution method. The solutions for different detuning and particle numbers are shown in Fig. 21. We can find the quantum droplet is typically suppressed in the z direction. The degrees of suppression decreases for a larger ϵ_0. Hence the droplet looks like a pancake when N/n_s is large enough but ϵ_0 is small (see the upper right subfigure of Fig. 21). We also show the section of the solution where $\epsilon_0 m a_{res}^2 = 0.5, N/(n_s a_{res}^3) = 10^6$ in Fig. 22. The density is found to suddenly fall to zero in the horizontal directions (x or y directions), while gently decreasing

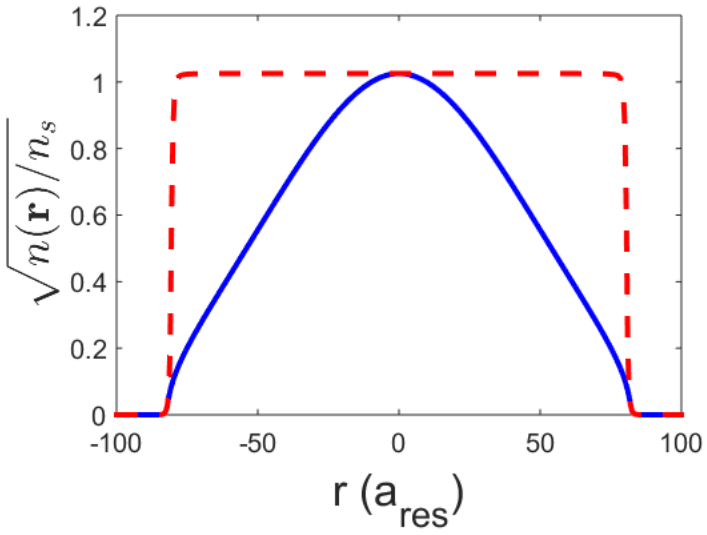

Figure 22: Density profile on the centered lines along x and z directions inside the droplet under condition $\epsilon_0 m a_{res}^2 = 0.5$ and $N/(n_s a_{res}^3) = 10^6$. The red dashed curve is the centered line along x direction and the blue solid curve is along z direction. The value on the plateau is almost constant and close to 1.025. If the system size is increased, the height of the plateau will be closer to 1.

to zero in the z direction. Except for the boundary regime, the profile varies smoothly everywhere, which implies that LDA could qualitatively catch the features of quantum droplet here. In fact, the anisotropy of quantum droplet arises from the spontaneous breaking of SO(3) rotation symmetry by finite-momentum atomic condensates. It is intrinsically different from the anisotropic quantum droplets in the presence of dipolar interaction [56, 57, 58, 59] or spin-orbit coupling [62], where the anisotropy arises from external fields. As we can see, the value on the plateau remains almost constant and close to 1, which will be exactly 1 when the system size goes to infinity. Another special feature of quantum droplet here is that the atomic components carry finite momentums due to the breaking of time-reversal symmetry.

5.6 Background s-wave Interactions

Hereinbefore we mainly focused on the case without background interactions. In the presence of the background s-wave interactions, which are characterized by

$$\begin{aligned}\hat{V}_{bg} =& g_1\hat{\psi}_1^\dagger\hat{\psi}_1^\dagger\hat{\psi}_1\hat{\psi}_1 + g_2\hat{\psi}_2^\dagger\hat{\psi}_2^\dagger\hat{\psi}_2\hat{\psi}_2 + g_{12}\hat{\psi}_1^\dagger\hat{\psi}_2^\dagger\hat{\psi}_2\hat{\psi}_1 \\ &+ g_{mm}^{(1)}\sum_{i,j=x,y,z}\hat{\phi}_i^\dagger\hat{\phi}_j^\dagger\hat{\phi}_j\hat{\phi}_i + g_{mm}^{(2)}\sum_{i,j=x,y,z}\hat{\phi}_i^\dagger\hat{\phi}_i^\dagger\hat{\phi}_j\hat{\phi}_j \\ &+ g_{am}\sum_{\sigma=1,2}\sum_{i=x,y,z}\hat{\psi}_\sigma^\dagger\hat{\phi}_i^\dagger\hat{\phi}_i\hat{\psi}_\sigma,\end{aligned} \tag{5.45}$$

where g_1, g_2 and g_{12} ($g_{mm}^{(1)}$ and $g_{mm}^{(2)}$) are the atom-atom (molecule-molecule) interaction coefficients and g_{am} is the atom-molecule interaction coefficient, the mean-field ground state energy in the AMSF phase (taking the polar molecular state [42, 9] as example) takes the form,

$$\begin{aligned}\frac{E_0}{V} =& [-4\epsilon_0^2(g_{aa} - 3g_{am} + 2g_{mm} + \overline{g}^2 m) \\ &- 4\epsilon_0 n(2g_{aa} - 2g_{am} + \overline{g}^2 m) \\ &\times (g_{aa} - 3g_{am} + 2g_{mm} + \overline{g}^2 m) \\ &+ (4g_{aa}^2 g_{am} + (3g_{am} - 2g_{mm} - \overline{g}^2 m)(-2g_{am} + \overline{g}^2 m)^2 \\ &- g_{aa}(12g_{am}^2 - 4g_{mm}^2 - 8g_{am}\overline{g}^2 m + \overline{g}^4 m^2))n^2] \\ &/[16(g_{aa} - 2g_{am} + g_{mm} + \overline{g}^2 m)^2].\end{aligned} \tag{5.46}$$

Here $g_{aa} = g_1 + g_2 + g_{12}$ and $g_{mm} = g_{mm}^{(1)} + g_{mm}^{(2)}$. In order to capture the profile of quantum droplet with finite particle number, we consider the ground-state energy with the canonical condition in this paper instead of the grand canonical condition in Refs. [42, 9], while we would like to emphasize that the statistic condition does not affect the stability mechanism of quantum droplet, which is mainly determined by intra-atomic interaction. When the p-wave interaction strength is far larger than the background interaction strengths, i.e. the effective p-wave interaction strength $g_p = m\bar{g}^2 \gg g_{aa}, g_{am}, g_{mm}$, we have $E_0/V = -\frac{(2\epsilon_0+\overline{g}^2 mn)^2}{16\overline{g}^2 m} + O(\delta_{aa}, \delta_{am}, \delta_{mm})$ with $\delta_{aa,am,mm} = g_{aa,am,mm}/m\bar{g}^2$, which implies that

the mean-field instability should exist in a finite regime of background-interaction parameters.

On the other hand, since the LHY corrections of s-wave interactions are typically proportional to $(g_s n)^{2.5}$ with the s-wave interaction strength g_s and average density n [63, 51], and that of p-wave interaction is proportional to $(g_p n)^{2.5}$ [see Eq. (5.31)], if the background s-wave interactions are weak enough with respect to the p-wave interaction, the background s-wave interactions should also not qualitatively affects the stabilization of the p-wave quantum droplet. Therefore, we can believe the presence of weak background s-wave interactions will not qualitatively affect the main conclusions of this paper. However, we have to point out that, to the best of our knowledge, the complete experimental data for the background interactions in a p-wave Feshbach resonance (especially the molecule-molecule interactions) is not available currently, and further investigations are necessary for judging if the quantum droplet could emerge under realistic conditions.

6.0 Fast Scrambling Without Appealing to Holographic Duality

The dynamics of thermalization in closed quantum systems has received immense attention in recent years [12, 3, 13, 14, 72, 73, 74, 75, 76]. A central focus of these studies has been the "scrambling" of quantum information [16, 17, 18, 19, 77, 78, 79, 80, 81, 82, 83, 84]. Scrambling is the process by which locally encoded information gets spread over non-local many-body degrees of freedom during the time evolution of a complex quantum system. This paradigm has been used to address a diverse array of questions in areas ranging from quantum chaos to quantum gravity [20, 21, 22, 23, 85, 86, 87, 88, 89, 90, 91, 92, 93]. Several recent experiments in a variety of analog quantum simulator platforms have successfully probed quantum scrambling [24, 25, 26, 27, 94, 95, 96, 97], thereby paving the path to answer fundamental questions about non-equilibrium quantum dynamics.

Black holes are the fastest scramblers known in nature. In the context of quantum information recovery, the scrambling time scale can be viewed as a lower bound on the time it takes between throwing information into a black hole and being able to recover it, with small error from the subsequent Hawking radiation [98]. It has also been described as the amount of time it takes for a qubit of information thrown into a black hole to become thoroughly "mixed" [99]. There are many methodologies in the current literature to calculate the scrambling time scale for black holes [99, 100, 101]. Depending on the particular approach one takes the exact mathematical expression for the scrambling time scale may vary. However, as diverse as they may be, it seems that the approaches described in [99, 100] give a time scale that can be roughly quantified by the following expression:

$$t_{scr} \sim \beta \ln(S). \tag{6.1}$$

Here, β is the inverse temperature of the system and S can be viewed as the number of microscopic degrees of freedom in the system which take part in the fast scrambling process. Unlike the normal scramblers, where the characteristic times are usually linear to system entropy or system size, the fast scramblers process information in characteristic times scaling logarithmically as shown in Eq. 6.1.

Motivated by advances in holography, researchers have studied quantum many-body systems that can exhibit fast scrambling. Perhaps, the most celebrated example of this is the Sachdev-Ye-Kitaev (SYK) model [102, 103, 104, 105, 106]. This model describes N Majorana fermions interacting via random infinite range interactions. The SYK model can be exactly solved in the large N limit, where it is conjectured to be holographically dual to the Jackiw-Teitelboim model of gravity in two dimensions [107, 108, 109], and it can scramble as fast as a black hole in the low temperature limit [110]. The comparison to show the duality is summarized in Fig. 23 [110].

However, the randomness in the long range interactions is not necessary to produce fast scrambling. As Bentsen *et al.* have demonstrated in a recent paper, a non-disordered spin model describing sparsely connected spin-1/2 particles, can also be a fast scrambler [111]. Their proposal was motivated by the p-adic version of the anti-de Sitter/conformal field theory correspondence [112]. While their model is very elegant, its experimental realization can be very difficult when the system size becomes large. Thus, it is necessary to search for alternative approaches to realize fast scrambling without disordered interactions. Furthermore, all of these works raises a crucial question: are all fast scramblers holographically dual to quantum gravity?

In this chapter, we address this issue by proposing a fast scrambling many-body model, that is not inspired by holography. Our model essentially comprises two ingredients - a short range Ising interaction, and an infinite range XX interaction. Both of these features are crucial since short range interacting systems can not be fast scramblers [113], while uniform infinite range interactions can not induce quantum chaos [114]. Although our model is integrable in certain limits, we show that there is a large parameter regime, where the system exhibits fast scrambling. Furthermore, such a vanilla model may be easier to realize experimentally, even for large system sizes. Our results suggest that an appropriate combination of short and long range interactions can lead to fast scrambling.

We study information scrambling by studying the dynamics of an out-of-time ordered correlator (OTOC). In quantum chaotic systems, the growth of the OTOC at early times is exponential ($\sim e^{\lambda t}$), where λ is bounded ($\lambda \leq 2\pi k_B T/\hbar$)[89]. Moreover, the fast scrambling conjecture states that the time it takes for local information be thoroughly scrambled in a

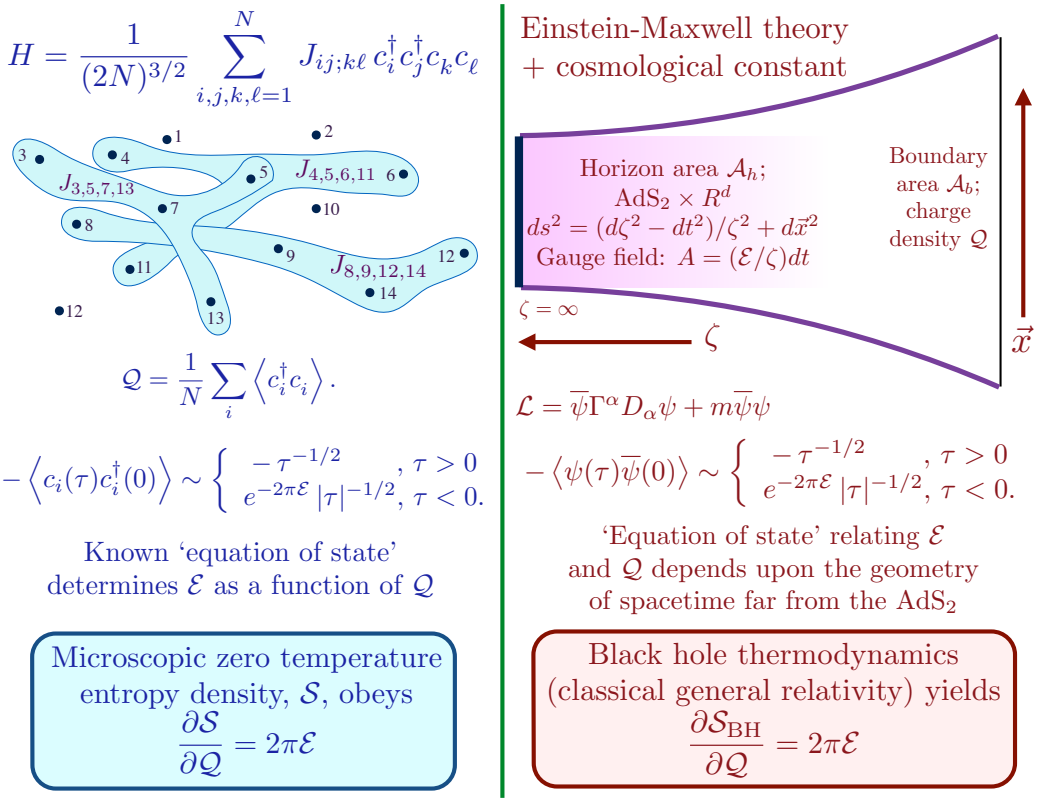

Figure 23: Summary of the properties of the SYK model and planar charged black holes at $T = 0$. The spatial co-ordinate $\vec{x}$ has d dimensions. The fermion mass m has to be adjusted to obtain the displayed power-law. The spectral asymmetry parameter $\mathcal{E}$ appears in the fermion correlators and in the AdS_2 electric field. A key observation in the holographic framework is that $\mathcal{E}$, now related to the electric field, obeys an important identity which follows from the laws of black hole thermodynamics, where $\mathcal{S}_{\rm BH}$ is the Bekenstein-Hawking entropy densiy of the AdS_2 horizon.

N body quantum system obeys a lower bound ($t \geq \log(N)/\lambda$) [87]. We identify a large parameter regime where our model behaves as a fast scrambler. We also find that in this regime, our model is non-integrable, and the entanglement entropy grows very fast.

6.1 Model

We study a one dimensional spin chain with N sites described by the following Hamiltonian:

$$H = \sum_{i=1}^{N} \left(\sigma_i^z \sigma_{i+1}^z + J \sum_{j>i} (\sigma_i^+ \sigma_j^- + \sigma_i^- \sigma_j^+) \right), \tag{6.2}$$

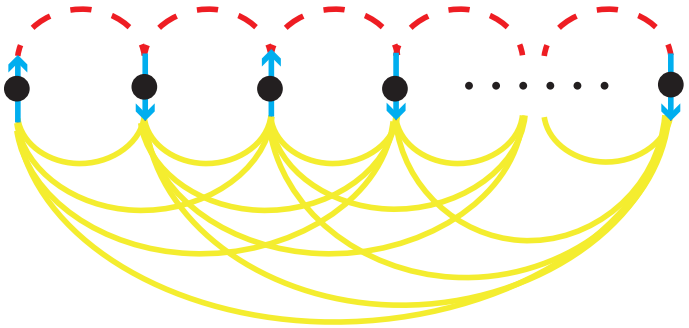

Figure 24: Schematic representation of the model: The model in Eq. (7.1) is characterized by a nearest neighbor Ising coupling and an infinite range XX coupling.

where $\sigma_i^{\pm} = \frac{1}{\sqrt{2}}(\sigma_i^x \pm i\sigma_i^y)$ and σ_i^{γ} is the standard Pauli matrix at lattice site i. A schematic of this model is shown in Fig. 24. In accordance with realistic experimental realizations of the all-to-all interaction, we do not rescale J by $1/N$. We note that this spin chain can not exhibit fast scrambling, when J is rescaled by $1/N$ [115]. Two other recent studies on related spin models have reached a similar conclusion [116, 117]. When $J \to \infty$, this model reduces to a form of the Lipkin-Meshkov-Glick model, and it is mean field solvable in the thermodynamic limit [118, 119]. On the other hand, when $J \to 0$, the model is the exactly solvable Ising model [120]. Intriguingly, between these two extreme limits, this model can

exhibit non-integrability - an essential criterion for fast scrambling [115]. In the remainder of the paper, we focus on the $J \sim O(1)$ regime, where the spin chain is characterized by Wigner-Dyson level statistics, and the system exhibits chaotic dynamics.

While cousins of our model have been studied extensively [121, 122, 123, 124, 125, 126, 127], to the best of our knowledge, neither the equilibrium phase diagram, nor the non-equilibrium dynamics of this precise model has been studied before. Consequently, we discover a trove of rich non-equilibrium physics that arises from the interplay of nearest neighbor and infinite range interactions. We use exact diagonalization to study this model with open boundary conditions. The total z-magnetization ($M_z = \sum_{i=1}^{N} \sigma_i^z$) is conserved during the time evolution of this system, and we examine the $M_z = 0$ sector in this work.

6.2 Out-of-time-order Correlations

Information scrambling is typically diagnosed by analyzing the dynamics of out-of-time ordered correlators (OTOCs). OTOCs capture the spreading of quantum information in a system by measuring operator growth. In particular, for two unitary and Hermitian operators A and B, the operator growth can be quantified by examining the expectation value of a squared commutator:

$$C(t) = \langle [A(t), B]^2 \rangle = 2 - 2\mathrm{Re}[\langle A(t)BA(t)B \rangle], \tag{6.3}$$

where $A(t) = e^{itH} A e^{-itH}$, and the OTOC is $\langle A(t)BA(t)B \rangle$. For our model, we take $A = \sigma_1^z$, $B = \sigma_j^z$, and we compute the following OTOC:

$$F(j,t) = \frac{1}{2}\left(1 + \mathrm{Re}[\langle \sigma_1^z(t)(t)\sigma_j^z\sigma_1^z(t)\sigma_j^z \rangle]\right). \tag{6.4}$$

We note that F is a bounded function ($0 \leq F \leq 1$). In quantum chaotic systems, $F(t)$ decays exponentially at early times i.e. $F(t) = 1 - \epsilon e^{\lambda_L t}$, where λ_L is analogous to the Lyapunov exponent. A salient characteristic of fast scramblers is that $F(j,t)$ spreads super-ballistically and starts deviating significantly from 1 on all sites, at a time $t^* \propto \log(N)$. In order to compare the properties of our model to other fast scramblers that have previously been

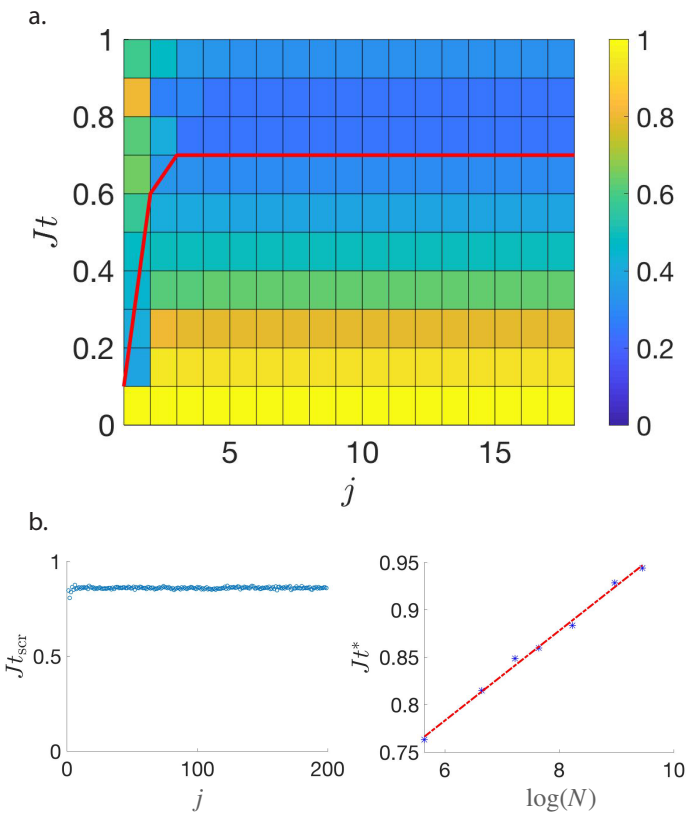

Figure 25: Scrambling of the infinite temperature state : a. Time evolution of the OTOC, $F(j,t)$ (defined in Eq. (6.4)) for a 18−site chain when $J = 1$. The red line represents the time at which the OTOC reaches its minimum value. The OTOC spreads super-ballistically in this parameter regime. This is a salient characteristic of a fast scrambler. b. Semiclassical numerics for the dynamics of the spin chain when $J = 1$. The left panel shows the time, $t_{\rm scr}$ at which the sensitivity $C_{cl}(j,t)$ (defined in Eq. (6.5)), reaches 1 on site j, when the chain length, $N = 200$. We conclude that this system exhibits super-ballistic spreading, since $t_{\rm scr}$ is (almost) constant for $j \gg 1$. The right panel shows the system size dependence of the scrambling time t^*, at which $C_{cl}(j,t)$ reaches 1 on all sites. We find that, $t^* \propto \log(N)$ - a characteristic signature of fast scrambling.

studied in the literature [21, 111, 128, 129], we compute $F(j,t)$ for the infinite temperature

state. Our results for a 18 site chain is shown in Fig. 25a. It is clear from these figures that super-ballistic spreading of the OTOC occurs in this system, when $J \sim 1$. As detailed in the supplementary material D, we can obtain an analytical understanding of this behavior using a short-time expansion [115].

While all the numerical results that we have discussed so far are exact, our study has been limited to small system sizes. However, in order to convincingly establish that out model is indeed a fast scrambler, we have to determine the dependence of t^* on N for $N \gg 1$. To overcome this limitation, we study the spin-S version of our model, in the $S \to \infty$ limit, where it can be analyzed semi-classically. Following Ref. [130], we compute the averaged sensitivity:

$$C_{\rm cl}(j,t) = \frac{1}{4S^2}\langle\left(\frac{dS_j^z(t)}{d\phi}\right)^2\rangle, \tag{6.5}$$

where ϕ is a small initial rotation of spin 1 about the z-axis, and the factor of $1/4$ has been introduced to establish correspondence with $F(j,t)$. This quantity can capture the sensitivity to initial conditions in classical systems, and it can be derived from Eq. (6.3) by substituting the commutator with appropriate Poisson brackets. In order to compute the infinite temperature OTOC, we evaluate Eq. (6.5) for an ensemble in which each spin is initially aligned in a random direction. We characterize the scrambling rate in this semi-classical limit by computing the $j-$dependence of the time, $t_{\rm scr}$ at which $C_{\rm cl}(j, t_{\rm scr})$ becomes significant (~ 1). As shown in Fig. 25b, we find that $t_{\rm scr}$ is (almost) constant for $j \gg 1$, thereby implying that this chain exhibits super-ballistic spreading. Furthermore, we systematically analyze the system size dependence of the scrambling time, and find that $C_{cl}(t^*)$ becomes significant (~ 1) on all sites at time $t^* \propto \log(N)$. These calculations confirm that our model can exhibit fast scrambling.

6.3 Quench Dynamics

While the infinite temperature OTOC dynamics provides compelling evidence for fast scrambling in our model, preparing this state in an experiment can be challenging. To alleviate this concern, we also study quench dynamics of this system for different initial

states in the $M_z = 0$ sector. In particular, we examine the OTOCs for unentangled product states of the form $|z_1; z_2; z_3 \dots z_L\rangle$, where z_i is a spin polarized along the z-direction at site i ($\uparrow$ or $\downarrow$). Motivated by experiments on cold atoms, we study the time evolution of the system, when it is initially prepared in the classical Néel initial state ($|\uparrow\downarrow\uparrow\downarrow \dots \uparrow\downarrow\uparrow\downarrow\rangle$). As shown in Fig. 26, we find that signatures of fast scrambling can be seen in the quench dynamics. We observe qualitatively similar behavior for other initial states [115]. We note that the infinite temperature results imply that fast scrambling can be observed for any typical initial state [117].

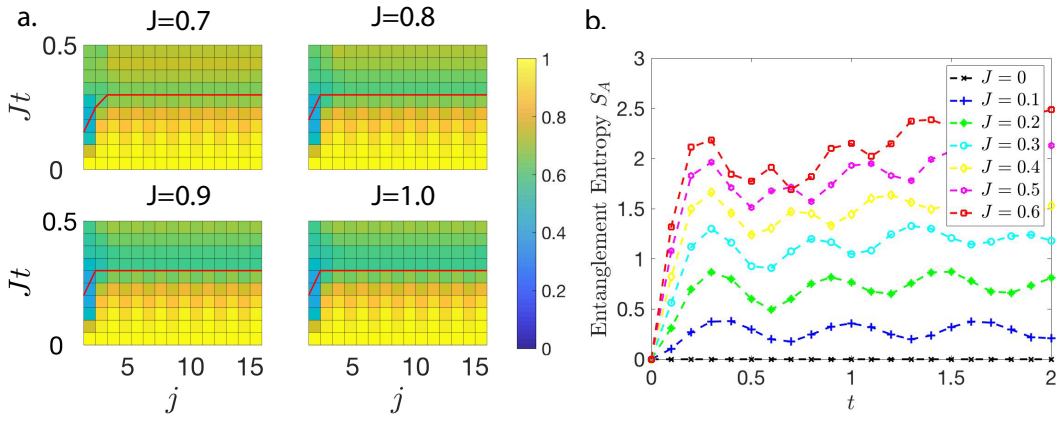

Figure 26: Quench dynamics for the classical Néel state: a. The OTOC for different long range interactions, J. The red line is the time at which the OTOC reaches its minimal value. Similar to the infinite temperature case, the OTOC spreads super-ballistically. b. The dynamics of the half-chain entanglement entropy, for different long range interactions, J. This model is identical to the Ising model when $J = 0$, and the entropy does not grow. As we increase J, the entropy grows faster and saturates to higher values. This result is consistent with the behavior of the OTOC.

A complementary approach to study information propagation in a quantum many-body system is to examine the growth of the half-chain entanglement entropy, $S_A = \mathrm{Tr}[\rho_L \log(\rho_L)]$, where $\rho_L = \mathrm{Tr}_R(|\psi\rangle\langle\psi|)$ is the reduced density matrix obtained by tracing over the degrees of freedom of one half of the chain. As shown in Fig. 26b, we find that S_A grows faster and saturates to higher values as J increases. These results agree with our previous observation

that the system exhibits faster scrambling when the strength of the infinite range interaction increases, as long as the system remains non-integrable.

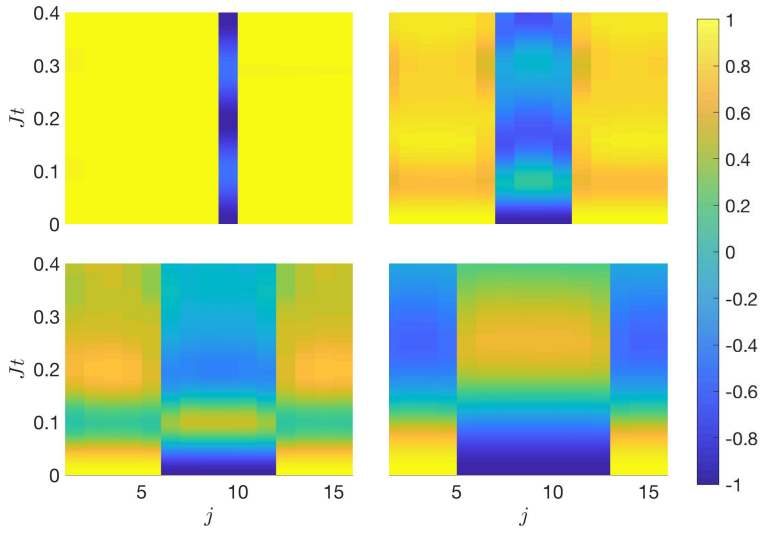

Figure 27: Quench dynamics for different magnetization sectors: Density plot for the local z-magnetization for initial states with different total magnetizations, when $J = 1$. The initial state has M spin downs clustered at the center of the chain, and $N - M$ spin-ups present symmetrically around this cluster. We find that there is a crossover from slow to fast scrambling, as the spin imbalance decreases.

Finally, we also explore the quench dynamics, when the total magnetization M_z is finite. In particular, we compute the localization magnetization, since this order parameter is accessible to experimental measurements. Furthermore, this quantity can be related to the recently proposed fidelity out of time order correlators, and can hence be used to quantify scrambling [131]. We note that in the one-magnon sector, i.e. when there is one spin-up (spin-down), and $N - 1$ spin-down (spin-up) in the initial state, then the system is integrable, and the system exhibits localized dynamics. This localization can be traced to the presence of localized eigenstates of the form: $|\psi\rangle = |\phi_i\rangle + \frac{1}{N-1}\sum_{j\neq i}|\phi_j\rangle$, where $|\phi_i\rangle = |\uparrow\uparrow \ldots \uparrow_{i-1}\downarrow_i\uparrow_{i+1} \ldots \uparrow\uparrow\rangle$ [132]. While this model is integrable in the one-magnon sector, and it can be non-integrable for a large parameter regime in the $N/2$ magnon sector. We carefully study the crossover from slow to fast scrambling can be seen as $|M_z|$ decreases.

As shown in Fig. 27, we find that the fastest scrambling occurs when $M_z = 0$.

6.4 Experimental Realizations

The most natural way to realize our model is to couple an Ising spin chain to a single mode cavity [133]. By adiabatically eliminating the cavity degrees of freedom in the dispersive limit, we can obtain an effective infinite range coupling of the form described in Eq. (7.1) [134, 135, 136]. A promising scheme to realize our spin model using Rydberg dressed atoms in an optical cavity has been proposed in Ref. [137]. As detailed in the supplementary material D, implementing this scheme is within the reach of current experiments. Another feasible route is to place a trapped ion crystal in the cavity [138, 139]. Alternatively, it is possible to engineer this model by employing photon-mediated interaction between spins trapped in a photonic crystal waveguide [140], or by performing digital-analog simulations with trapped ions [141]. Several experimental protocols have been proposed to measure OTOCs in the experimental platforms described above. The infinite temperature OTOC can be determined by examining statistical correlations between measurements on randomized initial states [142]. Furthermore, some recent investigations have shown that it is possible to probe the scrambling dynamics after a quantum quench by measuring two point correlation functions [143, 144]. Alternatively, interferometric techniques can also be used to measure OTOCs in different experimental platforms.

6.5 Comparison with Other Fast Scramblers

Before we conclude this paper, it is instructive to compare our model to other fast scramblers studied in the literature. As illustrated in Fig. 2, the scrambling time in our model is finite at infinite temperature. This feature is shared by several other fast scramblers, including most noticeably the SYK model, which describes N Majorana fermions interacting via disordered global interactions drawn from a gaussian distribution of width $\mathcal{J}/N^{3/2}$. The

scrambling time in this model shows a logarithmic dependence on the system size: $t^* \sim \log(N)/\mathcal{J}$ [145, 146]. It is worth noting, there are some quantum chaotic systems, where the scrambling time is much faster (~ 0) and N-independent [129]. A particularly striking example of this is a model of N spins interacting with a central spin on a star like graph, where $t^* \sim 0$, even at finite temperatures [147]; this is the fastest scrambler found till date.

We note that after our preprint was posted on the arXiv, there appeared two other papers exploring fast scrambling in related spin models. Belyansky *et al.* have demonstrated super-ballistic spreading of OTOCs in a spin model similar to ours (with the infinite range interaction is given by $J/\sqrt{N}$). Furthermore, they have argued that the infinite temperature Lyapunov exponent is finite in these systems and $t^* \sim 3/2 \log(N)/J^2$ [116]. In a similar vein, Yin and Lucas have studied a family of non-integrable spin chains with two ingredients: (1) a global interaction rescaled by $1/N^\delta$ and (2) a time dependent magnetic field that ensures locally chaotic dynamics. They have derived a lower bound on the scrambling time in these models: $t^* > N^{\delta-1/2}$; fast scrambling occurs only when $\delta \leq 1/2$ [117]. Thus, akin to our model, fast scrambling and extensivity of the total energy (which requires $\delta > 1$) can not occur simultaneously in these systems. Intriguingly, the scrambling rate can increase dramatically in these models (and even become N-independent), when the infinite range couplings are strongly time-dependent.

6.6 Summary and Outlook

The paradigm of fast scrambling is of fundamental importance in understanding the dynamics of highly chaotic quantum systems. Observing fast scrambling is widely considered to be an important milestone towards exploring aspects of quantum gravity in the laboratory [148, 149, 150]. Furthermore, fast scramblers can be harnessed for performing quantum information processing tasks, and is thus of great practical use [151, 152]. An extremely important feature of our work is that unlike other proposals studied in the literature, our model is not motivated by holography. This leads us to conjecture that fast scrambling can arise in non-holographic quantum matter. A rigorous proof of this conjecture can lead to

the discovery of precise probes for distinguishing holographic and non-holographic quantum models, thereby shedding light on some fundamental questions in non-equilibrium quantum dynamics. Future work can examine other models with both short and long range interactions, and determine general conditions under which quantum many-body systems can exhibit fast scrambling.

7.0 Quantum Phases of the Heisenberg Spin Chain with Competing Short and Long Range Interactions

In recent years, there has been a lot of interest in exploring the kaleidoscope of quantum phases that arise in quantum many-body systems with cavity induced long range interactions [153, 154, 155, 156, 157, 158, 159]. These systems provide a promising platform for realizing quantum spin liquids [160], supersolids [161, 126, 162], exotic superconductors [163, 164, 165], charge density waves [166], time crystals [167, 168], chaotic dynamical phases [124, 123], and even topological states of matter [169]. Moreover, cavity mediated interactions can be harnessed to explore many-body chaos [114, 111, 78, 82, 131] and dynamical quantum phase transitions [170, 171].

In the previous chapter, we have demonstrated that a one dimensional Ising spin chain coupled to a single mode cavity can exhibit fast scrambling; this highly chaotic dynamics originates from the interplay of short and long range interactions [15]. Concurrently, other groups have also shown that competing short and long range interactions can induce fast scrambling [116, 117]. In this context, it is worth noting that even though scrambling is an inherently non-equilibrium phenomenon, several fast scrambling many-body models host a rich array of quantum phases at equilibrium [102, 172, 173, 174, 175]. This observation naturally leads to the following question: what are the ground state phases of this new class of cavity induced fast scramblers?

In this chapter, we address this question by investigating the quantum phases of an one-dimensional spin chain composed of two ingredients - a nearest neighbor XXZ interaction and an infinite range XX interaction. A schematic representation of our model is shown in Fig. 28. This model describes a Heisenberg XXZ spin chain coupled to a single mode cavity in the "bad cavity" limit. By employing an analytical spin-wave analysis as well as numerical Density Matrix Renormalization Group (DMRG) computations, we demonstrate that this system exhibits three different phases: (a) a long-range ordered Ising ferromagnetic phase, (b) a quasi-long range ordered critical phase, and (c) a long-range ordered $U(1)$ symmetry breaking XY phase. While the first two phases can be realized in the short range interacting

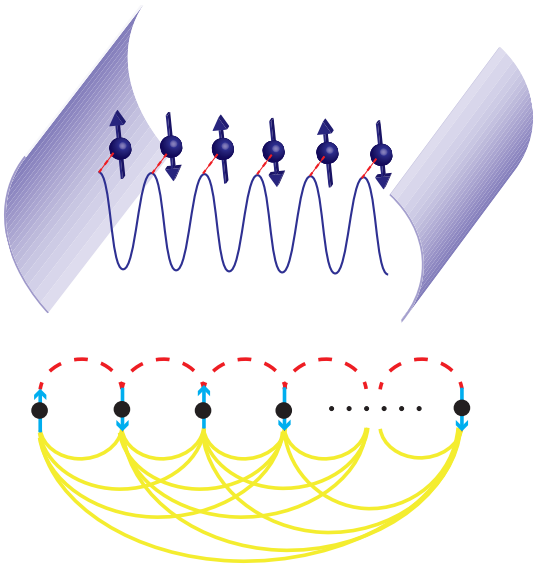

Figure 28: Schematic representation of the model: The model in Eq. (7.1) is characterized by a nearest neighbor XXZ coupling and an infinite range XX coupling. This model describes a XXZ spin chain is coupled to a single mode cavity.

Heisenberg model, the cavity induced interaction leads to the realization of the third phase. We demonstrate that these phases can be distinguished by their entanglement entropy; in particular, phases (b) and (c) violate the area law logarithmically and can be associated with an effective central charge. The effective central charge distinguishes phase (b) from phase (c).

7.1 Model

We study a one dimensional spin chain with N sites described by the Hamiltonian, $H = H_{XXZ} + H_{\rm LMG}$, where

$$\begin{aligned} H_{XXZ} &= -\frac{1}{4}\sum_{i=1}^{N}\left(\sigma_i^z\sigma_{i+1}^z + \alpha(\sigma_i^x\sigma_{i+1}^x + \sigma_i^y\sigma_{i+1}^y)\right) \\ H_{\rm LMG} &= \frac{J}{4N}\sum_{i=1}^{N}\sum_{j>i}\left(\sigma_i^x\sigma_j^x + \sigma_i^y\sigma_j^y\right) \end{aligned} \tag{7.1}$$

where σ_i^γ is the standard Pauli matrix at lattice site i. We have rescaled the infinite range interaction by $1/N$ to ensure extensivity of the total energy. We note that this model has a $U(1)\times\mathbb{Z}_2$ symmetry. The chain is in the Ising ferromagnetic phase when the $\mathbb{Z}_2$ symmetry is broken; when the continuous $U(1)$ symmetry is broken on the other hand, the system is in the XY phase [176].

When $J\to 0$, the model is the exactly solvable by the Bethe ansatz [177, 178], and in this case there are two possible phases: the Ising ferromagnetic phase (when $\alpha < 1$) and a quasi-long range ordered critical phase, known as the Tomonaga-Luttinger Liquid (TLL) (when $\alpha \geq 1$) [179]. We note that the Mermin-Wagner theorem forbids the existence of a truly long range ordered phase with only short range interactions [180, 181].

The ground state of this system can also be exactly determined in the $J\to\infty$ limit, when the model reduces to mean-field solvable Lipkin-Meshkov-Glick (LMG) model [182, 118, 119]. In this case, the ground state of the system is in the XY phase [183]. In the next section, we explore the phase diagram of this model when J is finite. This is precisely the regime, where the model is non-integrable and its out-of-equilibrium dynamics is chaotic.

7.2 Spin Wave Analysis

In this section, we employ spin-wave analysis to explore the phase diagram of the model. It is well known that the ground state spontaneously breaks the $\mathbb{Z}_2$ symmetry, when $\alpha\to 0$

and $J \to 0$. In order to determine the phase boundary of this Ising ferromagnetic state, we define the vacuum state to be:

$$|\psi\rangle_{\rm FM} = |\uparrow\uparrow\uparrow\uparrow \ldots \uparrow\uparrow\uparrow\uparrow\rangle, \tag{7.2}$$

and apply the Holstein-Primakoff transformation to map the spin excitations to bosons: $S_j^- = \frac{1}{2}(\sigma_j^x - i\sigma_j^y) = \left(\sqrt{1 - a_j^\dagger a_j}\right) a_j; S_j^+ = \frac{1}{2}(\sigma_j^x + i\sigma_j^y) = a_j^\dagger \left(\sqrt{1 - a_j^\dagger a_j}\right); S_j^z = (\frac{1}{2} - a_j^\dagger a_j)$ [184]. In the weak excitation regime, $\langle a^\dagger a\rangle \ll 1$, and the Hamiltonian describing these spin waves is given by:

$$\begin{aligned} H_{FM} &= \sum_i \Big((a_i^\dagger a_i + a_{i+1}^\dagger a_{i+1}) - \alpha(a_i^\dagger a_{i+1} + a_{i+1}^\dagger a_i)\Big) \\ &+ \frac{J}{N}\sum_i \sum_{j>i} \Big(a_i^\dagger a_j + a_j^\dagger a_i)\Big) \end{aligned} \tag{7.3}$$

Assuming periodic boundary conditions, we can express the spin-wave Hamiltonian can be in the following form:

$$H_{FM} = \sum_k \omega_k a_k^\dagger a_k, \tag{7.4}$$

where

$$\omega_k = 1 - \alpha\cos(k) + \frac{J}{N}\sum_r \cos(kr). \tag{7.5}$$

If $\min[\omega_k] > 0$, then the ground state of the system is the z-polarized state in Eq. 7.2. On the other hand, when $\min[\omega_k] < 0$, then the ground state is no longer z-polarized. From this expression, it is clear that the ground state is ferromagnetic when $\alpha = 1$ (for $J \geq 0$), and $\alpha = 1 + J$ (for $J \leq 0$).

The Holstein-Primakoff transformation can also be employed to study the stability of the $U(1)$-symmetry breaking phase. In this case, we define the vacuum state to be spin polarized along the $+x$ direction:

$$|\psi\rangle_{\rm XY} = |\rightarrow\rightarrow\rightarrow\rightarrow \ldots \rightarrow\rightarrow\rightarrow\rightarrow\rangle, \tag{7.6}$$

The Holstein-Primakoff mapping in this case is $S_i^x = (\frac{1}{2} - a_i^\dagger a_i)$; $S_i^y \approx a_i^\dagger + a_i$; $S_i^z \approx (a_i^\dagger - a_i)/i$. The Hamiltonian describing the spin-wave excitations in this case is:

$$H_{\rm sw} = \sum_{k=-N/2}^{N/2} \omega_k (a_k^\dagger a_k + a_{-k} a_{-k}^\dagger) + \mu_k (a_k^\dagger a_{-k}^\dagger + a_k a_{-k}); \tag{7.7}$$

where,

$$\omega_k = (\alpha - \frac{J}{2}) - \frac{1+\alpha}{2}\cos(\frac{2\pi k}{N}) + \frac{J}{2N}\sum_{r=1}^{N/2}\cos(\frac{2\pi k}{N} r) \tag{7.8}$$

$$\mu_k = \frac{1-\alpha}{2}\cos(\frac{2\pi k}{N}) - \frac{J}{2N}\sum_{r=1}^{N/2}\cos(\frac{2\pi k}{N} r) \tag{7.9}$$

where $a_k = \frac{1}{\sqrt{N}}\sum_j \exp(i2\pi jk/N) a_j$. $H_{\rm sw}$ can be diagonalized by a Bogoliubov transformation [185]. In this case, the Bogoliubov quasiparticles are composed of both particles and holes and the ground state of the spin chain has spin excitations. The density of these excitations is given by:

$$\begin{aligned} \langle a_i^\dagger a_i \rangle &= \lim_{N\to\infty} \frac{1}{2N}\sum_{k\neq 0}([1-\mu_k^2/\omega_k^2]^{-1/2} - 1) \\ &= \frac{1}{4\pi}\int_{-\pi}^{\pi} dq \left([1-\mu(q)^2/\omega(q)^2]^{-1/2} - 1\right) \\ &= \frac{1}{4\pi}\int_{-\pi}^{\pi} dq\, \mathcal{I}(q) \end{aligned} \tag{7.10}$$

By expanding the integrand around $q = 0$, we find that $\mathcal{I}(q) \propto 1/|q|$, when $J = 0$. And more generally, $\mathcal{I}(q) \propto 1/\sqrt{(J-\alpha q^2)(1-\alpha+(q^2-J)/2)}$. This implies that in the absence of the infinite range interactions, $\langle a_i^\dagger a_i \rangle \sim \ln(N)$ and the long range order is destroyed in the thermodynamic limit. On the other hand, $\langle a_i^\dagger a_i \rangle$ does not diverge and $U(1)$ symmetry breaking occurs, when $J \neq 0$. Our results are summarized in Fig. 29. In the next section, we compliment our spin wave analysis results with numerical density matrix renormalization group calculation of the ground state phase diagram.

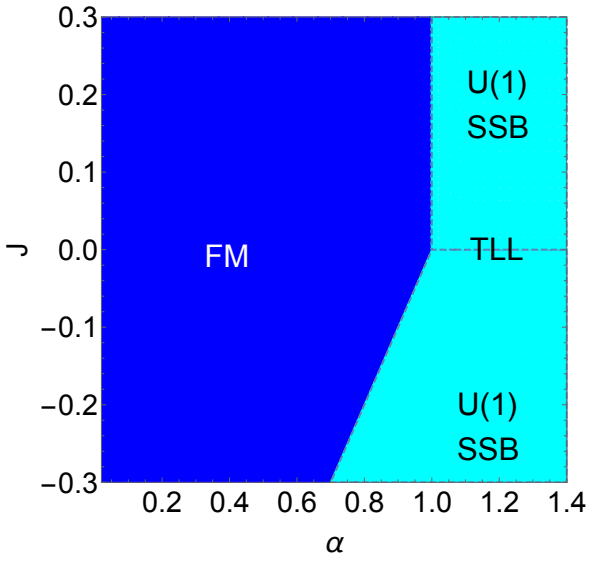

Figure 29: Phase diagram from dpin-wave analysis: The spin-wave analysis presented in section III reveals that there are three phases in this spin-chain: (a) A z-polarized ferromagnetic phase, (b) a quasi-long range ordered Tomonaga Luttinger liquid (TLL), and (c) a long-range ordered XY-like phase that spontaneously breaks the $U(1)$ symmetry of this model.

7.3 Density Matrix Renormalization Group Simulations

The density matrix renormalization group is a powerful tool to diagnose the equilibrium phases and out-of-equilibrium dynamics of one-dimensional and quasi-one-dimensional quantum systems [186, 187, 188]. We now proceed to to determine the phase diagram of our model using the DMRG algorithm. In this method, we employ a Matrix Product State ansatz to represent the ground state [189, 190], and ensure that the algorithm converges globally with a truncation error less than 10^{-6}. The short range part of the Hamiltonian (H_{XXZ}) has already been extensively studied with this method [187]. For the long range part, we represent H_{LMG} as a sum of Matrix Product Operators; this choice avoids systematic errors introduced by other schemes [191]. Our codes are mainly based on *tensors.net*

library [192].

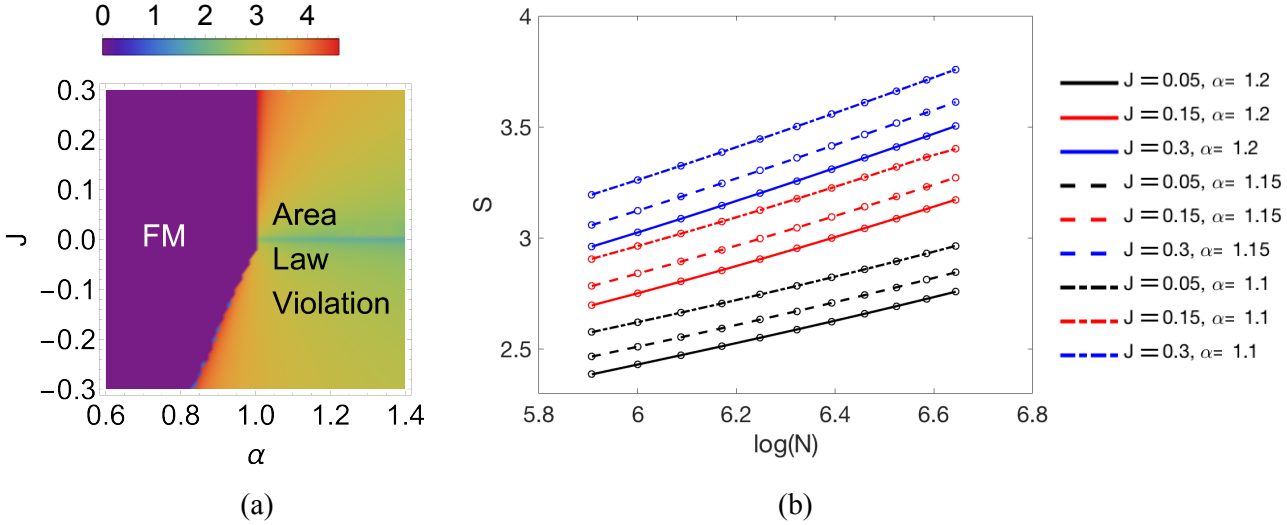

Figure 30: Ground state entanglement entropy: The entanglement entropy of the ground state is 0, when the spins are polarized along the z-direction and the correlations are ferromagnetic in nature. The entanglement entropy violates the area law logarithmically, when the correlations are XY-like. Panel (a) shows the density plot for the half chain entanglement entropy, defined in Eq. 7.11 for a 100 site chain. Panel (b) shows the dependence of the entanglement entropy on the system size, when the correlations are XY-like.

The ground state entanglement entropy, provides a powerful tool to numerically diagnose the phases of long range interacting systems [193, 194, 195]. In particular, the $\mathbb{Z}_2$-symmetry broken ferromagnetic phase is characterized by an area law entanglement entropy, while ground states with XY-like order exhibit violation of the area law. We compute the entanglement entropy, S, defined as:

$$S = \mathrm{Tr}\rho_B \log(\rho_B), \tag{7.11}$$

where ρ_B is the reduced density matrix of the right (left) half of the chain, and it is obtained by tracing over the degrees of freedom of the left (right) half of the chain. As shown in Fig. 30(a), $S = 0$, when the spins are z-polarized and the spin chain is in the ferromagnetic phase. On the other hand, the entropy is finite, when the ground state is XY-like. Our results are shown in Fig. 30(a).

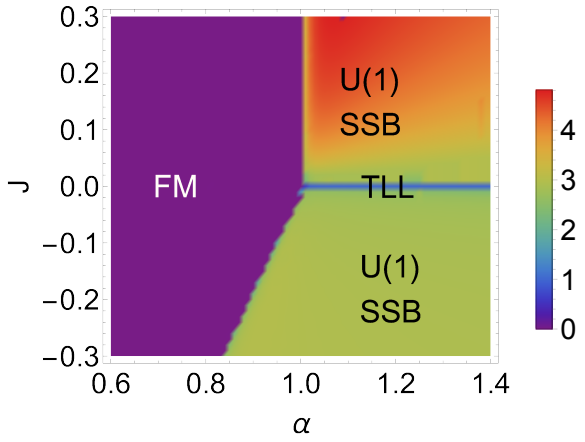

Figure 31: Phase diagram from the effective central charge: The density plot for the effective central charge, c (defined in Eq. 7.12) shows that there are three phases: (a) A ferromagnetic phase characterized by $c = 0$ (b) the critical Tomonaga Luttinger Liquid characterized by $c = 1$ and (c) A true $U(1)$ spontaneous symmetry breaking (SSB) phase characterized by $c > 1$. The phase diagram obtained from the central charge qualitatively matches the results from the spin wave analysis.

It is evident from Fig. 30(b) that in the XY-like phase, the entanglement entropy violates the area law logarithmically. Employing an analogy with critical systems [196], we can define an effective central charge, c using the following relation:

$$S = \frac{c}{6} \log(L) \tag{7.12}$$

The central charge, c is 0 for the Ising ferromagnetic phase and it is 1 for the critical Tomonaga-Luttinger liquid phase. Furthermore, in the long range ordered $U(1)$ symmetry breaking XY phase, $c > 1$ [197, 176, 191]. As shown in Fig. 31, we find that the cavity mediated long range interactions can lead to the spontaneous breaking of a continuous $U(1)$ symmetry for a large parameter regime. Furthermore, our results demonstrate that even an infinitesimally weak coupling between the short range interacting spin chain and the optical cavity is sufficient to induce long range XY order in the spin chain, thereby providing a route to circumvent the Mermin-Wagner theorem.

8.0 Conclusions

In this chapter, I will conclude the researches in my PhD study. In Chapter 4, we study the mean-field ground state of a d-wave interacting Bose gas, and it is found that there are three superfluid phases: atomic, molecular and atomic-molecular superfluid phases. What is most surprising is that unlike the p-wave case [42, 9, 43], we find the atomic superfluid does not carry finite momentum. Furthermore, we study the low-energy excitation spectrum above the superfluid phases. Our work provides a basic reference for the experiment on degenerate d-wave interacting Bose gas.

In Chapter 5, we study the quantum fluctuation correction to the ground states of a p-wave interacting Bose gas. Beginning with the mean-field analysis of the ground states, it is found that the ground states can be divided into three typical phases for different detunings of molecule channel, i.e. the ASF, AMSF and MSF phases, where particles are condensed into only the atomic, both the molecular and atomic, and only the molecular channels, respectively. Particularly, we find the ground state is unstable in phase AMSF. The instability of the ground state in the phase AMSF also manifests itself in the emergence of imaginary long-wavelength Bogoliubov excitation modes. Furthermore, we calculate the LHY correction with the Bogoliubov excitations. We find the LHY correction can stabilize the ground state in the mean-field-unstable regime. That means that the p-wave interacting Bose gas is self-stabilized at a certain density. Finally, we construct an effective Hamiltonian to characterize the ground state of a finite system. By solving the corresponding GP equation, we find self-stabilized quantum-droplet solutions. Unlike the s-wave case, the quantum droplet is anisotropic and carries finite momentums because the spatial rotation and the time-reversal symmetries are spontaneously broken. Although only the interspecies p-wave interaction is considered here, our results could be extended into the case with weak background s-wave interactions and may be observed in systems like $^{85}Rb-^{87}Rb$ Bose mixture [64, 65].

In Chapter 6, we have demonstrated a novel route for creating a fast scrambler in an experimentally realizable spin model. Our proposal exploits the interplay of short and long range interactions to make the system highly chaotic. By studying the infinite temperature

OTOC of the system, using both exact diagonalization, and a semi-classical approximation technique, we have first demonstrated that the system exhibits fast scrambling. Next, we have examined the quench dynamics of the system, when it is initially prepared in the classical Néel state, and found that the OTOC and the half chain entanglement entropy grows very fast. Similar results are found for other non-entangled initial states when the total magnetization, M_z is 0. We have systematically explored how the scrambling rate depends on the total magnetization, and found that the system exhibits a crossover from slow to fast scrambling as the total magnetization decreases from $|M_z| = N$ (i.e. the fully polarized state) to $M_z = 0$. Finally, we have proposed possible experimental realizations of our model. Thus, our work presents a rare example of a many-body model where the fast scrambling is not induced by random long range interactions, and provides a possible solution to the critical outstanding challenge of observing fast scrambling experimentally.

In Chapter 7, we have examined the ground state phases of a Heisenberg spin chain with competing short and long range interactions. Our results demonstrate that cavity mediated long range interactions can lead to the spontaneous breaking of the continuous $U(1)$ symmetry and a consequent violation of the area law. In the future it would be interesting to extend our study to spin-1 systems and examine whether Haldane-like topological phases can arise in those systems.

Appendix A p-wave Model Order Parameter Structure

Here we discuss two collinear states falling into two universality classes, represented by the FF-like [48] and the LO-like [49] single harmonic forms [9],

$$\Psi_\sigma^{\rm FF} = \Psi_{\sigma,\boldsymbol{Q}_\sigma} e^{i\boldsymbol{Q}_\sigma\cdot\boldsymbol{r}}, \tag{A.1}$$

$$\Psi_\sigma^{\rm LO} = \Psi_{\sigma,\boldsymbol{Q}} e^{i\boldsymbol{Q}\cdot\boldsymbol{r}} + \Psi_{\sigma,-\boldsymbol{Q}} e^{-i\boldsymbol{Q}\cdot\boldsymbol{r}}. \tag{A.2}$$

In the FF-like (LO-like) state each species is characterized by a single $\boldsymbol{Q}$ (double $\pm\boldsymbol{Q}$) momentum, exhibiting a uniform (periodic) atomic density. We reexpress the mean-field energy densities for FF and LO in terms of the corresponding eigenmodes, $\Psi_\pm^{\pm Q}$, the latter involving two ($\pm Q$) critical modes,

$$\mathcal{E}_{\rm FF} = (\varepsilon_{\boldsymbol{Q}} - |\Delta_{\boldsymbol{Q}}|)|\Psi_-^{Q}|^2 + \frac{1}{2}\lambda|\Psi_-^{Q}|^4, \tag{A.3}$$

$$\begin{aligned}\mathcal{E}_{\rm LO} = {} & (\varepsilon_{\boldsymbol{Q}} - |\Delta_{\boldsymbol{Q}}|)(|\Psi_-^{Q}|^2 + |\Psi_-^{-Q}|^2) \\ & + \frac{1}{2}\lambda(|\Psi_-^{Q}|^2 + |\Psi_-^{-Q}|^2)^2 + \lambda'|\Psi_-^{Q}|^2|\Psi_-^{-Q}|^2,\end{aligned} \tag{A.4}$$

where $\lambda = \frac{1}{4}(\lambda_1 + \lambda_2 + 2\lambda_{12})$ and $\lambda' = \frac{1}{4}(\lambda_1 + \lambda_2 - 2\lambda_{12})$.

These free energies thus show that the energetically preferred form of the AMSF state is determined by the coefficient λ' of last term in Eq. (A.4). For $\lambda' > 0$, that is, $\lambda_1 + \lambda_2 > 2\lambda_{12}$, the single Q FF-like state is selected. On the other hand, for $\lambda' < 0$, that is, $\lambda_1 + \lambda_2 < 2\lambda_{12}$, it is the LO-like state that has the lowest energy. Combining the above requirement on λ' for the stability of the LO-like state with the condition for two-species miscibility, $\lambda_1\lambda_2 > \lambda_{12}^2$, we find an inequality,

$$\frac{\lambda_1 + \lambda_2}{2} < \lambda_{12} < \sqrt{\lambda_1\lambda_2} \tag{A.5}$$

which for positive couplings λ_i can be shown to have a zero range of stability. Thus, as advertised, within mean-field approximation it is the single Q FF-like AMSF state that is always energetically selected.

Appendix B FF-like and LO-like Atomic Order Parameters Comparison

The FF-like [48] and LO-like [49] forms of order parameters are respectively given by

$$\Psi_\sigma^{FF} = \Psi_{\sigma,\mathbf{Q}_\sigma} e^{i\mathbf{Q}_\sigma\cdot\mathbf{r}},$$

$$\Psi_\sigma^{LO} = \Psi_{\sigma,\mathbf{Q}} e^{i\mathbf{Q}\cdot\mathbf{r}} + \Psi_{\sigma,-\mathbf{Q}} e^{-i\mathbf{Q}\cdot\mathbf{r}},$$

where $\Psi_{\sigma,\mathbf{Q}} = \Psi_{\sigma,-\mathbf{Q}}$. We will prove in the following context that FF-like form is energetically preferred in a low energy regime.

In LO form, the free energy density is

$$f = F/V = f_M + f_{\mathbf{Q}},$$

where

$$f_M = \sum_{m=-2}^{2} -\mu_M|\Phi_m|^2 + \sum_{m,n=-2}^{2} \frac{g_0}{2}(\Phi_m^*\Phi_m)(\Phi_n^*\Phi_n),$$

$$\begin{aligned} f_{\mathbf{Q}} = {} & \frac{1}{V}\int_V d^3r \sum_{\sigma=1,2} 4\varepsilon_{\mathbf{Q}}(|\Psi_{\sigma,\mathbf{Q}}|^2\cos^2(\mathbf{Q}\cdot\mathbf{r})) \\ & -[\Delta^*(\Psi_{1,\mathbf{Q}}\Psi_{2,-\mathbf{Q}} + \Psi_{1,-\mathbf{Q}}\Psi_{2,\mathbf{Q}}) + c.c.] \\ & + \sum_{\sigma,\sigma'=1,2} \frac{\lambda_{\sigma,\sigma'}}{2}|\Psi_\sigma|^2|\Psi_{\sigma'}|^2, \end{aligned}$$

and $\varepsilon_{\mathbf{Q}} = \frac{Q^2}{2m} - \mu + g_{\mathrm{AM}}n_M, \Delta = \sum_{m=-2}^{2} \overline{g}\sqrt{4\pi}Q^2\Phi_m Y_2^m(\hat{\mathbf{Q}})$. For the quadratic part, we rewrite it in the matrix formula,

$$f_{\mathbf{Q}}^0 = \frac{1}{V}\int_V d^3r \begin{bmatrix} \Psi_{1,\mathbf{Q}}^* \\ \Psi_{1,-\mathbf{Q}} \\ \Psi_{2,\mathbf{Q}}^* \\ \Psi_{2,-\mathbf{Q}} \end{bmatrix}^T \begin{bmatrix} 2\varepsilon_{\mathbf{Q}}\cos^2(\mathbf{Q}\cdot\mathbf{r}) & 0 & 0 & -\Delta_{\mathbf{Q}} \\ 0 & 2\varepsilon_{\mathbf{Q}}\cos^2(\mathbf{Q}\cdot\mathbf{r}) & -\Delta_{\mathbf{Q}}^* & 0 \\ 0 & -\Delta_{\mathbf{Q}} & 2\varepsilon_{\mathbf{Q}}\cos^2(\mathbf{Q}\cdot\mathbf{r}) & 0 \\ -\Delta_{\mathbf{Q}}^* & 0 & 0 & 2\varepsilon_{\mathbf{Q}}\cos^2(\mathbf{Q}\cdot\mathbf{r}) \end{bmatrix} \begin{bmatrix} \Psi_{1,\mathbf{Q}} \\ \Psi_{1,-\mathbf{Q}}^* \\ \Psi_{2,\mathbf{Q}} \\ \Psi_{2,-\mathbf{Q}}^* \end{bmatrix},$$

We diagonalize the quadratic Hamiltonian, obtaining the eigenvector matrix and eigenvalues,

$$U = \frac{1}{\sqrt{2}} \begin{bmatrix} e^{-i\theta_0} & 0 & -e^{-i\theta_0} & 0 \\ 0 & e^{i\theta_0} & 0 & -e^{i\theta_0} \\ 0 & 1 & 0 & 1 \\ 1 & 0 & 1 & 0 \end{bmatrix},$$

$$V=\begin{bmatrix} 2\varepsilon_{\mathbf{Q}}\cos^2(\mathbf{Q}\cdot\mathbf{r})-|\Delta_{\mathbf{Q}}| & 0 & 0 & 0 \\ 0 & 2\varepsilon_{\mathbf{Q}}\cos^2(\mathbf{Q}\cdot\mathbf{r})-|\Delta_{\mathbf{Q}}| & 0 & 0 \\ 0 & 0 & 2\varepsilon_{\mathbf{Q}}\cos^2(\mathbf{Q}\cdot\mathbf{r})+|\Delta_{\mathbf{Q}}| & 0 \\ 0 & 0 & 0 & 2\varepsilon_{\mathbf{Q}}\cos^2(\mathbf{Q}\cdot\mathbf{r})+|\Delta_{\mathbf{Q}}| \end{bmatrix}.$$

Hence, we can write the Nambu basis as

$$\begin{bmatrix} \Psi_{-,\mathbf{Q}} \\ \Psi^*_{-,-\mathbf{Q}} \\ \Psi_{+,\mathbf{Q}} \\ \Psi^*_{+,-\mathbf{Q}} \end{bmatrix} = \frac{1}{\sqrt{2}} \begin{bmatrix} e^{i\theta_0}\Psi_{1,\mathbf{Q}}+\Psi^*_{2,-\mathbf{Q}} \\ e^{-i\theta_0}\Psi^*_{1,\mathbf{Q}}+\Psi_{2,-\mathbf{Q}} \\ -e^{i\theta_0}\Psi_{1,\mathbf{Q}}+\Psi^*_{2,-\mathbf{Q}} \\ -e^{-i\theta_0}\Psi^*_{1,\mathbf{Q}}+\Psi_{2,-\mathbf{Q}} \end{bmatrix}.$$

In the AMSF phase and ASF phase, the atoms prefer to stay at a lower energy level, such that in the ground state $\Psi_{+,\mathbf{Q}}=0, \Psi^*_{+,-\mathbf{Q}}=0$. We obtain $\Psi^*_{2,-\mathbf{Q}}=e^{i\theta_0}\Psi_{1,\mathbf{Q}}$, and $\Psi_{-,\mathbf{Q}}=\sqrt{2}e^{i\theta_0}\Psi_{1,\mathbf{Q}}, \Psi_{-,-\mathbf{Q}}=\sqrt{2}e^{-i\theta_0}\Psi^*_{1,\mathbf{Q}}$, where θ_0 is the angle of Δ. The free energy can be rewritten in the form of the eigenvalues and eigenstates,

$$\begin{aligned} E_{LO} &= \frac{1}{V}\int_V d^3r 2(2\varepsilon_{\mathbf{Q}}\cos^2(\mathbf{Q}\cdot\mathbf{r})-|\Delta_{\mathbf{Q}}|)|\Psi_{-,\mathbf{Q}}|^2 \\ &\quad +8\lambda|\Psi_{-,\mathbf{Q}}|^2\cos^4(\mathbf{Q}\cdot\mathbf{r}), \end{aligned}$$

We use integral

$$\frac{1}{V}\int_V d^3r\cos^2(\mathbf{Q}\cdot\mathbf{r})=\frac{1}{2}+\frac{1}{2}\delta(\mathbf{Q}),$$

$$\frac{1}{V}\int_V d^3r\cos^4(\mathbf{Q}\cdot\mathbf{r})=\frac{3}{8}+\frac{5}{8}\delta(\mathbf{Q}),$$

to obtain

$$E_{LO}=2(\varepsilon_{\mathbf{Q}}-|\Delta_{\mathbf{Q}}|)|\Psi_{-,\mathbf{Q}}|^2+3\lambda|\Psi_{-,\mathbf{Q}}|^4, \mathbf{Q}\neq 0,$$

$$E_{LO}=2(2\varepsilon_{\mathbf{Q}}-|\Delta_{\mathbf{Q}}|)|\Psi_{-,\mathbf{Q}}|^2+8\lambda|\Psi_{-,\mathbf{Q}}|^4, \mathbf{Q}=0.$$

Comparing with the calculations in the main context,

$$E_{FF}=(\varepsilon_{\mathbf{Q}}-|\Delta_{\mathbf{Q}}|)|\Psi_{-,\mathbf{Q}}|^2+\frac{1}{2}\lambda|\Psi_{-,\mathbf{Q}}|^4.$$

We can see that the FF-like state has lower energy, which is preferred in the ground state regime.

Appendix C Bogoliubov Hamiltonians

C.1 ASF Bogoliubov Hamiltonian

The Bogliubov Hamiltonian for ASF condensates is rewritten as

$$H_f = \sum_{\mathbf{k},i,j} \hat{c}^\dagger_{i,\mathbf{k}} h^{i,j}_{\mathbf{k}} \hat{c}_{j,\mathbf{k}}, \tag{C.1}$$

where $\hat{c}_{\mathbf{k}}$ and $h_{\mathbf{k}}$ are defined below,

$$\hat{c}^\dagger_{\mathbf{k}} = \begin{bmatrix} \hat{a}^\dagger_{1,\mathbf{k}} & \hat{a}_{1,-\mathbf{k}} & \hat{a}^\dagger_{2,\mathbf{k}} & \hat{a}_{2,-\mathbf{k}} & \hat{b}^\dagger_{-2,\mathbf{k}} & \hat{b}_{2,-\mathbf{k}} & \hat{b}^\dagger_{-1,\mathbf{k}} & \hat{b}_{1,-\mathbf{k}} & \hat{b}^\dagger_{0,\mathbf{k}} & \hat{b}_{0,-\mathbf{k}} & \hat{b}^\dagger_{1,\mathbf{k}} & \hat{b}_{-1,-\mathbf{k}} & \hat{b}^\dagger_{2,\mathbf{k}} & \hat{b}_{-2,-\mathbf{k}} \end{bmatrix}, \tag{C.2}$$

$$h_{\mathbf{k}} = \begin{bmatrix}
\varepsilon_{1,\mathbf{k}} & 2\tilde{\lambda}^*_1 & t_1 & t^*_{2,\mathbf{k}} & -\alpha^*_{-2,2,\mathbf{k}} & 0 & -\alpha^*_{-1,2,\mathbf{k}} & 0 & -\alpha^*_{0,2,\mathbf{k}} & 0 & -\alpha^*_{1,2,\mathbf{k}} & 0 & -\alpha^*_{2,2,\mathbf{k}} & 0 \\
2\tilde{\lambda}_1 & \varepsilon_{1,-\mathbf{k}} & t_{2,-\mathbf{k}} & t^*_1 & 0 & -\alpha_{2,2,-\mathbf{k}} & 0 & -\alpha_{1,2,-\mathbf{k}} & 0 & -\alpha_{0,2,-\mathbf{k}} & 0 & -\alpha_{-1,2,-\mathbf{k}} & 0 & -\alpha_{-2,2,-\mathbf{k}} \\
t^*_1 & t^*_{2,-\mathbf{k}} & \varepsilon_{2,\mathbf{k}} & 2\tilde{\lambda}^*_2 & -\alpha^*_{-2,1,\mathbf{k}} & 0 & -\alpha^*_{-1,1,\mathbf{k}} & 0 & -\alpha^*_{0,1,\mathbf{k}} & 0 & -\alpha^*_{1,1,\mathbf{k}} & 0 & -\alpha^*_{2,1,\mathbf{k}} & 0 \\
t_{2,\mathbf{k}} & t_1 & 2\tilde{\lambda}_2 & \varepsilon_{2,-\mathbf{k}} & 0 & -\alpha_{2,1,-\mathbf{k}} & 0 & -\alpha_{1,1,-\mathbf{k}} & 0 & -\alpha_{0,1,-\mathbf{k}} & 0 & -\alpha_{-1,1,-\mathbf{k}} & 0 & -\alpha_{-2,1,-\mathbf{k}} \\
-\alpha_{-2,2,\mathbf{k}} & 0 & -\alpha_{-2,1,\mathbf{k}} & 0 & \omega_{-2,k} & 0 & 0 & 0 & 0 & 0 & 0 & 0 & 0 & 0 \\
0 & -\alpha^*_{2,2,-\mathbf{k}} & 0 & -\alpha^*_{2,1,-\mathbf{k}} & 0 & \omega_{2,k} & 0 & 0 & 0 & 0 & 0 & 0 & 0 & 0 \\
-\alpha_{-1,2,\mathbf{k}} & 0 & -\alpha_{-1,1,\mathbf{k}} & 0 & 0 & 0 & \omega_{-1,k} & 0 & 0 & 0 & 0 & 0 & 0 & 0 \\
0 & -\alpha^*_{1,2,-\mathbf{k}} & 0 & -\alpha^*_{1,1,-\mathbf{k}} & 0 & 0 & 0 & \omega_{1,k} & 0 & 0 & 0 & 0 & 0 & \\
-\alpha_{0,2,\mathbf{k}} & 0 & -\alpha_{0,1,\mathbf{k}} & 0 & 0 & 0 & 0 & 0 & \omega_{0,k} & 0 & 0 & 0 & 0 & 0 \\
0 & -\alpha^*_{0,2,-\mathbf{k}} & 0 & -\alpha^*_{0,1,-\mathbf{k}} & 0 & 0 & 0 & 0 & 0 & \omega_{0,k} & 0 & 0 & 0 & 0 \\
-\alpha_{1,2,\mathbf{k}} & 0 & -\alpha_{1,1,\mathbf{k}} & 0 & 0 & 0 & 0 & 0 & 0 & 0 & \omega_{1,k} & 0 & 0 & 0 \\
0 & -\alpha^*_{-1,2,-\mathbf{k}} & 0 & -\alpha^*_{-1,1,-\mathbf{k}} & 0 & 0 & 0 & 0 & 0 & 0 & 0 & \omega_{-1,k} & 0 & 0 \\
-\alpha_{2,2,\mathbf{k}} & 0 & -\alpha_{2,1,\mathbf{k}} & 0 & 0 & 0 & 0 & 0 & 0 & 0 & 0 & 0 & \omega_{2,k} & 0 \\
0 & -\alpha^*_{-2,2,-\mathbf{k}} & 0 & -\alpha^*_{-2,1,-\mathbf{k}} & 0 & 0 & 0 & 0 & 0 & 0 & 0 & 0 & 0 & \omega_{-2,k}
\end{bmatrix}, \tag{C.3}$$

where the reduced parameters are defined below,

$$\varepsilon_{\sigma,\mathbf{k}} = \epsilon_k - \mu_\sigma + 2\lambda_{\sigma,\sigma}|\Psi_\sigma|^2 + \frac{\lambda_{12}+\lambda_{21}}{2}|\Psi_{\overline{\sigma}}|^2, \tag{C.4}$$

$$\omega_k = \frac{1}{2}\epsilon_{\mathbf{k}} + z(\frac{1}{2}\epsilon_{\mathbf{k}})^2 - \mu_M + g_{\mathrm{AM}}(|\Psi_1|^2 + |\Psi_2|^2), \tag{C.5}$$

$$\tilde{\lambda}_\sigma = \frac{1}{2}\lambda_{\sigma,\sigma}\Psi^{*2}_\sigma, \tag{C.6}$$

$$t_1 = \frac{1}{2}(\lambda_{12}+\lambda_{21})\Psi_1\Psi^*_2, \tag{C.7}$$

$$t_{2,\mathbf{k}} = \frac{1}{2}(\lambda_{12}+\lambda_{21})\Psi^*_1\Psi^*_2, \tag{C.8}$$

$$\alpha_{m,\sigma,\mathbf{k}} = \frac{1}{4}\overline{g}\sqrt{4\pi}\Psi_{\sigma,\mathbf{Q}_\sigma}k^2 Y^m_2(\hat{\mathbf{k}}). \tag{C.9}$$

C.2 MSF Bogoliubov Hamiltonian

The Bogliubov Hamiltonian for MSF condensates is rewritten as

$$H_f = H_A + H_M, \tag{C.10}$$

the atomic Hamiltonian H_A is given as,

$$H_A = \sum_{\mathbf{k},i,j} \hat{a}^\dagger_{i,\mathbf{k}} h^{i,j}_{A,\mathbf{k}} \hat{a}_{j,\mathbf{k}}, \tag{C.11}$$

where $\hat{a}_\mathbf{k}$ and $h_{A,\mathbf{k}}$ are defined below,

$$\hat{a}^\dagger_\mathbf{k} = (\hat{a}^\dagger_{1,\mathbf{k}}, \hat{a}^\dagger_{2,\mathbf{k}}, \hat{a}_{1,-\mathbf{k}}, \hat{a}_{2,-\mathbf{k}}), \tag{C.12}$$

$$h_{A,\mathbf{k}} = \begin{pmatrix} \varepsilon_{1,\mathbf{k}} & 0 & 0 & t^*_{2,\mathbf{k}} \\ 0 & \varepsilon_{2,\mathbf{k}} & t^*_{2,-\mathbf{k}} & 0 \\ 0 & t_{2,-\mathbf{k}} & \varepsilon_{1,-\mathbf{k}} & 0 \\ t_{2,\mathbf{k}} & 0 & 0 & \varepsilon_{2,-\mathbf{k}} \end{pmatrix}, \tag{C.13}$$

the reduced parameters are defined below,

$$\varepsilon_{\sigma,\mathbf{k}} = \epsilon_\mathbf{k} - \mu_\sigma + g_{\mathrm{AM}} n_M, \tag{C.14}$$

$$t_{2,\mathbf{k}} = \overline{g}\sqrt{4\pi} k^2 \sum_m \Phi^*_m Y^m_2(\hat{\mathbf{k}}). \tag{C.15}$$

The molecular Hamiltonian is hence given as

$$H_M = \sum_{\mathbf{k},i,j} \hat{b}^\dagger_{i,\mathbf{k}} h^{i,j}_{M,\mathbf{k}} \hat{b}_{j,\mathbf{k}}, \tag{C.16}$$

where $\hat{b}_\mathbf{k}$ and $h_{M,\mathbf{k}}$ are defined below,

$$\hat{b}^\dagger_\mathbf{k} = (\hat{b}^\dagger_{-2,\mathbf{k}}, \hat{b}_{2,-\mathbf{k}}, \hat{b}^\dagger_{-1,\mathbf{k}}, \hat{b}_{1,-\mathbf{k}}, \hat{b}^\dagger_{0,\mathbf{k}}, \hat{b}_{0,-\mathbf{k}}, \hat{b}^\dagger_{1,\mathbf{k}}, \hat{b}_{-1,-\mathbf{k}}, \hat{b}^\dagger_{2,\mathbf{k}}, \hat{b}_{-2,-\mathbf{k}}), \tag{C.17}$$

$$h_{M,\mathbf{k}} = \begin{pmatrix} \Omega_{-2} & 0 & 0 & 0 & 0 \\ 0 & \Omega_{-1} & 0 & 0 & 0 \\ 0 & 0 & \Omega_0 & 0 & 0 \\ 0 & 0 & 0 & \Omega_1 & 0 \\ 0 & 0 & 0 & 0 & \Omega_2 \end{pmatrix}, \tag{C.18}$$

where Ω_n is a 2×2 matrix, defined as

$$\Omega_{n\neq 0} = \begin{pmatrix} \omega_{n,k} & 0 \\ 0 & \omega_{-n,k} \end{pmatrix}, \tag{C.19}$$

$$\Omega_{n=0} = \begin{pmatrix} \omega_{0,k} & 2\delta_0^* \\ 2\delta_0 & \omega_{0,k} \end{pmatrix}, \tag{C.20}$$

the reduced parameters are

$$\omega_{n\neq 0,k} = \frac{1}{2}\epsilon_{\mathbf{k}} + z(\frac{1}{2}\epsilon_{\mathbf{k}})^2 - \mu_M + g_0 n_M, \tag{C.21}$$

$$\omega_{n=0,k} = \frac{1}{2}\epsilon_{\mathbf{k}} + z(\frac{1}{2}\epsilon_{\mathbf{k}})^2 - \mu_M + 2g_0 n_M, \tag{C.22}$$

$$\delta_0 = \frac{1}{2} g_0 n_M. \tag{C.23}$$

C.3 AMSF Bogoliubov Hamiltonian

The Bogliubov Hamiltonian for AMSF condensates is rewritten as

$$H_f = \sum_{\mathbf{k},i,j} \hat{c}^\dagger_{i,\mathbf{k}} h^{i,j}_{\mathbf{k}} \hat{c}_{j,\mathbf{k}}, \tag{C.24}$$

where $\hat{c}_{\mathbf{k}}$ and $h_{\mathbf{k}}$ are defined below,

$$\hat{c}^\dagger_{\mathbf{k}} = \Big[\hat{a}^\dagger_{1,\mathbf{k}} \;\; \hat{a}_{1,-\mathbf{k}} \;\; \hat{a}^\dagger_{2,\mathbf{k}} \;\; \hat{a}_{2,-\mathbf{k}} \;\; \hat{b}^\dagger_{-2,\mathbf{k}} \;\; \hat{b}_{2,-\mathbf{k}} \;\; \hat{b}^\dagger_{-1,\mathbf{k}} \;\; \hat{b}_{1,-\mathbf{k}} \;\; \hat{b}^\dagger_{0,\mathbf{k}} \;\; \hat{b}_{0,-\mathbf{k}} \;\; \hat{b}^\dagger_{1,\mathbf{k}} \;\; \hat{b}_{-1,-\mathbf{k}} \;\; \hat{b}^\dagger_{2,\mathbf{k}} \;\; \hat{b}_{-2,-\mathbf{k}}\Big], \tag{C.25}$$

$$h^{i,j}_{\mathbf{k}} = \begin{bmatrix}
\varepsilon_{1,\mathbf{k}} & 2\tilde{\lambda}^*_1 & t_1 & t^*_{2,\mathbf{k}} & -\alpha^*_{-2,2,\mathbf{k}} & 0 & -\alpha^*_{-1,2,\mathbf{k}} & 0 & -\alpha^*_{0,2,\mathbf{k}} + \beta_{1,0,1} & \beta_{2,0,1} & -\alpha^*_{1,2,\mathbf{k}} & 0 & -\alpha^*_{2,2,\mathbf{k}} & 0 \\
2\tilde{\lambda}_1 & \varepsilon_{1,-\mathbf{k}} & t_{2,-\mathbf{k}} & t^*_1 & 0 & -\alpha_{2,2,-\mathbf{k}} & 0 & -\alpha_{1,2,-\mathbf{k}} & \beta_{3,0,1} & -\alpha_{0,2,-\mathbf{k}} + \beta_{4,0,1} & 0 & -\alpha_{-1,2,-\mathbf{k}} & 0 & -\alpha_{-2,2,-\mathbf{k}} \\
t^*_1 & t^*_{2,-\mathbf{k}} & \varepsilon_{2,\mathbf{k}} & 2\tilde{\lambda}^*_2 & -\alpha^*_{-2,1,\mathbf{k}} & 0 & -\alpha^*_{-1,1,\mathbf{k}} & 0 & -\alpha^*_{0,1,\mathbf{k}} + \beta_{1,0,2} & \beta_{2,0,2} & -\alpha^*_{1,1,\mathbf{k}} & 0 & -\alpha^*_{2,1,\mathbf{k}} & 0 \\
t_{2,\mathbf{k}} & t_1 & 2\tilde{\lambda}_2 & \varepsilon_{2,-\mathbf{k}} & 0 & -\alpha_{2,1,-\mathbf{k}} & 0 & -\alpha_{1,1,-\mathbf{k}} & \beta_{3,0,2} & -\alpha_{0,1,-\mathbf{k}} + \beta_{4,0,2} & 0 & -\alpha_{-1,1,-\mathbf{k}} & 0 & -\alpha_{-2,1,-\mathbf{k}} \\
-\alpha_{-2,2,\mathbf{k}} & 0 & -\alpha_{-2,1,\mathbf{k}} & 0 & \omega_{-2,k} & 0 & 0 & 0 & 0 & 0 & 0 & 0 & 0 & 0 \\
0 & -\alpha^*_{2,2,-\mathbf{k}} & 0 & -\alpha^*_{2,1,-\mathbf{k}} & 0 & \omega_{2,k} & 0 & 0 & 0 & 0 & 0 & 0 & 0 & 0 \\
-\alpha_{-1,2,\mathbf{k}} & 0 & -\alpha_{-1,1,\mathbf{k}} & 0 & 0 & 0 & \omega_{-1,k} & 0 & 0 & 0 & 0 & 0 & 0 & 0 \\
0 & -\alpha^*_{1,2,-\mathbf{k}} & 0 & -\alpha^*_{1,1,-\mathbf{k}} & 0 & 0 & 0 & \omega_{1,k} & 0 & 0 & 0 & 0 & 0 & \\
-\alpha_{0,2,\mathbf{k}} + \beta^*_{1,0,1} & \beta^*_{3,0,1} & -\alpha_{0,1,\mathbf{k}} + \beta^*_{1,0,2} & \beta^*_{3,0,2} & 0 & 0 & 0 & 0 & \omega_{0,k} & 2\delta^*_0 & 0 & 0 & 0 & 0 \\
\beta^*_{2,0,1} & -\alpha^*_{0,2,-\mathbf{k}} + \beta^*_{4,0,1} & \beta^*_{2,0,2} & -\alpha^*_{0,1,-\mathbf{k}} + \beta^*_{4,0,2} & 0 & 0 & 0 & 0 & 2\delta_0 & \omega_{0,k} & 0 & 0 & 0 & 0 \\
-\alpha_{1,2,\mathbf{k}} & 0 & -\alpha_{1,1,\mathbf{k}} & 0 & 0 & 0 & 0 & 0 & 0 & 0 & \omega_{1,k} & 0 & 0 & 0 \\
0 & -\alpha^*_{-1,2,-\mathbf{k}} & 0 & -\alpha^*_{-1,1,-\mathbf{k}} & 0 & 0 & 0 & 0 & 0 & 0 & 0 & \omega_{-1,k} & 0 & 0 \\
-\alpha_{2,2,\mathbf{k}} & 0 & -\alpha_{2,1,\mathbf{k}} & 0 & 0 & 0 & 0 & 0 & 0 & 0 & 0 & 0 & \omega_{2,k} & 0 \\
0 & -\alpha^*_{-2,2,-\mathbf{k}} & 0 & -\alpha^*_{-2,1,-\mathbf{k}} & 0 & 0 & 0 & 0 & 0 & 0 & 0 & 0 & 0 & \omega_{-2,k}
\end{bmatrix}, \tag{C.26}$$

where the reduced parameters are given as

$$\begin{aligned}
\varepsilon_{\sigma,\mathbf{k}} &= \epsilon_{\mathbf{k}} - \mu + \lambda_{\sigma,\sigma} n_A + \frac{1}{4}(\lambda_{12} + \lambda_{21}) n_A \\
&\quad + g_{\mathrm{AM}} n_M \;, \qquad\qquad (C.27)
\end{aligned}$$

$$\begin{aligned}
\omega_{m,k} &= \frac{1}{2}\epsilon_{\mathbf{k}} + z(\frac{1}{2}\epsilon_{\mathbf{k}})^2 - \mu_M + g_0 n_M \qquad\qquad (C.28) \\
&\quad + g_0 n_M \delta_{m,0} + g_{\mathrm{AM}} n_A \;,
\end{aligned}$$

$$\tilde{\lambda}_\sigma = \frac{1}{4}\lambda_{\sigma,\sigma} n_A, \tag{C.29}$$

$$t_1 = \frac{1}{4}(\lambda_{12} + \lambda_{21}) n_A, \tag{C.30}$$

$$t_{2,\mathbf{k}} = \frac{1}{4}(\lambda_{12} + \lambda_{21}) n_A - \overline{g}\sqrt{4\pi n_M} k^2 Y^0_2(\hat{\mathbf{k}}), \tag{C.31}$$

$$\delta_m = \frac{1}{2} g_0 n_M \delta_{m,0}, \tag{C.32}$$

$$\beta_{i,0,\sigma} = g_{\mathrm{AM}} \sqrt{\frac{n_A n_M}{2}}, i = 1, 2, 3, 4, \tag{C.33}$$

$$\alpha_{m,\sigma,\mathbf{k}} = \frac{\sqrt{2\pi}}{4} \overline{g} \sqrt{n_A} k^2 Y_2^m(\hat{\mathbf{k}}), \tag{C.34}$$

where $\delta_{m,0}$ is Kronecker delta function, and n_A, n_M represent the atom and molecule condensate density respectively.

Appendix D Fast Scrambling Without Appealing to Holographic Duality: Supplementary Material

D.1 Level Statistics and Information Scrambling

An important diagnostic that is used to distinguish quantum chaotic systems from integrable systems is the energy level statistics [198, 199, 200]. Since fast scrambling can only occur when the system is non-integrable, we study the spectral statistics of our model this section. To keep our discussion slightly more general, we study the following model:

$$H = \sum_{i=1}^{N} \left(\sigma_i^z \sigma_{i+1}^z + \alpha(\sigma_i^+ \sigma_{i+1}^- + \sigma_i^- \sigma_{i+1}^+) + J \sum_{j>i} (\sigma_i^+ \sigma_j^- + \sigma_i^- \sigma_j^+) \right), \tag{D.1}$$

We examine the level statistics of this model by sorting the energy eigenvalues $E_1 < E_2 < E_3 < \ldots$, computing the adjacent energy gaps $\Delta E_n = E_{n+1} - E_n$, and then calculating the ratio of the adjacent energy gaps, $r_n = \min(\Delta E_m, \Delta E_{m+1})/\max(\Delta E_m, \Delta E_{m+1})$. Integrable systems are typically characterized by a Poisson distribution of r_n i.e. $P(r) = 2/(1+r)^2$, with a mean value of $\langle r \rangle \approx 0.39$. In contrast, thermalizing systems are characterized by Wigner-Dyson distribution of r_n i.e. $P(r) = (27/8)(r + r^2)/(1 + r + r^2)^{5/2}$, with a mean value of $\langle r \rangle \approx 0.53$. Figure 32a shows the energy level statistics for our model. We conclude that there is a wide parameter regime, where $\langle r \rangle \sim 0.53$, and the system is thermalizing in nature; the model is integrable only when $\alpha \sim 1$. While, we have focused on $\alpha = 0$ regime in the main text, we note that a small finite α does not alter the results qualitatively.

We now proceed to investigate the dynamics of the spin chain in the $\alpha = 0$ regime when J is rescaled by $1/N$. In this case, the system does not exhibit fast scrambling (see Fig. 32b). While, we have presented the $N = 100$ results here, we have verified that this result remains unchanged for other values of J and N. More generally, if J is scaled by $1/N^\alpha$, then fast scrambling can occur only when $\alpha \leq 1/2$ [117].

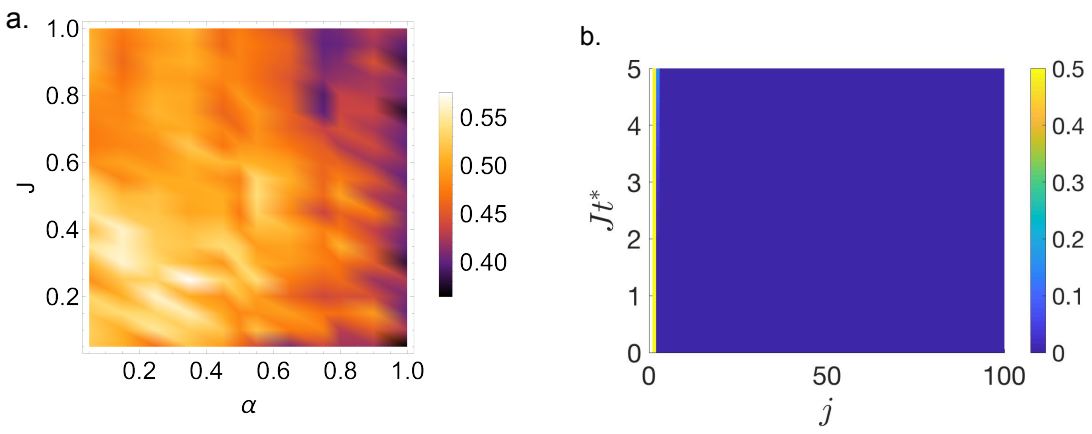

Figure 32: Level statistics and scrambling of the infinite temperature state: a: The spectral statistics for our model (Eq. D.1) when the total z-magnetization is 0, as characterized by the averaged ratio of adjacency gaps. We conclude that there is a large parameter regime, where $\langle r \rangle \sim 0.53$, and the system is non-integrable. We find that $\langle r \rangle \sim 0.39$, only when $\alpha \sim 1$, and the model is integrable. Fast scrambling is only expected when the system in non-integrable, and thus we focus on the $\alpha = 0$ regime in the main text. b: The spread of the semiclassical sensitivity, $C_{cl}(j,t)$ for a 100-site chain, when the infinite range interaction is $1/N$. In this case, the spin model does not exhibit fast scrambling.

D.2 Short Time Expansion

In the main text, we have computed the OTOC employing exact diagonalization. However, at early times, it is possible to obtain an analytical expression for the decay of the OTOC. To do this we expand the operator $\sigma_1^z(t)$ in the form

$$\sigma_1^z(t) = \sigma_1^z(0) - it[\sigma_1^z, H] - \frac{1}{2}t^2[[\sigma_1^z, H], H] + \dots . \tag{D.2}$$

Using Eq. (D.2), we can express the OTOC given in Eq. (3) of the main text as a polynomial in t. Fig. 33 shows the comparison between the numerically calculated OTOC and

analytical expression (upto $O(t^{30})$).

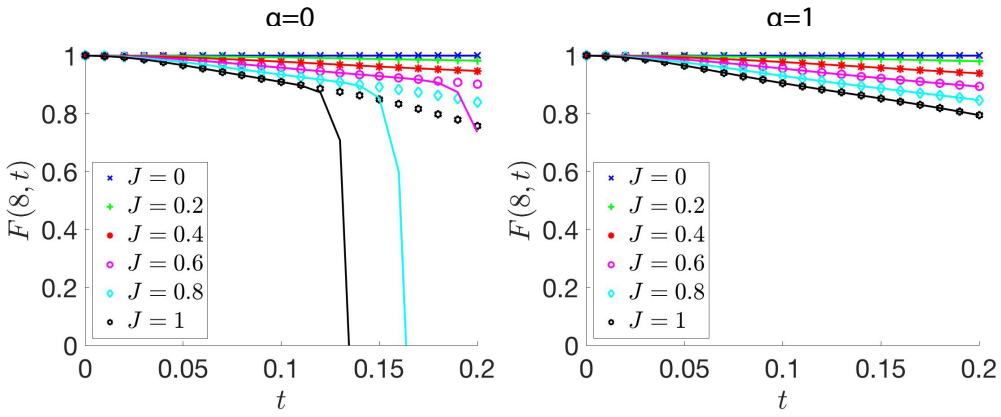

Figure 33: Comparison of an analytic short time expansion and exact diagonalization results for the OTOC, $F(8,t)$: The circles represent numerical data from the exact diagonalizaton calculation, while the lines represent the analytical expression. Both approaches agree at short times, even though they differ at longer times in the fast scrambling regime.

We find that for the non-integrable spin chain ($\alpha = 0$), there is reasonably good agreement between both approaches at short times. However, the analytical and numerical results diverge in the fast scrambling regime at longer times. The analytical expression is valid up to longer times, when the spin chain becomes integrable (i.e. $\alpha = 1$).

D.3 Quench Dynamics

We have already demonstrated that signatures of fast scrambling can be observed in the quench dynamics of the spin chain. In the main text, we had presented the results for the classical Nèel initial state. However, we had concluded that this system is expected to exhibit similar dynamical behavior for any typical initial state [117]. In this section, we examine

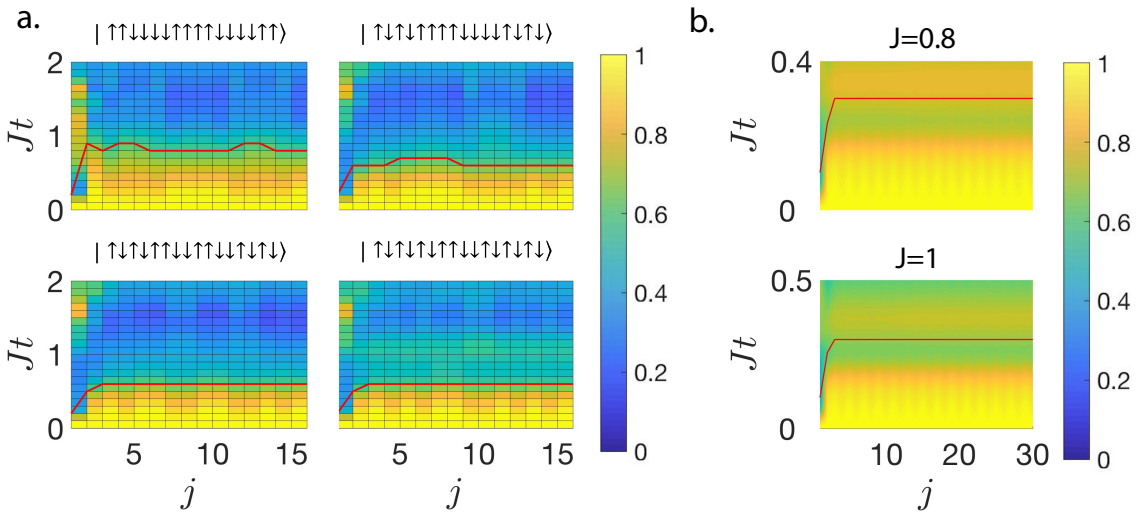

Figure 34: Quench dynamics for $J = 1$: a: Exact results for the OTOC of a 16-site chain initially prepared in various experimentally realizable product states. The initial states have been stated above each sub-figure. b: Matrix-product-state simulations for the quench dynamics of a 30-site chain initialized in the classical Néel state. It is clear the the OTOC spreads super-ballistically in all of these cases.

the dynamics of the model for some experimentally realizable initial states. By performing exact diagonalization on a 16-site chain, we find that fast scrambling can indeed be exhibited by the spin chain for several initial product states (see Fig. 34a). Furthermore, we employ matrix-product-state (MPS) techniques to access quantum dynamics for larger system sizes [190]. As shown in Fig. 34b, we find that a 30-site chain initialized in the classical Néel state exhibits super-ballistic spreading. These results agree with the exact diagonalization calculations presented in the main text.

D.4 Experimental Realization

We have mentioned in the main text that the model in Eq. (1) can be realized by coupling a spin chain to a single mode cavity [137]. In this section, we explicitly derive the effective spin Hamiltonian that arises when this scenario is realized.

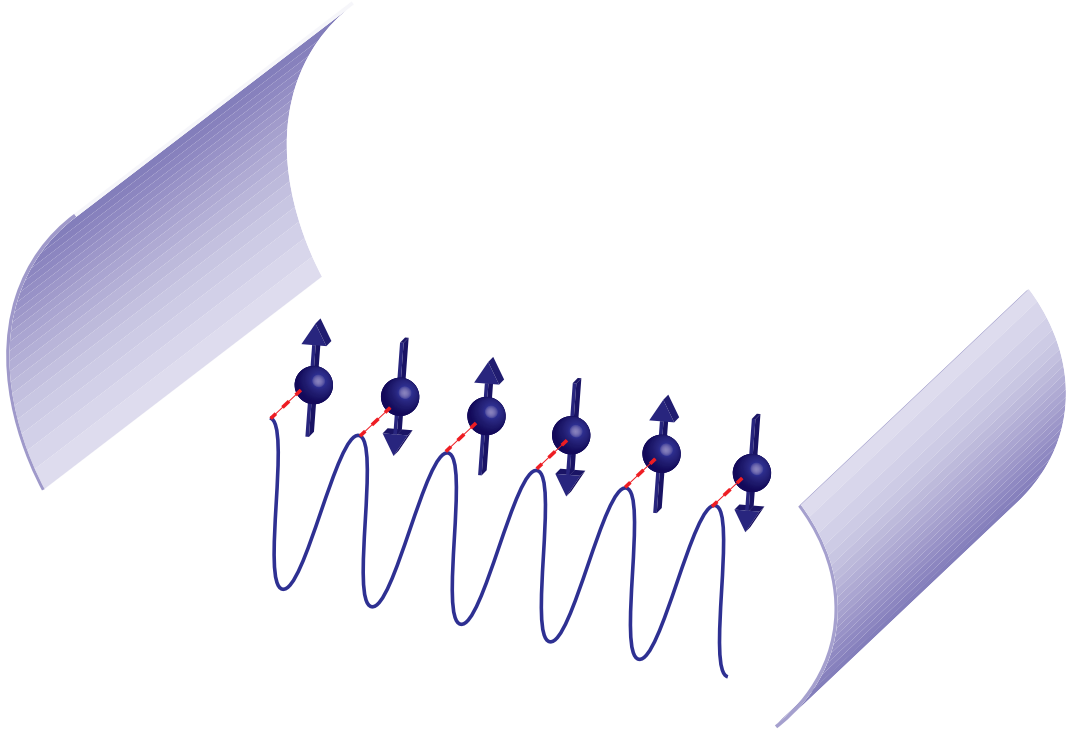

Figure 35: Schematic of the experimental realization of the spin model: The fast scrambling model that we have studied can be realized when a one dimensional spin chain is collectively coupled to an optical cavity.

The dynamics of an Ising chain interacting with a cavity can be described by the master equation:

$$\frac{d\hat{\rho}}{dt} = -i[\hat{H}_{SL}, \hat{\rho}] + \mathcal{L}_c[\hat{\rho}], \tag{D.3}$$

where $\hat{\rho}$ is the density matrix of the system. The Hamiltonian describing the unitary evolu-

tion of the system is

$$\hat{H}_{SL} = -\Delta_c \hat{a}^+ \hat{a} + J_z \sum_{i=1}^{N} \hat{\sigma}_i^z \hat{\sigma}_{i+1}^z + g \sum_{i=1}^{N} (\hat{a}^+ \hat{\sigma}_i^- + \hat{a} \hat{\sigma}_i^+), \tag{D.4}$$

where Δ_c is the effective cavity frequency, g is the coupling between the spins and the cavity field, J_z is the Ising interaction strength, and the Lindblad term capturing the photon loss from the cavity at a rate κ is given by:

$$\mathcal{L}_c[\hat{\rho}] = \frac{\kappa}{2}(2\hat{a}\hat{\rho}\hat{a}^+ - \hat{a}^+\hat{a}\hat{\rho} - \hat{\rho}\hat{a}^+\hat{a}). \tag{D.5}$$

We can eliminate the cavity mode adiabatically in the bad cavity limit ($\kappa \gg g$), and obtain a master equation for the reduced density matrix $\hat{\rho}_s$ of the spin chain,

$$\frac{d\hat{\rho}_s}{dt} = -i[\hat{H}_{\text{eff}}, \hat{\rho}_s] + \mathcal{L}_\Gamma[\hat{\rho}_s], \tag{D.6}$$

where the effective Hamiltonian is given by:

$$\hat{H}_{\text{eff}} = \frac{4g^2\Delta_c}{4\Delta_c^2 + \kappa^2} \sum_{i,j} \hat{\sigma}_i^+ \hat{\sigma}_j^- + J_z \sum_{i=1}^{L} \hat{\sigma}_i^z \hat{\sigma}_{i+1}^z, \tag{D.7}$$

and

$$\mathcal{L}_\Gamma[\hat{\rho}_s] = \frac{2g^2\kappa}{4\Delta_c^2 + \kappa^2} \sum_{i,j} (2\hat{\sigma}_i^- \hat{\rho}_s \hat{\sigma}_j^+ - \hat{\sigma}_i^+ \hat{\sigma}_j^- \hat{\rho}_s - \hat{\rho}_s \hat{\sigma}_i^+ \hat{\sigma}_j^-). \tag{D.8}$$

When $\Delta_c \gg \kappa/2$, the dynamics is approximately unitary.

For realistic state of the art experiments, $g \sim 2\pi \times 4$ Hz, $\Delta_c \sim 1$Mhz $J_z \sim 21$Hz, and $J = g^2/(\Delta_c J_z) \sim 0.76$ [135, 201]; the spin chain exhibits fast scrambling in this parameter regime (see Fig. 36). These results indicate that our proposal provides a promising avenue for observing fast scrambling in state-of-the-art quantum simulators.

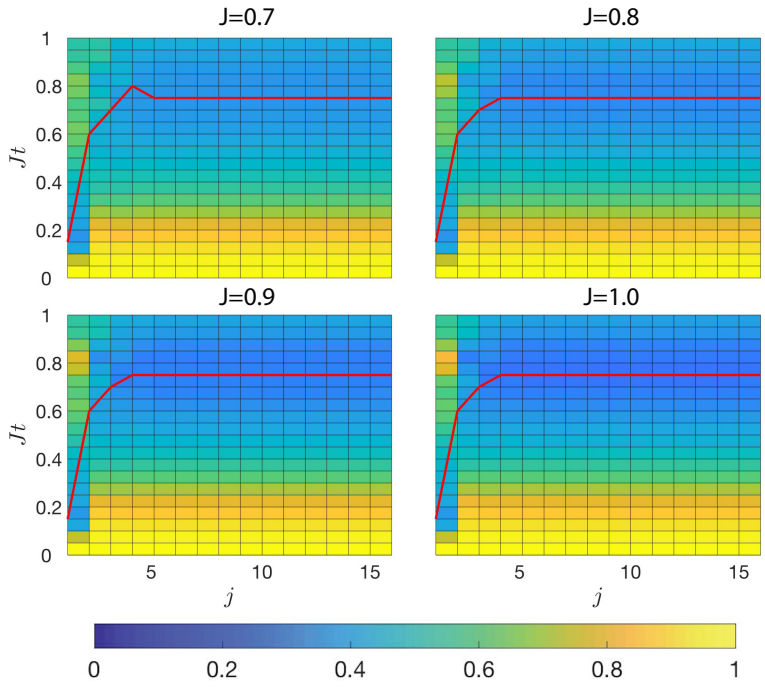

Figure 36: Fast scrambling of the infinite temperature state: The OTOC for different values of the long range interactions, J, when $N = 16$. The red line represents the time at which the OTOC reaches its minimum value. We find that when $J \sim O(1)$, the system exhibits super-ballistic spreading of the OTOC. The scrambling becomes faster with increasing J in this regime.

Bibliography

[1] T. Bourdel, J. Cubizolles, L. Khaykovich, K. M. F. Magalhães, S. J. J. M. F. Kokkelmans, G. V. Shlyapnikov, and C. Salomon. Measurement of the interaction energy near a feshbach resonance in a ^{6}Li fermi gas. *Phys. Rev. Lett.*, 91:020402, Jul 2003.

[2] Leo Radzihovsky, Peter B. Weichman, and Jae I. Park. Superfluidity and phase transitions in a resonant bose gas. *Annals of Physics*, 323(10):2376 – 2451, 2008.

[3] Anatoli Polkovnikov, Krishnendu Sengupta, Alessandro Silva, and Mukund Vengalattore. Colloquium: Nonequilibrium dynamics of closed interacting quantum systems. *Reviews of Modern Physics*, 83(3):863, 2011.

[4] M. H. Anderson, J. R. Ensher, M. R. Matthews, C. E. Wieman, and E. A. Cornell. Observation of bose-einstein condensation in a dilute atomic vapor. *Science*, 269(5221):198–201, 1995.

[5] P. G. KEVREKIDIS, R. CARRETERO-GONZÁLEZ, D. J. FRANTZESKAKIS, and I. G. KEVREKIDIS. Vortices in bose–einstein condensates: Some recent developments. *Modern Physics Letters B*, 18(30):1481–1505, 2004.

[6] K. B. Davis, M. O. Mewes, M. R. Andrews, N. J. van Druten, D. S. Durfee, D. M. Kurn, and W. Ketterle. Bose-einstein condensation in a gas of sodium atoms. *Phys. Rev. Lett.*, 75:3969–3973, Nov 1995.

[7] D. S. Jin, J. R. Ensher, M. R. Matthews, C. E. Wieman, and E. A. Cornell. Collective excitations of a bose-einstein condensate in a dilute gas. *Phys. Rev. Lett.*, 77:420–423, Jul 1996.

[8] M. R. Andrews, C. G. Townsend, H.-J. Miesner, D. S. Durfee, D. M. Kurn, and W. Ketterle. Observation of interference between two bose condensates. *Science*, 275(5300):637–641, 1997.

[9] Sungsoo Choi and Leo Radzihovsky. Finite-momentum superfluidity and phase transitions in a p-wave resonant bose gas. *Phys. Rev. A*, 84(04):043612, 2011.

[10] Zehan Li, Jian-Song Pan, and W. Vincent Liu. Superfluid phases and excitations in a cold gas of d-wave interacting bosonic atoms and molecules, 2020.

[11] Zehan Li, Jian-Song Pan, and W. Vincent Liu. Spontaneous formation of polar superfluid droplets in a p-wave interacting bose gas. *Phys. Rev. A*, 100:053620, Nov 2019.

[12] Marcos Rigol, Vanja Dunjko, and Maxim Olshanii. Thermalization and its mechanism for generic isolated quantum systems. *Nature*, 452(7189):854–858, 2008.

[13] Eyal Leviatan, Frank Pollmann, Jens H Bardarson, David A Huse, and Ehud Altman. Quantum thermalization dynamics with matrix-product states. *arXiv preprint arXiv:1702.08894*, 2017.

[14] Charles Neill, P Roushan, M Fang, Y Chen, M Kolodrubetz, Z Chen, A Megrant, R Barends, B Campbell, B Chiaro, et al. Ergodic dynamics and thermalization in an isolated quantum system. *Nature Physics*, 12(11):1037–1041, 2016.

[15] Zehan Li, Sayan Choudhury, and W. Vincent Liu. Fast scrambling without appealing to holographic duality. *Phys. Rev. Research*, 2:043399, Dec 2020.

[16] Brian Swingle, Gregory Bentsen, Monika Schleier-Smith, and Patrick Hayden. Measuring the scrambling of quantum information. *Physical Review A*, 94(4):040302(R), 2016.

[17] Norman Y Yao, Fabian Grusdt, Brian Swingle, Mikhail D Lukin, Dan M Stamper-Kurn, Joel E Moore, and Eugene A Demler. Interferometric approach to probing fast scrambling. *arXiv preprint arXiv:1607.01801*, 2016.

[18] Vedika Khemani, Ashvin Vishwanath, and David A Huse. Operator spreading and the emergence of dissipative hydrodynamics under unitary evolution with conservation laws. *Physical Review X*, 8(3):031057, 2018.

[19] Ahmet Keleş, Erhai Zhao, and W Vincent Liu. Scrambling dynamics and many-body chaos in a random dipolar spin model. *Physical Review A*, 99(5):053620, 2019.

[20] Igor L Aleiner, Lara Faoro, and Lev B Ioffe. Microscopic model of quantum butterfly effect: out-of-time-order correlators and traveling combustion waves. *Annals of Physics*, 375:378–406, 2016.

[21] Pavan Hosur, Xiao-Liang Qi, Daniel A Roberts, and Beni Yoshida. Chaos in quantum channels. *Journal of High Energy Physics*, 2016(2):4, 2016.

[22] Debanjan Chowdhury and Brian Swingle. Onset of many-body chaos in the o (n) model. *Physical Review D*, 96(6):065005, 2017.

[23] Daniel A Roberts and Douglas Stanford. Diagnosing chaos using four-point functions in two-dimensional conformal field theory. *Physical Review Letters*, 115(13):131603, 2015.

[24] Martin Gärttner, Justin G Bohnet, Arghavan Safavi-Naini, Michael L Wall, John J Bollinger, and Ana Maria Rey. Measuring out-of-time-order correlations and multiple quantum spectra in a trapped-ion quantum magnet. *Nature Physics*, 13(8):781–786, 2017.

[25] Kevin A Landsman, Caroline Figgatt, Thomas Schuster, Norbert M Linke, Beni Yoshida, Norm Y Yao, and Christopher Monroe. Verified quantum information scrambling. *Nature*, 567(7746):61–65, 2019.

[26] Manoj K Joshi, Andreas Elben, Benoît Vermersch, Tiff Brydges, Christine Maier, Peter Zoller, Rainer Blatt, and Christian F Roos. Quantum information scrambling in a trapped-ion quantum simulator with tunable range interactions. *Physical Review Letters*, 124(24):240505, 2020.

[27] Jun Li, Ruihua Fan, Hengyan Wang, Bingtian Ye, Bei Zeng, Hui Zhai, Xinhua Peng, and Jiangfeng Du. Measuring out-of-time-order correlators on a nuclear magnetic resonance quantum simulator. *Physical Review X*, 7(3):031011, 2017.

[28] Franco Dalfovo, Stefano Giorgini, Lev P. Pitaevskii, and Sandro Stringari. Theory of bose-einstein condensation in trapped gases. *Rev. Mod. Phys.*, 71:463–512, Apr 1999.

[29] U. Fano. Effects of configuration interaction on intensities and phase shifts. *Phys. Rev.*, 124:1866–1878, Dec 1961.

[30] Herman Feshbach. A unified theory of nuclear reactions. ii. *Annals of Physics*, 19(2):287 – 313, 1962.

[31] Eddy Timmermans, Paolo Tommasini, Mahir Hussein, and Arthur Kerman. Feshbach resonances in atomic Bose-Einstein condensates. *physrep*, 315(1):199–230, July 1999.

[32] Roahn Wynar, R. S. Freeland, D. J. Han, C. Ryu, and D. J. Heinzen. Molecules in a bose-einstein condensate. *Science*, 287(5455):1016–1019, 2000.

[33] Sarah T. Thompson Elizabeth A. Donley, Neil R. Claussen and Carl E. Wieman. Atom–molecule coherence in a bose–einstein condensate. *Nature*, 417:529, 2002.

[34] S. Jochim, M. Bartenstein, A. Altmeyer, G. Hendl, S. Riedl, C. Chin, J. Hecker Denschlag, and R. Grimm. Bose-einstein condensation of molecules. *Science*, 302(5653):2101–2103, 2003.

[35] Cindy A. Regal Markus Greiner and Deborah S. Jin. Emergence of a molecular bose–einstein condensate from a fermi gas. *Nature*, 426:537, 2003.

[36] M. W. Zwierlein, C. A. Stan, C. H. Schunck, S. M. F. Raupach, S. Gupta, Z. Hadzibabic, and W. Ketterle. Observation of bose-einstein condensation of molecules. *Phys. Rev. Lett.*, 91:250401, Dec 2003.

[37] J. Bardeen, L. N. Cooper, and J. R. Schrieffer. Theory of superconductivity. *Phys. Rev.*, 108:1175–1204, Dec 1957.

[38] J. Werner, A. Griesmaier, S. Hensler, J. Stuhler, T. Pfau, A. Simoni, and E. Tiesinga. Observation of feshbach resonances in an ultracold gas of ^{52}Cr. *Phys. Rev. Lett.*, 94:183201, May 2005.

[39] Q. Beaufils, A. Crubellier, T. Zanon, B. Laburthe-Tolra, E. Maréchal, L. Vernac, and O. Gorceix. Feshbach resonance in d-wave collisions. *Phys. Rev. A*, 79:032706, Mar 2009.

[40] Yue Cui, Chuyang Shen, Min Deng, Shen Dong, Cheng Chen, Rong Lü, Bo Gao, Meng Khoon Tey, and Li You. Observation of broad d-wave feshbach resonances with a triplet structure. *Phys. Rev. Lett.*, 119(20):203402, 2017.

[41] Xing-Can Yao, Ran Qi, Xiang-Pei Liu, Xiao-Qiong Wang, Yu-Xuan Wang, Yu-Ping Wu, Hao-Ze Chen, Peng Zhang, Hui Zhai, Yu-Ao Chen, et al. Degenerate bose gases near a d-wave shape resonance. *Nat. Phys.*, 15(6):570–576, 2019.

[42] Leo Radzihovsky and Sungsoo Choi. p-wave resonant bose gas: A finite-momentum spinor superfluid. *Phys. Rev. Lett.*, 103(9):095302, 2009.

[43] Zehan Li, Jian-Song Pan, and W. Vincent Liu. Spontaneous formation of polar superfluid droplets in a p-wave interacting bose gas. *Phys. Rev. A*, 100:053620, Nov 2019.

[44] Xing-Can Yao, Ran Qi, Xiang-Pei Liu, Xiao-Qiong Wang, Yu-Xuan Wang, Yu-Ping Wu, Hao-Ze Chen, Peng Zhang, Hui Zhai, Yu-Ao Chen, et al. Strongly interacting bose gases near a d-wave shape resonance. *arXiv preprint arXiv:1711.06622*, 2017.

[45] Juan Yao and Shizhong Zhang. Normal-state properties of a resonantly interacting p-wave fermi gas. *Phys. Rev. A*, 97:043612, Apr 2018.

[46] Pengfei Zhang, Shizhong Zhang, and Zhenhua Yu. Effective theory and universal relations for fermi gases near a d-wave interaction resonance. *Physical Review A*, 95(04):043609, 2016.

[47] A. B. Kuklov. Unconventional strongly interacting bose-einstein condensates in optical lattices. *Phys. Rev. Lett.*, 97:110405, Sep 2006.

[48] Peter Fulde and Richard A. Ferrell. Superconductivity in a strong spin-exchange field. *Phys. Rev.*, 135:A550, 1964.

[49] A. I. Larkin and Y. N. Ovchinnikov. Lo. *Sov. Phys. JETP*, 20:762, 1965.

[50] Pasquale Calabrese, Andrea Pelissetto, and Ettore Vicari. Multicritical phenomena in $\mathrm{O}(n_1) \bigoplus \mathrm{O}(n_2)$-symmetric theories. *Phys. Rev. B*, 67:054505, Feb 2003.

[51] DS Petrov. Quantum mechanical stabilization of a collapsing bose-bose mixture. *Phys. Rev. Lett.*, 115(15):155302, 2015.

[52] G Semeghini, G Ferioli, L Masi, C Mazzinghi, L Wolswijk, F Minardi, M Modugno, G Modugno, M Inguscio, and M Fattori. Self-bound quantum droplets of atomic mixtures in free space. *Phys. Rev. Lett.*, 120(23):235301, 2018.

[53] P Cheiney, CR Cabrera, J Sanz, B Naylor, L Tanzi, and L Tarruell. Bright soliton to quantum droplet transition in a mixture of bose-einstein condensates. *Phys. Rev. Lett.*, 120(13):135301, 2018.

[54] CR Cabrera, L Tanzi, J Sanz, B Naylor, P Thomas, P Cheiney, and L Tarruell. Quantum liquid droplets in a mixture of bose-einstein condensates. *Science*, 359(6373):301–304, 2018.

[55] Yaroslav V. Kartashov, Boris A. Malomed, Leticia Tarruell, and Lluis Torner. Three-dimensional droplets of swirling superfluids. *Phys. Rev. A*, 98:013612, Jul 2018.

[56] Igor Ferrier-Barbut, Holger Kadau, Matthias Schmitt, Matthias Wenzel, and Tilman Pfau. Observation of quantum droplets in a strongly dipolar bose gas. *Phys. Rev. Lett.*, 116(21):215301, 2016.

[57] Holger Kadau, Matthias Schmitt, Matthias Wenzel, Clarissa Wink, Thomas Maier, Igor Ferrier-Barbut, and Tilman Pfau. Observing the rosensweig instability of a quantum ferrofluid. *Nature*, 530(7589):194, 2016.

[58] L Chomaz, S Baier, D Petter, MJ Mark, F Wächtler, Luis Santos, and F Ferlaino. Quantum-fluctuation-driven crossover from a dilute bose-einstein condensate to a macrodroplet in a dipolar quantum fluid. *Phys. Rev. X*, 6(4):041039, 2016.

[59] Matthias Schmitt, Matthias Wenzel, Fabian Böttcher, Igor Ferrier-Barbut, and Tilman Pfau. Self-bound droplets of a dilute magnetic quantum liquid. *Nature*, 539(7628):259, 2016.

[60] Aurel Bulgac. Dilute quantum droplets. *Phys. Rev. Lett.*, 89(5):050402, 2002.

[61] Yuta Sekino and Yusuke Nishida. Quantum droplet of one-dimensional bosons with a three-body attraction. *Phys. Rev. A*, 97(1):011602, 2018.

[62] Xiaoling Cui. Spin-orbit-coupling-induced quantum droplet in ultracold bose-fermi mixtures. *Phys. Rev. A*, 98(2):023630, 2018.

[63] Kerson Huang T. D. Lee and C. N. Yang. Lhy effect. *Phys. Rev.*, 106:1135, 1957.

[64] SB Papp, JM Pino, and CE Wieman. Tunable miscibility in a dual-species bose-einstein condensate. *Phys. Rev. Lett.*, 101(4):040402, 2008.

[65] Shen Dong, Yue Cui, Chuyang Shen, Yewei Wu, Meng Khoon Tey, Li You, and Bo Gao. Observation of broad p-wave feshbach resonances in ultracold rb 85- rb 87 mixtures. *Phys. Rev. A*, 94(6):062702, 2016.

[66] E Aybar and MÖ Oktel. Temperature-dependent density profiles of dipolar droplets. *Phys. Rev. A*, 99(1):013620, 2019.

[67] Nikolay Nikolaevich Bogolyubov. On the theory of superfluidity. *Izv. Akad. Nauk Ser. Fiz.*, 11:23–32, 1947.

[68] C. J. Pethick and H. Smith. *Bose-Einstein Condensation in Dilute Gases*. Cambridge University Press, 2 edition, 2008.

[69] V Gurarie and L Radzihovsky. Resonantly paired fermionic superfluids. *Annals of Physics*, 322(1):2–119, 2007.

[70] Fang Qin. Universal relations and normal-state properties of a fermi gas with laser-dressed mixed-partial-wave interactions. *Phys. Rev. A*, 98(5):053621, 2018.

[71] Christopher Luciuk, Stefan Trotzky, Scott Smale, Zhenhua Yu, Shizhong Zhang, and Joseph H Thywissen. Evidence for universal relations describing a gas with p-wave interactions. *Nature Physics*, 12(6):599, 2016.

[72] Krishnanand Mallayya, Marcos Rigol, and Wojciech De Roeck. Prethermalization and thermalization in isolated quantum systems. *Physical Review X*, 9(2):021027, 2019.

[73] Christopher David White, Michael Zaletel, Roger S K Mong, and Gil Refael. Quantum dynamics of thermalizing systems. *Physical Review B*, 97(3):035127, 2018.

[74] Adam Nahum, Jonathan Ruhman, Sagar Vijay, and Jeongwan Haah. Quantum entanglement growth under random unitary dynamics. *Physical Review X*, 7(3):031016, 2017.

[75] Daniel E Parker, Xiangyu Cao, Alexander Avdoshkin, Thomas Scaffidi, and Ehud Altman. A universal operator growth hypothesis. *Physical Review X*, 9(4):041017, 2019.

[76] Takashi Mori, Tatsuhiko N Ikeda, Eriko Kaminishi, and Masahito Ueda. Thermalization and prethermalization in isolated quantum systems: a theoretical overview. *Journal of Physics B: Atomic, Molecular and Optical Physics*, 51(11):112001, 2018.

[77] Martin Gärttner, Philipp Hauke, and Ana Maria Rey. Relating out-of-time-order correlations to entanglement via multiple-quantum coherences. *Physical Review Letters*, 120(4):040402, 2018.

[78] J Marino and Ana Maria Rey. Cavity-qed simulator of slow and fast scrambling. *Physical Review A*, 99(5):051803(R), 2019.

[79] Shenglong Xu and Brian Swingle. Locality, quantum fluctuations, and scrambling. *Physical Review X*, 9(3):031048, 2019.

[80] Shenglong Xu and Brian Swingle. Accessing scrambling using matrix product operators. *Nature Physics*, 16(2):199–204, 2020.

[81] Wouter Buijsman, Vladimir Gritsev, and Rudolf Sprik. Nonergodicity in the anisotropic dicke model. *Physical Review Letters*, 118(8):080601, 2017.

[82] Yahya Alavirad and Ali Lavasani. Scrambling in the dicke model. *Physical Review A*, 99(4):043602, 2019.

[83] Jorge Chávez-Carlos, B López-del-Carpio, Miguel A Bastarrachea-Magnani, Pavel Stránskỳ, Sergio Lerma-Hernández, Lea F Santos, and Jorge G Hirsch. Quantum and classical lyapunov exponents in atom-field interaction systems. *Physical Review Letters*, 122(2):024101, 2019.

[84] Po-Yao Chang, Xiao Chen, Sarang Gopalakrishnan, and JH Pixley. Evolution of entanglement spectra under generic quantum dynamics. *Physical Review Letters*, 123(19):190602, 2019.

[85] Aurélia Chenu, Javier Molina-Vilaplana, and Adolfo Del Campo. Work statistics, loschmidt echo and information scrambling in chaotic quantum systems. *Quantum*, 3:127, 2019.

[86] Nima Lashkari, Douglas Stanford, Matthew Hastings, Tobias Osborne, and Patrick Hayden. Towards the fast scrambling conjecture. *Journal of High Energy Physics*, 2013(4):22, 2013.

[87] Yasuhiro Sekino and Leonard Susskind. Fast scramblers. *Journal of High Energy Physics*, 2008(10):065, 2008.

[88] Stephen H Shenker and Douglas Stanford. Black holes and the butterfly effect. *Journal of High Energy Physics*, 2014(3):67, 2014.

[89] Juan Maldacena, Stephen H Shenker, and Douglas Stanford. A bound on chaos. *Journal of High Energy Physics*, 2016(8):106, 2016.

[90] Tianrui Xu, Thomas Scaffidi, and Xiangyu Cao. Does scrambling equal chaos? *Physical Review Letters*, 124(14):140602, 2020.

[91] Hao Geng. Non-local entanglement and fast scrambling in de-sitter holography. *arXiv preprint arXiv:2005.00021*, 2020.

[92] Kaushik Y Bhagat, Baibhab Bose, Sayantan Choudhury, Satyaki Chowdhury, Rathindra N Das, Saptarshhi G Dastider, Nitin Gupta, Archana Maji, Gabriel D Pasquino, and Swaraj Paul. The generalized otoc from supersymmetric quantum mechanics: Study of random fluctuations from eigenstate representation of correlation functions. *arXiv preprint arXiv:2008.03280*, 2020.

[93] Sayantan Choudhury. The cosmological otoc: Formulating new cosmological microcanonical correlation functions for random chaotic fluctuations in out-of-equilibrium quantum statistical field theory. *arXiv preprint arXiv:2005.11750*, 2020.

[94] Ken Xuan Wei, Pai Peng, Oles Shtanko, Iman Marvian, Seth Lloyd, Chandrasekhar Ramanathan, Paola Cappellaro, et al. Emergent prethermalization signatures in out-of-time ordered correlations. *Physical Review Letters*, 123(9):090605, 2019.

[95] Deepak Khurana, VR Krithika, and TS Mahesh. Unambiguous measurement of information scrambling in a hierarchical star-topology system. *arXiv preprint arXiv:1906.02692*, 2019.

[96] MS Blok, VV Ramasesh, T Schuster, K O'Brien, JM Kreikebaum, D Dahlen, A Morvan, B Yoshida, NY Yao, and I Siddiqi. Quantum information scrambling in a superconducting qutrit processor. *arXiv preprint arXiv:2003.03307*, 2020.

[97] Eric J Meier, Jackson Ang'ong'a, Fangzhao Alex An, and Bryce Gadway. Exploring quantum signatures of chaos on a floquet synthetic lattice. *Physical Review A*, 100(1):013623, 2019.

[98] Patrick Hayden and John Preskill. Black holes as mirrors: quantum information in random subsystems. *Journal of High Energy Physics*, 2007(09):120–120, sep 2007.

[99] Yasuhiro Sekino and L Susskind. Fast scramblers. *Journal of High Energy Physics*, 2008(10):065–065, oct 2008.

[100] Nima Lashkari, Douglas Stanford, Matthew Hastings, Tobias Osborne, and Patrick Hayden. Towards the Fast Scrambling Conjecture. *JHEP*, 04:022, 2013.

[101] Stefan Leichenauer. Disrupting entanglement of black holes. *Phys. Rev. D*, 90:046009, Aug 2014.

[102] Subir Sachdev and Jinwu Ye. Gapless spin-fluid ground state in a random quantum heisenberg magnet. *Physical Review Letters*, 70(21):3339, 1993.

[103] Alexei Kitaev. A simple model of quantum holography. In *Proceedings of the KITP program: Entanglement in Strongly-Correlated Quantum Matter, Santa Barbara, CA*, 2015.

[104] Juan Maldacena and Douglas Stanford. Remarks on the sachdev-ye-kitaev model. *Physical Review D*, 94(10):106002, 2016.

[105] Yingfei Gu, Xiao-Liang Qi, and Douglas Stanford. Local criticality, diffusion and chaos in generalized sachdev-ye-kitaev models. *Journal of High Energy Physics*, 2017(5):125, 2017.

[106] Richard A Davison, Wenbo Fu, Antoine Georges, Yingfei Gu, Kristan Jensen, and Subir Sachdev. Thermoelectric transport in disordered metals without quasiparticles: The sachdev-ye-kitaev models and holography. *Physical Review B*, 95(15):155131, 2017.

[107] Gautam Mandal, Pranjal Nayak, and Spenta R Wadia. Coadjoint orbit action of virasoro group and two-dimensional quantum gravity dual to syk/tensor models. *Journal of High Energy Physics*, 2017(11):46, 2017.

[108] Shao-Kai Jian, Zhuo-Yu Xian, and Hong Yao. Quantum criticality and duality in the sachdev-ye-kitaev/ads 2 chain. *Physical Review B*, 97(20):205141, 2018.

[109] Adwait Gaikwad, Lata Kh Joshi, Gautam Mandal, and Spenta R Wadia. Holographic dual to charged syk from 3d gravity and chern-simons. *Journal of High Energy Physics*, 2020(2):33, 2020.

[110] Subir Sachdev. Bekenstein-hawking entropy and strange metals. *Physical Review X*, 5(4):041025, 2015.

[111] Gregory Bentsen, Tomohiro Hashizume, Anton S Buyskikh, Emily J Davis, Andrew J Daley, Steven S Gubser, and Monika Schleier-Smith. Treelike interactions and fast scrambling with cold atoms. *Physical Review Letters*, 123(13):130601, 2019.

[112] Steven S Gubser, Johannes Knaute, Sarthak Parikh, Andreas Samberg, and Przemek Witaszczyk. p-adic ads/cft. *Communications in Mathematical Physics*, 352(3):1019–1059, 2017.

[113] Elliott H Lieb and Derek W Robinson. The finite group velocity of quantum spin systems. In *Statistical mechanics*, pages 425–431. Springer, 1972.

[114] Gregory Bentsen, Ionut-Dragos Potirniche, Vir B Bulchandani, Thomas Scaffidi, Xiangyu Cao, Xiao-Liang Qi, Monika Schleier-Smith, and Ehud Altman. Integrable and chaotic dynamics of spins coupled to an optical cavity. *Physical Review X*, 9(4):041011, 2019.

[115] See Supplementary Material.

[116] Ron Belyansky, Przemyslaw Bienias, Yaroslav A Kharkov, Alexey V Gorshkov, and Brian Swingle. A minimal model for fast scrambling. *arXiv preprint arXiv:2005.05362*, 2020.

[117] Chao Yin and Andrew Lucas. Bound on quantum scrambling with all-to-all interactions. *Physical Review A*, 102(2):022402, 2020.

[118] Harry J Lipkin, N Meshkov, and AJ Glick. Validity of many-body approximation methods for a solvable model:(i). exact solutions and perturbation theory. *Nuclear Physics*, 62(2):188–198, 1965.

[119] Pedro Ribeiro, Julien Vidal, and Rémy Mosseri. Thermodynamical limit of the lipkin-meshkov-glick model. *Physical Review Letters*, 99(5):050402, 2007.

[120] Masuo Suzuki, Bunjiro Tsujiyama, and Shigetoshi Katsura. One-dimensional ising model with general spin. *Journal of Mathematical Physics*, 8(1):124–130, 1967.

[121] Lea F Santos, Fausto Borgonovi, and Giuseppe Luca Celardo. Cooperative shielding in many-body systems with long-range interaction. *Physical Review Letters*, 116(25):250402, 2016.

[122] G L Celardo, R Kaiser, and Fausto Borgonovi. Shielding and localization in the presence of long-range hopping. *Physical Review B*, 94(14):144206, 2016.

[123] Alessio Lerose, Bojan Žunkovič, Jamir Marino, Andrea Gambassi, and Alessandro Silva. Impact of nonequilibrium fluctuations on prethermal dynamical phase transitions in long-range interacting spin chains. *Physical Review B*, 99(4):045128, 2019.

[124] Alessio Lerose, Jamir Marino, Bojan Žunkovič, Andrea Gambassi, and Alessandro Silva. Chaotic dynamical ferromagnetic phase induced by nonequilibrium quantum fluctuations. *Physical Review Letters*, 120(13):130603, 2018.

[125] Bihui Zhu, Jamir Marino, Norman Y Yao, Mikhail D Lukin, and Eugene A Demler. Dicke time crystals in driven-dissipative quantum many-body systems. *New Journal of Physics*, 21(7):073028, 2019.

[126] Bhuvanesh Sundar and Erich J Mueller. Lattice bosons with infinite-range checkerboard interactions. *Physical Review A*, 94(3):033631, 2016.

[127] Yikai Chen and Zi Cai. Persistent oscillations versus thermalization in the quench dynamics of quantum gases with long-range interactions. *Physical Review A*, 101(2):023611, 2020.

[128] Wenbo Fu and Subir Sachdev. Numerical study of fermion and boson models with infinite-range random interactions. *Physical Review B*, 94(3):035135, 2016.

[129] Gregory Bentsen, Yingfei Gu, and Andrew Lucas. Fast scrambling on sparse graphs. *Proceedings of the National Academy of Sciences*, 116(14):6689–6694, 2019.

[130] Jordan S Cotler, Dawei Ding, and Geoffrey R Penington. Out-of-time-order operators and the butterfly effect. *Annals of Physics*, 396:318–333, 2018.

[131] R. J. Lewis-Swan, A Safavi-Naini, J. J. Bollinger, and A. M. Rey. Unifying scrambling, thermalization and entanglement through measurement of fidelity out-of-time-order correlators in the dicke model. *Nature Communications*, 10(1):1581, 2019.

[132] Filippo Caruso, Alex W Chin, Animesh Datta, Susana F Huelga, and Martin B Plenio. Highly efficient energy excitation transfer in light-harvesting complexes: The fundamental role of noise-assisted transport. *The Journal of Chemical Physics*, 131(10):09B612, 2009.

[133] Helmut Ritsch, Peter Domokos, Ferdinand Brennecke, and Tilman Esslinger. Cold atoms in cavity-generated dynamical optical potentials. *Reviews of Modern Physics*, 85(2):553, 2013.

[134] Jiří Minář, Şebnem Güneş Söyler, Pietro Rotondo, and Igor Lesanovsky. Effective spin physics in two-dimensional cavity qed arrays. *New Journal of Physics*, 19(6):063033, 2017.

[135] Matthew A Norcia, Robert J Lewis-Swan, Julia RK Cline, Bihui Zhu, Ana M Rey, and James K Thompson. Cavity-mediated collective spin-exchange interactions in a strontium superradiant laser. *Science*, 361(6399):259–262, 2018.

[136] Emily J Davis, Avikar Periwal, Eric S Cooper, Gregory Bentsen, Simon J Evered, Katherine Van Kirk, and Monika H Schleier-Smith. Protecting spin coherence in a tunable heisenberg model. *Physical Review Letters*, 125(6):060402, 2020.

[137] Jan Gelhausen, Michael Buchhold, Achim Rosch, and Philipp Strack. Quantum-optical magnets with competing short-and long-range interactions: Rydberg-dressed spin lattice in an optical cavity. *SciPost Phys*, 1:004, 2016.

[138] Søren Gammelmark and Klaus Mølmer. Phase transitions and heisenberg limited metrology in an ising chain interacting with a single-mode cavity field. *New Journal of Physics*, 13(5):053035, 2011.

[139] Xi-Wang Luo, Yu-Na Zhang, Xingxiang Zhou, Guang-Can Guo, and Zheng-Wei Zhou. Dynamic phase transitions of a driven ising chain in a dissipative cavity. *Physical Review A*, 94(5):053809, 2016.

[140] C-L Hung, Alejandro González-Tudela, J Ignacio Cirac, and HJ Kimble. Quantum spin dynamics with pairwise-tunable, long-range interactions. *Proceedings of the National Academy of Sciences*, 113(34):E4946–E4955, 2016.

[141] Iñigo Arrazola, Julen S Pedernales, Lucas Lamata, and Enrique Solano. Digital-analog quantum simulation of spin models in trapped ions. *Scientific reports*, 6:30534, 2016.

[142] Benoît Vermersch, Andreas Elben, Lukas M Sieberer, Norman Y Yao, and Peter Zoller. Probing scrambling using statistical correlations between randomized measurements. *Physical Review X*, 9(2):021061, 2019.

[143] Étienne Lantagne-Hurtubise, Stephan Plugge, Oguzhan Can, and Marcel Franz. Diagnosing quantum chaos in many-body systems using entanglement as a resource. *Physical Review Research*, 2(1):013254, 2020.

[144] Philip Daniel Blocher, Serwan Asaad, Vincent Mourik, Mark AI Johnson, Andrea Morello, and Klaus Mølmer. Measuring out-of-time-ordered correlation functions without reversing time evolution. *arXiv preprint arXiv:2003.03980*, 2020.

[145] Bryce Kobrin, Zhenbin Yang, Gregory D Kahanamoku-Meyer, Christopher T Olund, Joel E Moore, Douglas Stanford, and Norman Y Yao. Many-body chaos in the sachdev-ye-kitaev model. *arXiv preprint arXiv:2002.05725*, 2020.

[146] Andrew Lucas. Non-perturbative dynamics of the operator size distribution in the sachdev–ye–kitaev model. *Journal of Mathematical Physics*, 61(8):081901, 2020.

[147] Andrew Lucas. Quantum many-body dynamics on the star graph. *arXiv preprint arXiv:1903.01468*, 2019.

[148] Adam R Brown, Hrant Gharibyan, Stefan Leichenauer, Henry W Lin, Sepehr Nezami, Grant Salton, Leonard Susskind, Brian Swingle, and Michael Walter. Quantum gravity in the lab: teleportation by size and traversable wormholes. *arXiv preprint arXiv:1911.06314*, 2019.

[149] Run-Qiu Yang, Hui Liu, Shining Zhu, Le Luo, and Rong-Gen Cai. Simulating quantum field theory in curved spacetime with quantum many-body systems. *Physical Review Research*, 2(2):023107, 2020.

[150] Stephan Plugge, Étienne Lantagne-Hurtubise, and Marcel Franz. Revival dynamics in a traversable wormhole. *Physical Review Letters*, 124(22):221601, 2020.

[151] Adam R Brown, Daniel A Roberts, Leonard Susskind, Brian Swingle, and Ying Zhao. Holographic complexity equals bulk action? *Physical Review Letters*, 116(19):191301, 2016.

[152] Adam R Brown, Daniel A Roberts, Leonard Susskind, Brian Swingle, and Ying Zhao. Complexity, action, and black holes. *Physical Review D*, 93(8):086006, 2016.

[153] Ameneh Sheikhan, Ferdinand Brennecke, and Corinna Kollath. Cavity-induced chiral states of fermionic quantum gases. *Physical Review A*, 93(4):043609, 2016.

[154] Renate Landig, Lorenz Hruby, Nishant Dogra, Manuele Landini, Rafael Mottl, Tobias Donner, and Tilman Esslinger. Quantum phases from competing short-and long-range interactions in an optical lattice. *Nature*, 532(7600):476–479, 2016.

[155] Benjamin Blaß, Heiko Rieger, Gergő Roósz, and Ferenc Iglói. Quantum relaxation and metastability of lattice bosons with cavity-induced long-range interactions. *Physical Review Letters*, 121(9):095301, 2018.

[156] Ameneh Sheikhan and Corinna Kollath. Cavity-induced superconducting and 4 k f charge-density-wave states. *Physical Review A*, 99(5):053611, 2019.

[157] Catalin-Mihai Halati, Ameneh Sheikhan, and Corinna Kollath. Cavity-induced spin-orbit coupling in an interacting bosonic wire. *Physical Review A*, 99(3):033604, 2019.

[158] Catalin-Mihai Halati, Ameneh Sheikhan, and Corinna Kollath. Cavity-induced artificial gauge field in a bose-hubbard ladder. *Physical Review A*, 96(6):063621, 2017.

[159] Astrid E Niederle, Giovanna Morigi, and Heiko Rieger. Ultracold bosons with cavity-mediated long-range interactions: A local mean-field analysis of the phase diagram. *Physical Review A*, 94(3):033607, 2016.

[160] Alessio Chiocchetta, Dominik Kiese, Francesco Piazza, and Sebastian Diehl. Cavity-induced quantum spin liquids. *arXiv preprint arXiv:2009.11856*, 2020.

[161] Nishant Dogra, Ferdinand Brennecke, Sebastian D Huber, and Tobias Donner. Phase transitions in a bose-hubbard model with cavity-mediated global-range interactions. *Physical Review A*, 94(2):023632, 2016.

[162] Yu Chen, Zhenhua Yu, and Hui Zhai. Quantum phase transitions of the bose-hubbard model inside a cavity. *Physical Review A*, 93(4):041601, 2016.

[163] Frank Schlawin and Dieter Jaksch. Cavity-mediated unconventional pairing in ultracold fermionic atoms. *Physical Review Letters*, 123(13):133601, 2019.

[164] Frank Schlawin, Andrea Cavalleri, and Dieter Jaksch. Cavity-mediated electron-photon superconductivity. *Physical Review Letters*, 122(13):133602, 2019.

[165] Ahana Chakraborty and Francesco Piazza. Non-bcs-type enhancement of superconductivity from long-range photon fluctuations. *arXiv preprint arXiv:2008.06513*, 2020.

[166] Huang-Jie Chen, Yan-Qiang Yu, Dong-Chen Zheng, and Renyuan Liao. Extended bose-hubbard model with cavity-mediated infinite-range interactions at finite temperatures. *Scientific Reports*, 10(1):1–7, 2020.

[167] Kristopher Tucker, Bihui Zhu, Robert J Lewis-Swan, Jamir Marino, Felix Jimenez, Juan G Restrepo, and Ana Maria Rey. Shattered time: can a dissipative time crystal survive many-body correlations? *New Journal of Physics*, 20(12):123003, 2018.

[168] Hans Keßler, Jayson G Cosme, Michal Hemmerling, Ludwig Mathey, and Andreas Hemmerich. Emergent limit cycles and time crystal dynamics in an atom-cavity system. *Physical Review A*, 99(5):053605, 2019.

[169] Ameneh Sheikhan, Ferdinand Brennecke, and Corinna Kollath. Cavity-induced generation of nontrivial topological states in a two-dimensional fermi gas. *Physical Review A*, 94(6):061603, 2016.

[170] Jens Klinder, Hans Keßler, Matthias Wolke, Ludwig Mathey, and Andreas Hemmerich. Dynamical phase transition in the open dicke model. *Proceedings of the National Academy of Sciences*, 112(11):3290–3295, 2015.

[171] Juan A Muniz, Diego Barberena, Robert J Lewis-Swan, Dylan J Young, Julia RK Cline, Ana Maria Rey, and James K Thompson. Exploring dynamical phase transitions with cold atoms in an optical cavity. *Nature*, 580(7805):602–607, 2020.

[172] AV Lunkin, KS Tikhonov, and MV Feigel'man. Sachdev-ye-kitaev model with quadratic perturbations: The route to a non-fermi liquid. *Physical Review Letters*, 121(23):236601, 2018.

[173] Xue-Yang Song, Chao-Ming Jian, and Leon Balents. Strongly correlated metal built from sachdev-ye-kitaev models. *Physical Review Letters*, 119(21):216601, 2017.

[174] Étienne Lantagne-Hurtubise, Chengshu Li, and Marcel Franz. Family of sachdev-ye-kitaev models motivated by experimental considerations. *Physical Review B*, 97(23):235124, 2018.

[175] Arijit Haldar, Sumilan Banerjee, and Vijay B Shenoy. Higher-dimensional sachdev-ye-kitaev non-fermi liquids at lifshitz transitions. *Physical Review B*, 97(24):241106(R), 2018.

[176] Mohammad F Maghrebi, Zhe-Xuan Gong, and Alexey V Gorshkov. Continuous symmetry breaking in 1d long-range interacting quantum systems. *Physical Review Letters*, 119(2):023001, 2017.

[177] M Gaudin. Thermodynamics of the heisenberg-ising ring for $\delta >\tilde{}$ 1. *Physical Review Letters*, 26(21):1301, 1971.

[178] C Destri and HJ De Vega. New thermodynamic bethe ansatz equations without strings. *Physical Review Letters*, 69(16):2313, 1992.

[179] Peter Barmettler, Matthias Punk, Vladimir Gritsev, Eugene Demler, and Ehud Altman. Quantum quenches in the anisotropic spin-heisenberg chain: different approaches to many-body dynamics far from equilibrium. *New Journal of Physics*, 12(5):055017, 2010.

[180] N David Mermin and Herbert Wagner. Absence of ferromagnetism or antiferromagnetism in one-or two-dimensional isotropic heisenberg models. *Physical Review Letters*, 17(22):1133, 1966.

[181] Thierry Giamarchi. *Quantum physics in one dimension*, volume 121. Oxford University Press, Oxford, UK, 2004.

[182] R Botet, R Jullien, and P Pfeuty. Size scaling for infinitely coordinated systems. *Physical Review Letters*, 49(7):478, 1982.

[183] Bojan Žunkovič, Alessandro Silva, and Michele Fabrizio. Dynamical phase transitions and loschmidt echo in the infinite-range xy model. *Philosophical Transactions of the Royal Society A: Mathematical, Physical and Engineering Sciences*, 374(2069):20150160, 2016.

[184] T Holstein and Hl Primakoff. Field dependence of the intrinsic domain magnetization of a ferromagnet. *Physical Review*, 58(12):1098, 1940.

[185] Minoru Takahashi. Modified spin-wave theory of a square-lattice antiferromagnet. *Physical Review B*, 40(4):2494, 1989.

[186] Steven R White. Density matrix formulation for quantum renormalization groups. *Physical review letters*, 69(19):2863, 1992.

[187] Steven R White. Density-matrix algorithms for quantum renormalization groups. *Physical Review B*, 48(14):10345, 1993.

[188] Steven R White and Adrian E Feiguin. Real-time evolution using the density matrix renormalization group. *Physical Review Letters*, 93(7):076401, 2004.

[189] U. Schollwöck. The density-matrix renormalization group. *Rev. Mod. Phys.*, 77(1):259–315, 2005.

[190] Ulrich Schollwöck. The density-matrix renormalization group in the age of matrix product states. *Annals of physics*, 326(1):96–192, 2011.

[191] Jie Ren, Wen-Long You, and Xiaoqun Wang. Entanglement and correlations in a one-dimensional quantum spin-1 2 chain with anisotropic power-law long-range interactions. *Physical Review B*, 101(9):094410, 2020.

[192] Glen Evenbly. *Tensors.net (https://www.tensors.net/)*, 2019.

[193] Thomas Koffel, M Lewenstein, and Luca Tagliacozzo. Entanglement entropy for the long-range ising chain in a transverse field. *Physical review letters*, 109(26):267203, 2012.

[194] Davide Vodola, Luca Lepori, Elisa Ercolessi, and Guido Pupillo. Long-range ising and kitaev models: phases, correlations and edge modes. *New Journal of Physics*, 18(1):015001, 2015.

[195] Jens Eisert, Marcus Cramer, and Martin B Plenio. Colloquium: Area laws for the entanglement entropy. *Reviews of Modern Physics*, 82(1):277, 2010.

[196] Pasquale Calabrese and John Cardy. Entanglement entropy and quantum field theory. *Journal of Statistical Mechanics: Theory and Experiment*, 2004(06):P06002, 2004.

[197] Z-X Gong, Mohammad F Maghrebi, Anzi Hu, Michael Foss-Feig, Phillip Richerme, Christopher Monroe, and Alexey V Gorshkov. Kaleidoscope of quantum phases in a long-range interacting spin-1 chain. *Physical Review B*, 93(20):205115, 2016.

[198] Lea F Santos and Marcos Rigol. Onset of quantum chaos in one-dimensional bosonic and fermionic systems and its relation to thermalization. *Physical Review E*, 81(3):036206, 2010.

[199] Fausto Borgonovi, Felix M Izrailev, Lea F Santos, and Vladimir G Zelevinsky. Quantum chaos and thermalization in isolated systems of interacting particles. *Physics Reports*, 626:1–58, 2016.

[200] Luca D'Alessio, Yariv Kafri, Anatoli Polkovnikov, and Marcos Rigol. From quantum chaos and eigenstate thermalization to statistical mechanics and thermodynamics. *Advances in Physics*, 65(3):239–362, 2016.

[201] Victoria Borish, Ognjen Marković, Jacob A Hines, Shankari V Rajagopal, and Monika Schleier-Smith. Transverse-field ising dynamics in a rydberg-dressed atomic gas. *Physical Review Letters*, 124(6):063601, 2020.